



저작자표시-비영리-변경금지 2.0 대한민국

이용자는 아래의 조건을 따르는 경우에 한하여 자유롭게

- 이 저작물을 복제, 배포, 전송, 전시, 공연 및 방송할 수 있습니다.

다음과 같은 조건을 따라야 합니다:



저작자표시. 귀하는 원저작자를 표시하여야 합니다.



비영리. 귀하는 이 저작물을 영리 목적으로 이용할 수 없습니다.



변경금지. 귀하는 이 저작물을 개작, 변형 또는 가공할 수 없습니다.

- 귀하는, 이 저작물의 재이용이나 배포의 경우, 이 저작물에 적용된 이용허락조건을 명확하게 나타내어야 합니다.
- 저작권자로부터 별도의 허가를 받으면 이러한 조건들은 적용되지 않습니다.

저작권법에 따른 이용자의 권리는 위의 내용에 의하여 영향을 받지 않습니다.

이것은 [이용허락규약\(Legal Code\)](#)을 이해하기 쉽게 요약한 것입니다.

[Disclaimer](#)

공학박사학위논문

리튬 이온 전지에서 음이온 산화물 양극재  
의 전자-기계적 기반 설계

Material design based on electro-mechanical  
modeling of poly-oxyanion cathode materials in  
lithium ion batteries

2019 년 8 월

서울대학교 대학원

기계항공공학부

이 상 관

# Abstract

The Li-ion battery is organized very sophisticated and complicated, hence have to develop the each part of the battery system to overcome the limitations of the Li-ion battery. Above all, challenges for the developing cathode part have been found the new cathode materials, and improve the cathode materials until now. Furthermore, the cathode materials operate on complex physical and chemical reactions from atomic scale to macro scale, thus have to study at each scale and bridging the scale, which is multiscale analysis.

In this dissertation, a systematic multiscale analysis based on mechanics is proposed from atomic scale using first-principles calculation to macro scale using phase field method at positive electrodes in Li-ion battery. Recent works, poly-oxyanion cathode materials received much attention for their higher capacity, higher energy density and stable materials structure. The poly-oxyanion materials are composed of lithium, transition metal, oxygen and anion (i.e.  $\text{LiFePO}_4$  and  $\text{Li}_2\text{FeSiO}_4$ ). Lithium orthosilicate  $\text{Li}_2\text{TMSiO}_4$  (TM = Fe, Mn, Ni and Co) are nowadays have attracted considerable attention for their higher theoretical capacity because of two Li ions insertion/extraction and stability for strong Si-O bonding force. And the orthosilicates suffer from their capacity fading or low electronic conductivity, so many studies are performed to overcome the disadvantages. However, almost approach is related to electrochemical or electronic point of view, not mechanical aspect. Mechanical behaviors of electrode materials are associated with rate capability, and dislocation and cracking micro particle cause of cyclic degradation. To explore the physical mechanism of

orthosilicates, mechanical properties are investigated using first-principles study. At first, elastic constants, several moduli and Poisson ratio of pristine orthosilicates are calculated and discuss the values related to elastic softness and rate capability that have a different types of transition metal. Furthermore, anisotropic factors which are new measurement are calculated to show the probability of dislocation and cracking. Also, fundamental understanding is discussed these mechanical values. Mechanical properties of binary multicomponent silicates  $\text{Li}_2\text{Fe}_{0.5}\text{TM}_{0.5}\text{SiO}_4$  (TM = Mn, Ni and Co) are also investigated and compared with pristine silicates, and the multicomponent silicate means that substituted from original transition metals to other transition metals.

Next study is performed the novel design of iron phosphor-silicate  $\text{LiFeP}_{1-x}\text{Si}_x\text{O}_4$  (LFPS,  $x = 0 \sim 1$ ) step by step to overcome the weakness of pristine iron phosphate like low voltage, anti-site defect phenomena and electronic conductivity, and find the optimized LFPS structure thermodynamically and the LFPS show that prevents the anti-site defect, increase electronic conductivity and control the voltage according to silicon ratio. Furthermore, we design the cathode materials substituted from several anions to phosphorus position at iron phosphate. At first, search for the anion candidates like Ge, As, Se, Sn and Sb including a same or closed group with Si and P, and find the thermodynamically favorable position for optimized structure based on ab-initio study. Finally, optimization structures are calculated the kinetical, electrochemical and electronic properties, and compared with pristine phosphate structure. For this research, Ge substitution structure  $\text{LiFeP}_{1-x}\text{Ge}_x\text{O}_4$  ( $x = 0 \sim 1$ ) most suitable material for used cathode part of Li-ion batteries than other anion substitution

structure materials.

Not only the atomic scale but also the macro scale analysis of novel designed cathode materials as mentioned before, phase field model is applied for the material's structure  $\text{LiFePO}_4$ ,  $\text{LiFeP}_{1-x}\text{Si}_x\text{O}_4$  ( $x = 0 \sim 1$ ). The mixing enthalpy about lithium ion concentration is calculated using the ab-initio study, and is consists of a governing equation connected to physics and chemistry. Through the multiphysics system that used bridging the scale, Phase separation, strain field, and stress field of cathode materials for macro scale.

Consequently, for the present multiscale analysis, the electrode mechanism of poly-oxyanion materials is studied for the mechanical aspect. Additionally, a novel designed the poly-oxyanion materials is suggested and researched from atomic scale to macro scale, so improve the performance of poly-oxyanion materials, and this approach will develop the cathode parts, and ultimately in the Li-ion battery.

**Keywords:** Li-ion battery, Cathode, Poly-oxyanion compound, Density functional theory, Phase field model, Multiscale Analysis.

**Student Number:** 2012-22562

# Table of Contents

<b>Table of Contents</b> .....	<b>iii</b>
<b>List of Figures</b> .....	<b>v</b>
<b>List of Tables</b> .....	<b>xii</b>
<b>1. Introduction</b> .....	<b>1</b>
1.1. Composition of Li ion batteries.....	2
1.2. Poly-oxyanion cathode materials .....	2
1.3. Multiscale analysis for Li-ion batteries .....	4
1.4. Objective and contributions of the thesis .....	5
<b>2. Mechanical properties of silicate cathode materials</b> .....	<b>11</b>
2.1. Importance for mechanical properties of electrode materials .....	11
2.2. Mechanical properties of pristine silicate materials $\text{Li}_2\text{TMSiO}_4$ (TM = Fe, Mn, Ni and Co).....	12
2.2.1. Elastic constants, several moduli and Poisson ratio .....	15
2.2.2. Shear and percentage anisotropic factors .....	19
2.3. Mechanical properties of binary multicomponent silicate materials $\text{Li}_2\text{Fe}_{0.5}\text{TM}_{0.5}\text{SiO}_4$ (TM = Mn, Ni and Co) .....	21
2.3.1. Elastic constants, several moduli and Poisson ratio .....	22

2.3.2. Shear and percentage anisotropic factors .....	23
2.4. Summary .....	25
<b>3. Novel design of poly-oxyanion cathode materials <math>\text{LiFeP}_{1-x}\text{Si}_x\text{O}_4</math> .....</b>	<b>59</b>
3.1. Overview of phosphate and silicate materials .....	59
3.2. Theoretical design of $\text{LiFeP}_{1-x}\text{Si}_x\text{O}_4$ .....	61
3.3. Improved the performance of $\text{LiFeP}_{1-x}\text{Si}_x\text{O}_4$ .....	64
3.4. Summary .....	70
<b>4. Several anion substitution design of <math>\text{LiFePO}_4</math> cathode material .....</b>	<b>90</b>
4.1. Introduction of poly-oxyanion materials and anion type.....	90
4.2. Theoretical design of $\text{LiFeP}_{1-x}\text{V}_x\text{O}_4$ ( $\text{V} = \text{Ge}, \text{As}$ and so on) .....	91
4.3. Improved the performance of $\text{LiFeP}_{1-x}\text{V}_x\text{O}_4$ ( $\text{V} = \text{Ge}, \text{As}$ and so on) .....	93
4.4. Summary .....	97
<b>5. Multiscale analysis for existing and new-designed poly-oxyanion cathode materials</b>	
.....	<b>119</b>
5.1. Phase field method bridging the atomic- and macro- scale.....	119
5.2. Phase separation of existing and new-designed poly-oxyanion materials.....	120
5.3. Strain field of existing and new-designed poly-oxyanion materials .....	121

5.4. Stress field of existing and new-designed poly-oxyanion materials .....	121
5.5. Summary .....	121
<b>6. Conclusions and recommendations.....</b>	<b>126</b>
<b>References .....</b>	<b>129</b>
<b>Abstract .....</b>	<b>142</b>

# List of Figures

**Figure 1.1** Comparison of Li-ion battery and other batteries systems with regard to gravimetric and volumetric energy density ..... 8

**Figure 1.2** Schematic of a Li-ion battery during charging/discharging process ..... 9

**Figure 1.3** Schematic of various poly-oxyanion cathode materials of Li-ion batteries .... 10

**Figure 2.1.1** The SEM images of  $\text{LiFePO}_4$ ..... 28

**Figure 2.2.1** Entire schematic of pristine silicates and their semi-lithiated and lithiated structures ..... 29

**Figure 2.2.2** Shear moduli  $G$  of pristine silicates (a)  $\text{Li}_x\text{FeSiO}_4$  (b)  $\text{Li}_x\text{MnSiO}_4$  (c)  $\text{Li}_x\text{NiSiO}_4$  and (d)  $\text{Li}_x\text{CoSiO}_4$  ( $x = 2$  and  $1$ )..... 31

**Figure 2.2.3** Bulk moduli  $B$  of pristine silicates (a)  $\text{Li}_x\text{FeSiO}_4$  (b)  $\text{Li}_x\text{MnSiO}_4$  (c)  $\text{Li}_x\text{NiSiO}_4$  and (d)  $\text{Li}_x\text{CoSiO}_4$  ( $x = 2$  and  $1$ )..... 34

**Figure 2.2.4** Young moduli  $E$  of pristine silicates (a)  $\text{Li}_x\text{FeSiO}_4$  (b)  $\text{Li}_x\text{MnSiO}_4$  (c)  $\text{Li}_x\text{NiSiO}_4$  and (d)  $\text{Li}_x\text{CoSiO}_4$  ( $x = 2$  and  $1$ ). ..... 37

**Figure 2.2.5** Poisson ratio  $\nu$  of pristine silicates (a)  $\text{Li}_x\text{FeSiO}_4$  (b)  $\text{Li}_x\text{MnSiO}_4$  (c)  $\text{Li}_x\text{NiSiO}_4$  and (d)  $\text{Li}_x\text{CoSiO}_4$  ( $x = 2$  and  $1$ ) ..... 38

**Figure 2.2.6** Shear anisotropic factors  $A_1$ ,  $A_2$  and  $A_3$  of pristine silicates (a)  $\text{Li}_x\text{FeSiO}_4$  (b)  $\text{Li}_x\text{MnSiO}_4$  (c)  $\text{Li}_x\text{NiSiO}_4$  and (d)  $\text{Li}_x\text{CoSiO}_4$  ( $x = 2$  and  $1$ ) ..... 39

**Figure 2.2.7** Percentage anisotropic factors  $A_G$  and  $A_B$  of pristine silicates (a)  $\text{Li}_x\text{FeSiO}_4$  (b)  $\text{Li}_x\text{MnSiO}_4$  (c)  $\text{Li}_x\text{NiSiO}_4$  and (d)  $\text{Li}_x\text{CoSiO}_4$  ( $x = 2$  and  $1$ )..... 41

<b>Figure 2.3.1</b> Schematics of multicomponent structure $\text{Li}_2\text{Fe}_{0.5}\text{Mn}_{0.5}\text{SiO}_4$ and semi-delithiated structure $\text{LiFe}_{0.5}\text{Mn}_{0.5}\text{SiO}_4$ .....	43
<b>Figure 2.3.2</b> Schematics of multicomponent structure $\text{Li}_2\text{Fe}_{0.5}\text{Ni}_{0.5}\text{SiO}_4$ and semi-delithiated structure $\text{LiFe}_{0.5}\text{Ni}_{0.5}\text{SiO}_4$ .....	44
<b>Figure 2.3.3</b> Schematics of multicomponent structure $\text{Li}_2\text{Fe}_{0.5}\text{Co}_{0.5}\text{SiO}_4$ and semi-delithiated structure $\text{LiFe}_{0.5}\text{Co}_{0.5}\text{SiO}_4$ .....	45
<b>Figure 2.3.4</b> Shear moduli $G$ of binray multicomponent silicates (a) $\text{Li}_x\text{Fe}_{0.5}\text{Mn}_{0.5}\text{SiO}_4$ (b) $\text{Li}_x\text{Fe}_{0.5}\text{Ni}_{0.5}\text{SiO}_4$ and (c) $\text{Li}_x\text{Fe}_{0.5}\text{Co}_{0.5}\text{SiO}_4$ ( $x = 2$ and $1$ ).....	46
<b>Figure 2.3.5</b> Bulk moduli $B$ of binray multicomponent silicates (a) $\text{Li}_x\text{Fe}_{0.5}\text{Mn}_{0.5}\text{SiO}_4$ (b) $\text{Li}_x\text{Fe}_{0.5}\text{Ni}_{0.5}\text{SiO}_4$ and (c) $\text{Li}_x\text{Fe}_{0.5}\text{Co}_{0.5}\text{SiO}_4$ ( $x = 2$ and $1$ ).....	48
<b>Figure 2.3.6</b> Young moduli $E$ of binray multicomponent silicates (a) $\text{Li}_x\text{Fe}_{0.5}\text{Mn}_{0.5}\text{SiO}_4$ (b) $\text{Li}_x\text{Fe}_{0.5}\text{Ni}_{0.5}\text{SiO}_4$ and (c) $\text{Li}_x\text{Fe}_{0.5}\text{Co}_{0.5}\text{SiO}_4$ ( $x = 2$ and $1$ ).....	50
<b>Figure 2.3.7</b> Poisson ratio $\nu$ of binray multicomponent silicates (a) $\text{Li}_x\text{Fe}_{0.5}\text{Mn}_{0.5}\text{SiO}_4$ (b) $\text{Li}_x\text{Fe}_{0.5}\text{Ni}_{0.5}\text{SiO}_4$ and (c) $\text{Li}_x\text{Fe}_{0.5}\text{Co}_{0.5}\text{SiO}_4$ ( $x = 2$ and $1$ ).....	51
<b>Figure 2.3.8</b> Shear anisotropic factors $A_1$ , $A_2$ and $A_3$ of multicomponent silicates (a) $\text{Li}_x\text{Fe}_{0.5}\text{Mn}_{0.5}\text{SiO}_4$ (b) $\text{Li}_x\text{Fe}_{0.5}\text{Ni}_{0.5}\text{SiO}_4$ and (c) $\text{Li}_x\text{Fe}_{0.5}\text{Co}_{0.5}\text{SiO}_4$ ( $x = 2$ and $1$ ) .....	52
<b>Figure 2.3.9</b> Percentage anisotropic factors $A_G$ and $A_B$ of multicomponent silicates (a) $\text{Li}_x\text{Fe}_{0.5}\text{Mn}_{0.5}\text{SiO}_4$ (b) $\text{Li}_x\text{Fe}_{0.5}\text{Ni}_{0.5}\text{SiO}_4$ and (c) $\text{Li}_x\text{Fe}_{0.5}\text{Co}_{0.5}\text{SiO}_4$ ( $x = 2$ and $1$ ) .....	54
<b>Figure 3.1</b> (a) Formation energies of the most optimized olivine and tetrahedral structures for mixed phosphorus and silicon. Chemical equation is $\text{LiFeP}_{1-x}\text{Si}_x\text{O}_4$ . (b) Formation energies of all possible structure at only olivine crystal structure. Pink points mean that	

most optimized structures thermodynamically.....	72
<b>Figure 3.2</b> Ground state structures of olivine $\text{LiFeP}_{1-x}\text{Si}_x\text{O}_4$ (a) $x=0$ (b) $x=0.125$ (c) $x=0.250$ (d) $x=0.375$ (e) $x=0.5$ (f) $x=0.625$ (g) $x=0.75$ (h) $x=0.875$ (i) $x=1$ . Green color represents Li atoms; blue, Si; gray, P; brown Fe.....	74
<b>Figure 3.3</b> Lattice parameters a, b, c and volume V of $\text{LiFeP}_{1-x}\text{Si}_x\text{O}_4$ according to Si proportion.....	75
<b>Figure 3.4</b> Bonding distance of most optimized olivine structure. Bonding distance between (a) P and O. (b) Si and O (c) Li and O and (d) Fe and O .....	78
<b>Figure 3.5</b> Li migration path schematics along the (010) of $\text{LiFePO}_4$ , $\text{LiFeP}_{0.5}\text{Si}_{0.5}\text{O}_4$ and $\text{LiFeSiO}_4$ .....	81
<b>Figure 3.6</b> Calculated lithium migration energy barriers along the (010) path of $\text{LiFePO}_4$ , $\text{LiFeP}_{0.5}\text{Si}_{0.5}\text{O}_4$ and $\text{LiFeSiO}_4$ .....	82
<b>Figure 3.7</b> Bader charge of Fe & O of iron phosphor-silicate for olivine structure $\text{LiFeP}_x\text{Si}_{1-x}\text{O}_4$ with increase in P ratio.....	83
<b>Figure 3.8</b> (a) Voltage of iron phosphor-silicate for olivine structure $\text{LiFeP}_{1-x}\text{Si}_x\text{O}_4$ according to Si ratio ( $x=0\sim 1$ ) (b) Voltage profiles of olivine structure $\text{LiFePO}_4$ , $\text{LiFeP}_{0.5}\text{Si}_{0.5}\text{O}_4$ and $\text{LiFeSiO}_4$ as Li concentration.....	84
<b>Figure 3.9</b> Relative volumetric energy densities of iron phosphor-silicate for olivine structure $\text{LiFeP}_{1-x}\text{Si}_x\text{O}_4$ compared with pristine iron phosphate $\text{LiFePO}_4$ .....	86
<b>Figure 3.10</b> Total density of states (TDOS) of iron phosphate and iron phosphor-silicate for olivine structure $\text{LiFeP}_{1-x}\text{Si}_x\text{O}_4$ ( $x= 0$ and $0.5$ ) (a) $\text{LiFePO}_4$ (b) $\text{FePO}_4$ (c)	

LiFeP<sub>0.5</sub>Si<sub>0.5</sub>O<sub>4</sub> and (d) FeP<sub>0.5</sub>Si<sub>0.5</sub>O<sub>4</sub> ..... 87

**Figure 4.1** Olivine structure *Pnma* space group and periodic table for show original anion elements Si, P and the anion candidates substituted for original anion position As, Sb, Ge, Sn and Se ..... 99

**Figure 4.2** Thermodynamic total energy and atomic radius the anion candidates substituted for original anion position As, Sb, Ge, Sn and Se ..... 100

**Figure 4.3** Entire schematics of LiFeP<sub>1-x</sub>V<sub>x</sub>O<sub>4</sub> according to V proportion ( $x = 0 \sim 1$  and V = As, Sb, Ge, Sn and Se) ..... 101

**Figure 4.4** Lattice parameters a, b, c and volume V of substituted As anion for olivine structure LiFeP<sub>1-x</sub>As<sub>x</sub>O<sub>4</sub> according to As proportion ( $x = 0 \sim 1$ ) ..... 104

**Figure 4.5** Lattice parameters a, b, c and volume V of substituted Sb anion for olivine structure LiFeP<sub>1-x</sub>Sb<sub>x</sub>O<sub>4</sub> according to Sb proportion ( $x = 0 \sim 1$ ) ..... 106

**Figure 4.6** Lattice parameters a, b, c and volume V of substituted Ge anion for olivine structure LiFeP<sub>1-x</sub>Ge<sub>x</sub>O<sub>4</sub> according to Ge proportion ( $x = 0 \sim 1$ ) ..... 108

**Figure 4.7** Lattice parameters a, b, c and volume V of substituted Sn anion for olivine structure LiFeP<sub>1-x</sub>Sn<sub>x</sub>O<sub>4</sub> according to Sn proportion ( $x = 0 \sim 1$ ) ..... 110

**Figure 4.8** Lattice parameters a, b, c and volume V of substituted Se anion for olivine structure LiFeP<sub>1-x</sub>Se<sub>x</sub>O<sub>4</sub> according to Se proportion ( $x = 0 \sim 1$ ) ..... 112

**Figure 4.9** Voltage profile of original LiFePO<sub>4</sub> and substituted As anion for olivine structure LiFeP<sub>1-x</sub>As<sub>x</sub>O<sub>4</sub> ( $x = 0 \sim 1$ ) ..... 114

**Figure 4.10** Voltage profile of original LiFePO<sub>4</sub> and substituted Sb anion for olivine

structure $\text{LiFeP}_{1-x}\text{Sb}_x\text{O}_4$ ( $x = 0 \sim 1$ ).....	115
<b>Figure 4.11</b> Voltage profile of original $\text{LiFePO}_4$ and substituted Ge anion for olivine structure $\text{LiFeP}_{1-x}\text{Ge}_x\text{O}_4$ ( $x = 0 \sim 1$ ) .....	116
<b>Figure 4.12</b> Voltage profile of original $\text{LiFePO}_4$ and substituted Sn anion for olivine structure $\text{LiFeP}_{1-x}\text{Sn}_x\text{O}_4$ ( $x = 0 \sim 1$ ).....	117
<b>Figure 4.13</b> Voltage profile of original $\text{LiFePO}_4$ and substituted Se anion for olivine structure $\text{LiFeP}_{1-x}\text{Se}_x\text{O}_4$ ( $x = 0 \sim 1$ ).....	118
<b>Figure 5.1</b> Entire numerical algorithm of multiscale analysis, DFT simulation and PFM method.....	127
<b>Figure 5.2</b> Mixing enthalpy at optimized $\text{LiFePO}_4$ (LFP) structures as a function of the inverse Li contents ( $x = 0 \sim 1$ ).....	127
<b>Figure 5.3</b> Mixing enthalpy at optimized $\text{LiFeP}_{0.5}\text{Si}_{0.5}\text{O}_4$ (LFPS) structures as a function of the inverse Li contents ( $x = 0 \sim 1$ ).....	128
<b>Figure 5.4</b> Homogeneous free energies $f_{\text{CP}}$ of LFP and LFPS structures as a function of the inverse Li contents $x$ .....	128
<b>Figure 5.5</b> Entire schematics of phase separation of (a) LFP and (b) LFPS structures at various dimensionless time $t$ .....	129
<b>Figure 5.6</b> Entire schematics of strain field $\epsilon_{xx}$ of (a) LFP and (b) LFPS structures at various dimensionless time $t$ .....	129
<b>Figure 5.7</b> Entire schematics of strain field $\epsilon_{yy}$ of (a) LFP and (b) LFPS structures at various dimensionless time $t$ .....	130

**Figure 5.8** Entire schematics of strain field  $\epsilon_{xy}$  of (a) LFP and (b) LFPS structures at various dimensionless time  $t$  ..... 130

**Figure 5.9** Entire schematics of stress field  $\sigma_{xx}$  of (a) LFP and (b) LFPS structures at various dimensionless time  $t$  ..... 131

**Figure 5.10** Entire schematics of stress field  $\sigma_{yy}$  of (a) LFP and (b) LFPS structures at various dimensionless time  $t$  ..... 131

**Figure 5.11** Entire schematics of stress field  $\sigma_{xy}$  of (a) LFP and (b) LFPS structures at various dimensionless time  $t$  ..... 132

## List of Tables

<b>Table 2.2.1</b> Elastic constants (given in GPa) of $\text{Li}_2\text{TMSiO}_4$ and $\text{LiTMSiO}_4$ (TM = Fe and Mn).....	56
<b>Table 2.2.2</b> Elastic constants (given in GPa) of $\text{Li}_2\text{TMSiO}_4$ and $\text{LiTMSiO}_4$ (TM = Ni and Co).....	57
<b>Table 2.3.2</b> Elastic constants (given in GPa) of $\text{Li}_2\text{Fe}_{0.5}\text{TM}_{0.5}\text{SiO}_4$ and $\text{LiFe}_{0.5}\text{TM}_{0.5}\text{SiO}_4$ (TM = Mn, Ni and Co).....	58

# 1. Introduction

Li-ion batteries (LIBs) are promising electronic energy storage for a long time because they can be used continuously due to lithium ion moving, and they have higher volumetric and gravimetric energy density as shown in Fig.1.1.<sup>1</sup> So, they have been widely used various electronic devices like portable electronics, cellular phone, smartphone, and other small computing and electronic equipment. Moreover, development of the Li-ion batteries is expected that they can use the large electronic device like plug-in hybrid vehicles (PHEV), electric vehicles (xEV) and energy storage system. (EES).<sup>2</sup> However, for use the Li ion batteries commercial large electronic device, they need to more development in several aspects. Among these, finding and upgrade the performance of cathode materials are essential to the application of LIBs at large electronic devices.<sup>3-4</sup> Poly-oxyanion materials are founded relatively recent, and the materials include anions not oxygen with lithium and transition metals, and the materials show the develop performance but many limitations. Thus this thesis shows the various properties of poly-oxyanion materials that have not studied until now. Furthermore, we designed novel poly-oxyanion cathode materials and show several performances and compare with existing poly-oxyanion materials using multiscale analysis.

In this chapter, the working mechanism and composition of Li-ion batteries and thermodynamics of the system are introduced, besides, poly-oxyanion compounds and multiscale analysis of the studies are shown in the chapter. Finally, the chapter concludes

with the objective and contribution of the present thesis.

## **1.1. Composition of Li-ion batteries**

Li-ion batteries are constituted of three parts, anode, cathode, and electrolyte. Among these, anode and cathode are called negative electrode and positive electrode following oxidation and reduction process, the anode is negative electrode and cathode is positive electrode at Li-ion batteries system.<sup>5-7</sup> The schematic of Li-ion batteries is shown in Fig.1.2.<sup>8</sup> At first, Li ions ( $\text{Li}^+$ ) moved from anode to cathode for the discharging process, and when the charging process, Li ions moved from cathode to anode. An electrolyte is located between anode and cathode and has the role that electrons can move between anode and cathode, so charge carrier lithium is reacted  $\text{Li}^0/\text{Li}^+$  redox. The voltage means that electrochemical potential when Li ion insertion/extraction (lithiation and delithiation) and capacity is means that amounts of the Li ions that can be moved between anode and cathode, respectively.<sup>9</sup> Based on the process, Li-ion batteries convert chemical and electrical energies continuously for the charging/discharging process.<sup>10</sup>

## **1.2. Poly-oxyanion cathode materials**

Present Li-ion batteries cannot be used for commercial large electronic devices because they didn't show the appropriate performance for the devices. Hence, to develop

the Li-ion batteries, many studies are performed until now. Mainly, the point of the studies finding the new electrode (anode and cathode) materials that have better properties or improved the performance of the existing electrode materials. And present cathode materials cannot show the performance that is catch up with the anode. Recent works suggested poly-oxyanion cathode materials that have anions not oxygen atoms with lithium and transition metals. Entire schematics of poly-oxyanion materials are shown in Fig.1.3. Iron phosphate  $\text{LiFePO}_4$  has attracted many interests after was first found by Goodenough and coworkers in 1997.<sup>11-12</sup> The structure contains *hcp* anion oxygen arrays with half octahedral sites occupied by iron and lithium. So Li and Fe have  $\text{LiO}_6$  and  $\text{FeO}_6$  octahedral shapes, and parallel to c-axis. And P has  $\text{PO}_4$  tetrahedral shape edge sharing with  $\text{FeO}_6$  octahedral sites. Through many previous studies are shown that lithium diffusion path is only (010) direction along the b axis, after Yamada and his coworkers certified precise lithium ion path curved one dimension for (010) direction from experiments. The materials show the good cyclability and stable structure, but hindered for anti-site defect, low energy density, low electronic conductivity and low voltage compared previous cathode materials like  $\text{LiCoO}_2$ .<sup>13</sup> Hence, various studies have attempted for overcoming the limitations, like nano-particle synthesis, carbon coating, and exchange or insertion of other transition metals, and so on. After various phosphates are suggested by many scientist like  $\text{LiMnPO}_4$ ,  $\text{LiNiPO}_4$  and  $\text{LiCoPO}_4$  and studied their many properties related with cathode materials of Li-ion batteries.<sup>14-16</sup> Carbon coating techniques help that overcome the low electronic conductivity, but other disadvantages did not overcome perfectly. Silicate material is found

more recently than phosphate. The first attempt is only substitution P to other anions, so selected Si, but the experiment is shown different chemical equation. Anton Nyten et al first found  $\text{Li}_2\text{FeSiO}_4$  in 2005.<sup>17</sup> The first structure has a tetrahedral structure  $Pmn2_1$  space group that is extracted two Li ions per unit formula, so has the higher theoretical capacity (ca. 330mAh<sup>-1</sup>).<sup>18</sup> But the practical capacity is lower than the theoretical value. So various attempts are performed overcome the limitation like phosphate.<sup>19-21</sup> As a result, there is revealed silicates have polymorphism that means can have various crystal structure even though same chemical equation.<sup>22-23</sup> Following the synthesis temperature, various structures ( $Pmn2_1$ ,  $P2_1/n$ ,  $Pmnb$  and so on) can be synthesized, also can have various transition metals like Mn, Ni and Co.<sup>24-25</sup> At Fig.1.3, brown color is named only Fe, but the location of the other transition metals is possible with the same position.<sup>26-27</sup> The silicate structure suffers from low ionic conductivity, low electronic conductivity, different voltage plateau for the first and second Li ion redox process for phase transformation and so on. So many studies have to perform to find the breakthrough like phosphate.

### **1.3. Multiscale analysis for Li-ion batteries**

For more deeply researches, multiscale analysis based on the atomic scale and macro scale are essential for the complex system like Li-ion batteries.<sup>28</sup> Many properties like mechanical, chemical, physical, electrical and electrochemical reactions have occurred at a various range of the size scale for dynamic systems at many applications. At first, the

atomistic simulation used first-principles study has been used for the various systems of atomic size, and the simulation can show the lattice parameters and volume of crystal structure, many physical and chemical properties based on density functional theory. To solve macro scale problems like particle and electrode, the mesoscale problems, furthermore thermodynamics, micromechanics, electrochemical parts, continuum mechanics, and so on have been investigated for used phase field model. At the complex systems, the computational study for narrow size has limitations for research of the entire system.<sup>29</sup> For the understanding of the complex system, not a single scale analysis, but bridging the several scales is very important for a detail study.<sup>30</sup> For example, single crystal structures of  $\text{LiFePO}_4$  or  $2\text{D-Li}_2\text{FeSiO}_4$  cathode materials have orthorhombic characteristics but have the isotropic characteristics for the electrode systems because the single crystals are aggregated to polycrystalline kinetically. Also, negative and positive electrodes are combined with electrolytes, show the different characteristics compares with only electrodes. In conclusion, the study of complex systems like Li-ion batteries, multiscale analysis has to be performed.<sup>31</sup>

#### **1.4. Objective and contribution of the thesis**

The aim of this dissertation is to understand the mechanical aspect at the electrode of Li ion batteries and newly design the novel electrode materials within the multiscale analysis. In chapter 2, the mechanical properties of silicate materials that including poly-

oxyanion compounds for anticipating the probability of dislocation and crack of particle cause of cyclic degradation, and bridging of macro scale for multiscale analysis are calculated using first-principles study. The elastic constants of pristine and binary multicomponent silicate materials, several moduli and Poisson ratio for secondary particle are calculate based on first-principles study. And, shear and percentage anisotropic factors that are the measurement of dislocation and cracking are calculated. From the simulation, manganese silicate is hampered mechanical properties, and multicomponent silicate is a breakthrough for overcoming the dislocation or crack of electrode mechanical aspect.<sup>32</sup>

Furthermore, the novel poly-oxyanion cathode materials  $\text{LiFeP}_{1-x}\text{Si}_x\text{O}_4$  ( $x = 0 \sim 1$ ) are designed to overcome the limitations for used cathode materials based on the previous studies in chapter 3. The newly designed poly-oxyanion cathode materials can overcome the limitations of pristine iron phosphate. At first, prevent the anti-site defect through stronger Fe-O bonding, next control the voltage until 4.97V according to Si ratio. Finally, the new materials better electronic conductivity and energy density than the conductivity of pristine iron phosphate.

In chapter 4, we designed poly-oxyanion compounds newly, for substituted several anions for pristine iron phosphate,  $\text{LiFeP}_{1-x}\text{V}_x\text{O}_4$  ( $x = 0 \sim 1$  and  $\text{V} = \text{As}, \text{Ge}$  and so on) for developing the performance of the Li-ion batteries. As a result, anion Ge is the most optimized element for substitution for phosphorus position of pristine iron phosphate because of stable structure and higher voltage and can control the voltage. On the other hands, Se substitution make the structure is very unstable because of its charge

distribution.<sup>9</sup>

In chapter 5, the multiscale analysis that bridged from atomic scale to macro scale is investigated with pristine poly-oxyanion material and newly designed poly-oxyanion materials, so show the phase separation according to Li ion concentration. The phase separation is decreased to newly designed poly-oxyanion materials  $\text{LiFeP}_{1-x}\text{Si}_x\text{O}_4$  as Si ratio increased, so phase stabilize more and more, hence cyclic performance and rate capability is better than pristine  $\text{LiFePO}_4$ . Besides, the strain field and stress field are investigated, and from the multiscale simulation results, we know that structural distortion and the magnitude of the stress are decreased according to Si ratio.<sup>33</sup>

Consequently, multiscale analysis for mechanics is investigated pristine and newly designed poly-oxyanion materials. So the newly designed materials can overcome the disadvantages of the present materials for used cathode material of Li-ion batteries. So these theoretical design of cathode materials will be light the way for the more improved Li-ion batteries, furthermore many electrochemical systems.

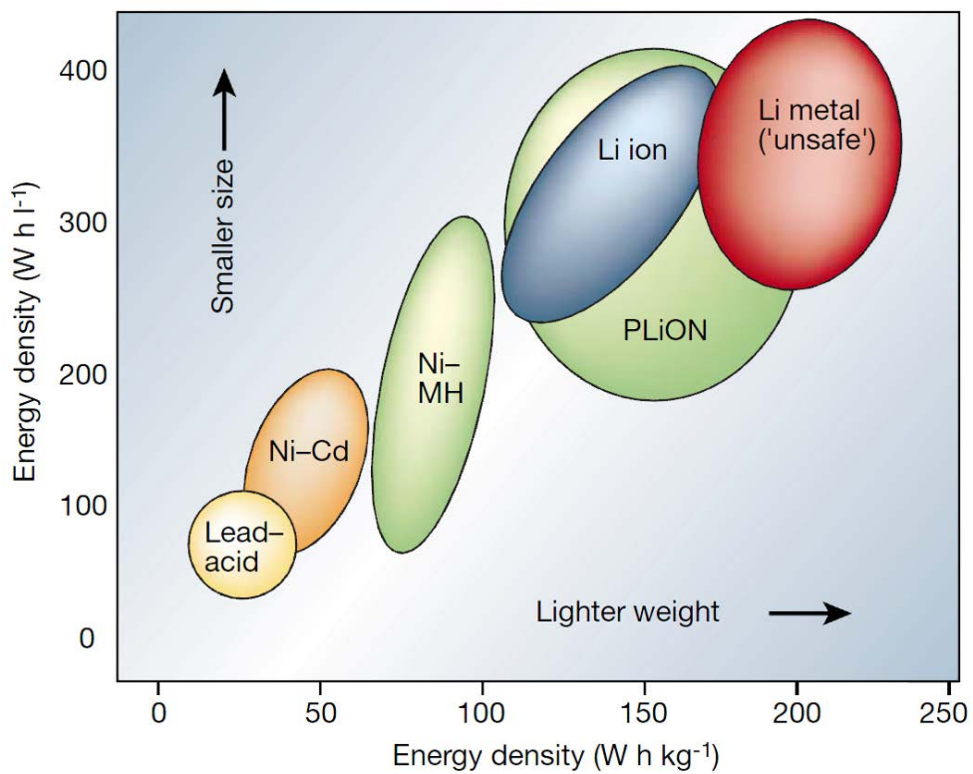


**Figure 1.1. Schematic of Li-ion battery system and various battery system in terms of gravimetric and volumetric energy density.<sup>1</sup>**

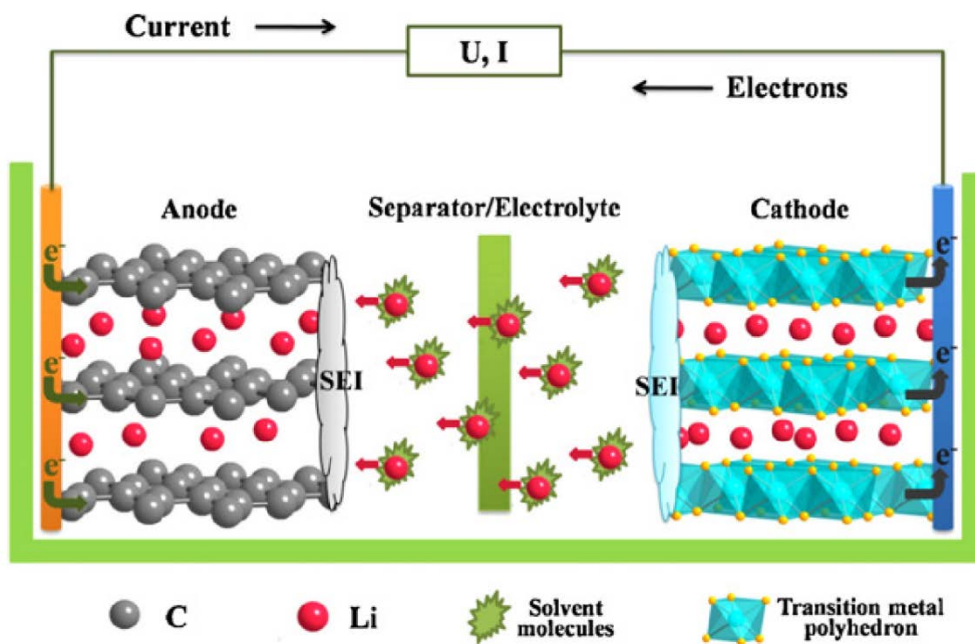
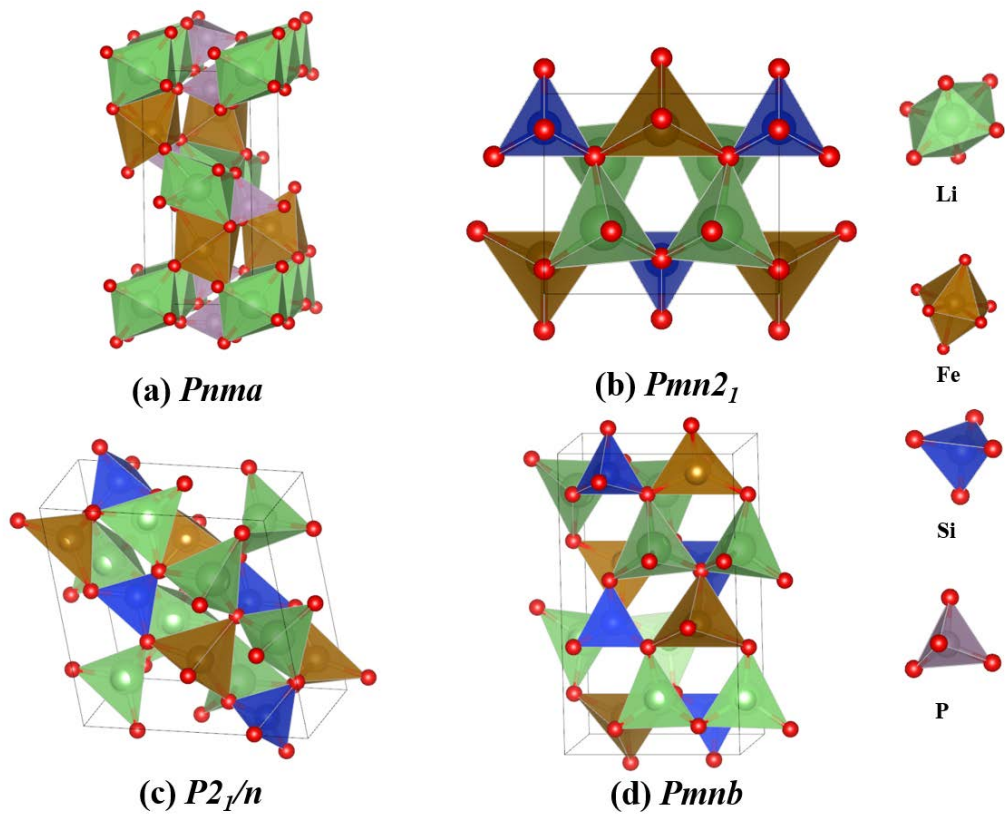


Figure 1.2. Entire schematic of Li-ion battery during charging process. The battery is constituted anode, cathode and electrolyte.<sup>8</sup>



**Figure 1.3. Entire schematic of various poly-oxyanion cathode materials for Li ion battery. (a)  $\text{LiFePO}_4$  olivine structure that phosphate can have. Space group is  $Pnma$ . (b)  $Pmn2_1$  (c)  $P2_1/n$  and (d)  $Pmn$  are silicate  $\text{Li}_2\text{FeSiO}_4$  structures following polymorphism. And all structures can have other transition metal.**

## 2. Mechanical properties of silicate cathode materials

### 2.1. Importance for mechanical properties of electrode materials

Several factors have interrupted that orthosilicates used to commercial Li-ion batteries, hence many studies performed by scientists such as nanostructure synthesis, carbon coatings, site exchange, and addition or substitution of other anions and cations to overcome the limitations of silicates.<sup>20, 34</sup> Among them, a strategy to stabilize the silicate crystal structure is the substitution with larger transition metal cations, such as Mn at Fe silicate. Many attempts that substituted at various type of transition metals have been performed, and these silicates including two or more transition metals named multicomponent silicate.<sup>4, 19, 35-39</sup> Through many previous studies, electrochemical properties (i.e. capacity, voltage, ionic mobility and so on) and electric properties (i.e. charge distribution, electronic conductivity, and so on) are attached so intensive.<sup>28, 34, 40-41</sup> On the other hand, only kinetic properties like lattice parameter and volume, and bonding length are studied at the mechanical aspect. In this paper, first-principles study based on density functional theory is performed about the mechanical properties of silicates.<sup>42</sup> At elastic constants of pristine silicates than mean have the only one transition metal  $\text{Li}_2\text{TMSiO}_4$  (TM = Fe, Mn, Ni and Co) was calculated, and shear, bulk and young moduli and Poisson ratio were calculated, and compared with the properties, and show stability and elastic softness of the structures during the charging/discharging process.<sup>43-44</sup>

Furthermore, shear anisotropic factors based on the elastic constants and shear and bulk percentage anisotropic factors based on shear and bulk moduli are investigated for the dislocation and crack probability for insertion and extraction Li ions.<sup>45-47</sup> At last, the same properties of binary multicomponent silicates based on iron  $\text{Li}_2\text{Fe}_{0.5}\text{TM}_{0.5}\text{SiO}_4$  (TM = Mn, Ni and Co) are calculated, and compared multicomponent system with pristine system. The research results will help a detail study for mechanical mechanism and the substitution effect of other transition metals of silicate structures, moreover, the plan making for improving the silicates to use cathode materials.

## **2.2. Mechanical properties of pristine silicate materials $\text{Li}_2\text{TMSiO}_4$ (TM = Fe, Mn, Ni and Co)**

The ab-initio calculations were performed used by density functional theory (DFT) method with plane wave basis sets and projector augmented wave (PAW) pseudopotentials as implemented in VASP code. Besides we used a generalized gradient approximation (GGA) with the Perdew-Burke-Ernzerhof (PBE) functional of the exchange and correlation interactions.<sup>48</sup> The electronic wave functions are represented by plane waves with a kinetic energy cut-off of 500 eV. In all calculations, there are used the k-point mesh in the Monkhorst pack scheme set up to 6x6x6 grid per reciprocal lattice vector, to ensure a convergence of 1 meV per formula unit of the energy for optimized electronics at self-consistent calculation. To optimize crystal structures, atomic coordinates and cell

parameters are fully relaxed.

The calculation method of elastic constants using first principles study is well established based on internal energy difference according to the strain tensor for orthorhombic crystal structures.<sup>49-50</sup> Bulk and shear moduli are calculated to use the elastic constants  $c_{ij}$  and elastic compliance constants  $s_{ij}$  based on Voigt and Reuss approximation, respectively.<sup>51-</sup>

<sup>52</sup> At first, Voigt shear modulus ( $G_V$ ) and Reuss shear modulus ( $G_R$ ) are defined following next equations:

$$G_V = \frac{(c_{11} + c_{22} + c_{33} - c_{12} - c_{13} - c_{23}) + 3(c_{44} + c_{55} + c_{66})}{15} \quad (2.2.1)$$

$$G_R = \frac{15}{4(s_{11} + s_{22} + s_{33}) - 4(s_{12} + s_{13} + s_{23}) + 3(s_{44} + s_{55} + s_{66})} \quad (2.2.2)$$

Next, the equations of Voigt bulk modulus ( $B_V$ ) and Reuss bulk modulus ( $B_R$ ) are next:

$$B_V = \frac{(c_{11} + c_{22} + c_{33}) + 2(c_{12} + c_{13} + c_{23})}{9} \quad (2.2.3)$$

$$B_R = \frac{1}{(s_{11} + s_{22} + s_{33}) + 2(s_{12} + s_{13} + s_{23})} \quad (2.2.4)$$

In the next generation, Hill proved that Voigt and Reuss values mean maximum and minimum values of isotropic crystal, so suggested average value for practical estimation and equations are next<sup>53-54</sup>:

$$G_H = \frac{G_V + G_R}{2} \quad \text{and} \quad B_H = \frac{B_V + B_R}{2} \quad (2.2.5)$$

Moreover, Young modulus ( $E_H$ ) and Poisson ratio ( $\nu_H$ ) are calculated using Hill's theory,

and the equations is next:

$$E_H = \frac{9B_H G_H}{3B_H + G_H} \text{ and } \nu_H = \frac{3B_H - 2G_H}{2(3B_H + G_H)} \quad (2.2.6)$$

For confirm the anisotropy, anisotropic factor is cacluated in various ways, and shear anisotropic factors which are calculated from elastic constants for single crystal are given below:

$$A_1 = \frac{4c_{44}}{c_{11} + c_{33} - 2c_{13}} \quad (2.2.7)$$

for (100) shear planes between  $\langle 011 \rangle$  and  $\langle 010 \rangle$  directions,

$$A_2 = \frac{4c_{55}}{c_{22} + c_{33} - 2c_{23}} \quad (2.2.8)$$

for (010) shear planes between  $\langle 101 \rangle$  and  $\langle 001 \rangle$  directions, and

$$A_3 = \frac{4c_{66}}{c_{11} + c_{22} - 2c_{12}} \quad (2.2.9)$$

for (001) shear planes between  $\langle 110 \rangle$  and  $\langle 010 \rangle$  directions. If single crystal is isotropic, the values have to be one, and any value bigger or smaller than unity is a measurement of elastic anisotropy.

For a polycrystlline material, percentage anisotropic factors are introduced by Chung and Buessem, and the values are closer with electrode materials from the experiment. The shear percentage anisotropic factor ( $A_G$ ) and bulk percentage anisotropic factor ( $A_B$ ) are given below:

$$A_G = \frac{G_V - G_R}{G_V + G_R} \quad (2.2.10)$$

$$A_B = \frac{B_V - B_R}{B_V + B_R} \quad (2.2.11)$$

### 2.2.1. Elastic constants, several moduli and Poisson ratio

In this study, the calculation of elastic constants of silicate crystal structures  $\text{Li}_2\text{TMSiO}_4$  (TM = Fe, Mn, Ni and Co) are calculated based on density functional theory is performed at first.<sup>25</sup> Before calculations to obtain the elastic constants, an initial calculation has to be carried out to optimized silicate crystal structure with  $Pmn2_1$  space group.<sup>55-56</sup> The calculation that finds the optimized all silicate crystal structures that has four different transition metals is performed. Furthermore, the parameters are calculated not only parameters of pristine silicate structures, but also their semi-delithiated  $\text{LiTMSiO}_4$  and fully-delithiated structure  $\text{TMSiO}_4$ , and their entire schemes are shown in Fig.2.2.1, respectively. In this calculation, generalized gradient approximation (GGA) method is used at all crystal structure not GGA+U method.<sup>25</sup> Generally, GGA+U method is more accurate than LDA or GGA method when calculating structure that has atoms including d-orbital, so widely used at almost ab-initio study. Electronic or electrochemical properties are more accurate when used GGA+U method, but the structural parameter is more accurate when used GGA method. For calculate mechanical properties, the structural parameter is dominant compared with other properties, so adopted the GGA method in this calculation.

Lattice parameters and volume are different according to the type of transition metal at silicate material, however, the difference is very small because silicates have the same orthorhombic structure space group and strong Si-O bonding force affects much bigger than the type of transition metals. Additionally, the result well agrees with other DFT studies. Next, the calculation of elastic constants is performed as mentioned before, and the P.Ravindra and co-workers well organized the calculation method that used the relation between internal energy and lattice distortion. Using this method, total nine independent elastic constants are calculated for each pristine silicate structure distinguished by a transition metal,  $\text{Li}_2\text{TMSiO}_4$  (TM = Fe, Mn, Ni and Co) and their semi-delithiated structure  $\text{LiTMSiO}_4$ , and the result is shown in Table.2.2.1 and Table.2.2.2. In this result, you can be conscious that there are no calculated elastic constants fully-delithiated structure  $\text{TMSiO}_4$ . The reason is when used the method mentioned the previous section at fully-delithiated structure, internal energy-distortion plots cannot normal polynomial fitting. And these results well correspond with experimental results and the reason is as follows. Until recent works from a first study, silicates cannot extract two lithium ions per  $\text{Li}_2\text{TMSiO}_4$  formula unit, so cannot show the theoretical capacity because occur the phase transformation upon cycling.<sup>57</sup> Therefore, no structure maintains a space group  $Pmn2_1$  crystal structure. Even if the structure exists for experiment development, it is very unstable breaking to small external stress. Hence, normal polynomial fitting is impossible because fully-delithiated structure modeling is possible for computational simulation, but very unstable when it occurs distortion for tensile or compression stress. For all pristine silicate structures, elastic

constants are very similar, and this result means that transition metals do not affect mechanical properties because of strong Si-O bonding force. And when extract Li ions, almost elastic constants are decreased, but only  $c_{11}$  of  $\text{Li}_x\text{MnSiO}_4$  and  $\text{Li}_x\text{CoSiO}_4$  ( $x=2$  and  $1$ ) is increased. And the decreased gaps of elastic constants are very small, also the increased gap of  $c_{11}$  is small in the case of  $\text{Li}_x\text{CoSiO}_4$ , too. On the other hand, the increased/decreased gap is larger than only for  $\text{Li}_x\text{MnSiO}_4$  crystal structure compared with other silicate structures at  $c_{11}$ ,  $c_{22}$ ,  $c_{33}$  and  $c_{44}$ , respectively. The charge state difference of transition metal  $\text{TM}^{2+}/\text{TM}^{3+}$  occurs during the extraction of one mol Li ion at electrode material. If transition metal is Mn, the structure suffers from the Jahn-teller distortion of  $\text{Mn}^{3+}$  which causes low cyclic performance.<sup>58</sup> And the Jahn-teller distortion indicates anisotropic electron configuration, it affects that the crystal structure becoming unstable during the charging/discharging process. Therefore, only  $\text{Li}_x\text{MnSiO}_4$  shows a different elastic constants change with other orthosilicates, and several moduli and anisotropic factors which will be discussed afterward in detail.

When electrode compound is synthesized through the experiment, it is impossible that successful synthesis of single crystal structure. Because each crystal aggregates having random orientations for synthesis process, so no specific direction exists for finished polycrystalline structure. In other words, synthesis electrode compound is an isotropic system, hence a measurement of polycrystalline shear modulus (G) and bulk modulus (B) may be determined on the compound. At first, Voigt approximation equated either the uniform strain to the external strain, and Reuss approximation equated the uniform stress

to the external stress at the polycrystalline, respectively. Afterward, Hill showed that the Voigt and Reuss values mean maximum and minimum of the true value of polycrystalline, so average the Voigt and Reuss values, and the value is standard value among three. The theory is named VRH approximation and based on the theory, shear, bulk and young moduli and Poisson ratio are calculated through the equations (2.1.1) – (2.1.6). Using this theory, at first, we performed shear modulus (G) of silicates and their semi-delithiated structures  $\text{Li}_2\text{TMSiO}_4$  and  $\text{LiTMSiO}_4$  as shown in Fig.2.2.2. At  $\text{Li}_2\text{TMSiO}_4$ , shear modulus G has very similar irrespective of transition metals (ca. 40GPa in Hill value). Next, one of semi-delithiated structure  $\text{LiTMSiO}_4$  is decreased at all silicate structure.  $\text{LiMnSiO}_4$  has the smallest shear modulus, next to the moduli of  $\text{LiNiSiO}_4$  and  $\text{LiCoSiO}_4$ , finally,  $\text{LiFeSiO}_4$  has the biggest one. In the case of bulk modulus, almost tendency is same with shear modulus, but the one of  $\text{LiCoSiO}_4$  is bigger than one of  $\text{LiNiSiO}_4$  as shown in Fig.2.2.3. At last, Fig.2.2.4 shows Young modulus E of pristine silicate, and the tendency is the same with shear modulus. The research results about elastic constants and several moduli show that elastic softness of pristine silicate according to transition metals. At  $\text{TM}^{2+}/\text{TM}^{3+}$  redox reactions, elastic softness is very similar, but Mn silicate enhanced elastic softness at  $\text{TM}^{3+}/\text{TM}^{4+}$  redox reactions, so can extract more Li ions and has better Li ionic mobility. However, the variation of the mechanical properties of Mn silicate is bigger than other transition metal silicate, so applied stress is bigger when the charging/discharging process, and it corresponds with anisotropic factors which will be discussed later. Consequently, Fe silicate is better variation mechanical properties compared with other silicates, especially

Mn silicate, and this result relates to longer cyclability. On the other hand, Mn silicate has enhanced elastic softness at semi-delithiated structure that means higher capacity and rate capability than other silicates, especially Fe silicate. And the results have good agreement with experimental reference. In Fig.2.2.5, Poisson ratio ( $\nu$ ) of pristine silicates and their semi-delithiated structure is shown, and the values are similar 0.28 ~ 0.30. In generally, Poisson ratio value has similar with the same materials, hence silicates and their semi-delithiated structures are the same materials like steel irrespective of transition metals.

### **2.2.2. Shear and percentage anisotropic factors**

When many scientists research the Li ion batteries, almost works have concentrated for electrochemical or electronic performance like capacity, voltage, electronic conductivity and charge density and so on until now. It is very important to develop the performance, but retaining the performance is also important. Cracking of microcrystalline of the electrode is main reason cause of cyclic degradation, in other words, capacity fading of Li ion batteries. Not only thermal expansion, but also elastic anisotropy can be induced several dislocations of crystal and cracks of electrode material, so the calculated anisotropic factors are important parameters to provide the degree of elastic anisotropy, the calculation method shown in equation (2.2.7) – (2.2.11).<sup>46</sup> At first, the shear anisotropic factors are the measurement of the anisotropy between atoms in different planes at a single crystal, and the value of factors is one at the isotropic crystal, while any value

bigger or smaller than unity becomes a measure of the degree of anisotropy of crystal. The shear anisotropic factors  $A_1$ ,  $A_2$  and  $A_3$  of pristine silicate structures and their semi-delithiated structures are shown in Fig.2.2.6. All shear anisotropic factors of silicate structures have near unity, however when extract Li ion, the values are farther from unity compared with lithiated silicate structure. Therefore, the probability of cracking or dislocation at the single crystal of silicates increased because anisotropy changes significantly when the charging/discharging process. At  $A_1$  and  $A_3$  parts, the anisotropy of Ni silicate is smallest, next is Fe silicate and Co silicate, finally Mn silicate. And Fe silicate has minimum anisotropy, next Ni and Co silicates. Especially the probability is biggest when transition metal is manganese, so occurs rapidly capacity degradation, also this tendency is well corresponds with the study result of elastic constants. And the reason is Jahn-teller distortion of  $Mn^{2+}/Mn^{3+}$  charge state as mentioned before.<sup>58</sup>

Second, Chung and Buessem suggested more practical criteria because when performed the study the elastic anisotropy, need to the measurement not a single crystal but polycrystalline. The percentage anisotropic factors that are measurements of elastic anisotropy of electrode compound which is isotropic characteristic using shear and bulk moduli, and the values of pristine silicate structures and their semi-delithiated structures are shown in Fig.2.2.7. The value of zero means that materials are perfectly isotropic, on the other hand, the largest possible anisotropic when has the value of hundred (100%). The elastic anisotropy of silicates shows different trend depending on the type of transition metal. The elastic anisotropy is very similar with fully lithiated silicates irrespective of the

type of transition metal, and the structures almost isotropic because shear and bulk percentage anisotropic factors have near 1 ~ 2%. Also, when Li ion extracted, the factors of all silicate increased which means elastic anisotropy grow bigger. However, the increased gap is different according to the transition metal. Firstly, the factors of Ni silicate are smallest increased to 8%, so probability cracking of electrode will increase at the least. The next order is Fe silicate, Co silicate and last is Mn silicate in the factors (11%, 14% and 29%). In particular, Mn silicate's shear and bulk percentage anisotropic factors are significantly increased compared with the rest of the factors increased alike and the result can be certified the remarkable low cyclability of Mn silicate.

### **2.3. Mechanical properties of binary multicomponent silicate materials $\text{Li}_2\text{Fe}_{0.5}\text{TM}_{0.5}\text{SiO}_4$ (TM = Mn, Ni and Co)**

Calculation of the optimized structure of binary multicomponent silicates based on iron silicate,  $\text{Li}_2\text{Fe}_{0.5}\text{TM}_{0.5}\text{SiO}_4$  (TM = Mn, Ni and Co) performed to find the favorable position of substituted transition metals. At first, schematics of  $\text{Li}_2\text{Fe}_{0.5}\text{Mn}_{0.5}\text{SiO}_4$  and  $\text{LiFe}_{0.5}\text{Mn}_{0.5}\text{SiO}_4$  are shown in Fig.2.3.1. In this figure, we know that fully lithiated structure is a stable polyhedral configuration at Fe, Mn, and Si elements, however when extract Li ions, distortion of polyhedral configuration has occurred. And the result means that semi-delithated structure is unstable than fully-lithiated structure. Next, schematics of  $\text{Li}_2\text{Fe}_{0.5}\text{Ni}_{0.5}\text{SiO}_4$  and  $\text{LiFe}_{0.5}\text{Ni}_{0.5}\text{SiO}_4$  are shown in Fig.2.3.2. In contrast with the

multicomponent  $\text{LiFe}_{0.5}\text{Mn}_{0.5}\text{SiO}_4$  silicate structure, the  $\text{LiFe}_{0.5}\text{Ni}_{0.5}\text{SiO}_4$  silicate structure shows the stable polyhedral configuration, hence multicomponent iron nickel silicate structure show the better cyclability than multicomponent iron manganese silicate structure. Finally,  $\text{Li}_2\text{Fe}_{0.5}\text{Ni}_{0.5}\text{SiO}_4$  and  $\text{LiFe}_{0.5}\text{Ni}_{0.5}\text{SiO}_4$  are shown in Fig.2.3.3, and the polyhedral shape of the structures are shown intermediate stability between previous two structures.

### **2.3.1. Elastic constants, several moduli and Poisson ratio**

The elastic constants of the silicates are shown in Table.2.3.1. In this result, elastic constants of semi-delithiated multicomponent silicates have intermediate value about combination transition metals. Meanwhile, shear moduli of multicomponent silicates are shown in Fig.2.3.4. The values of fully lithiated structures  $\text{Li}_2\text{Fe}_{0.5}\text{TM}_{0.5}\text{SiO}_4$  is a little different compared with pristine silicate  $\text{Li}_2\text{TMSiO}_4$ . When Li ions extract, the values less decreased to 34GPa than pristine silicates that all values under 30GPa. Besides, the decreased value is very similar regardless of the combination of transition metals. In this result, we know that Fe metal suppresses the Jahn-teller distortion of  $\text{Mn}^{3+}$  through the charge distribution to make stable Mn electronic structure at first. And other metals like Al also suppress the Jahn-teller distortion, and this effect has well demonstrated by the previous study and validate experiment. Bulk moduli of the multicomponent silicates are shown in Fig.2.3.5. The values are very similar with pristine silicates when fully lithiated state and this tendency same with shear moduli, but the tendency is different when semi-

delthiated state. At shear moduli, the values close to higher value between two pristine silicates values, on the other hand, the values are the average value between two pristine silicates values. In other words, doping the other transition metals suppressed Jahn-teller distortion of  $Mn^{3+}$ , and silicate polycrystalline structure is affected by more stable transition metal in shear direction, whereas the bulk is influenced by all transition metals, hence shear and bulk moduli have the values as previously mentioned. Next, young modulus and Poisson ratio are shown in Fig.2.3.6 and Fig.2.3.7. At first, young modulus of multicomponent silicates has similar value, and the value almost same with the value of pristine silicates however when extract Li ions, the value is less decreased. The reason is that not only suppression of Jahn-teller distortion, but also combination of different transition metal is declined electrostatic repulsion of cation.<sup>36</sup> And Poisson ratio decreased at multicomponent silicates and the tendency different from pristine silicates.

### **2.3.2. Shear and percentage anisotropic factors**

Finally, shear and percentage anisotropic factors of binary multicomponent silicates are calculated, and show the possibility of dislocation and cracking of the multicomponent silicates, additionally compared with pristine silicates. Shear anisotropic factors are shown in Fig.2.3.8. At first, all shear anisotropic factors very similar with pristine silicates. However when Li ions extracted,  $A_1$  and  $A_2$  values are closed to unity, and this result means that anisotropy is diminished although the charging/discharging

process.  $A_3$  value is almost same as pristine silicates at lithiated and semi-delithiated states. Totally, multicomponent silicate crystal structures have almost isotropic structure even the semi-delithiated structures for effect decreased electrostatic repulsion between transition metals.

Next is the shear percentage anisotropic factors are shown in 2.3.9a. Fully lithiated structure, shear percentage anisotropic factor is almost the same with pristine and multicomponent silicates. (ca. 1~3%). When extract Li ions, the values are increased that  $\text{LiFe}_{0.5}\text{Mn}_{0.5}\text{SiO}_4$  has 11%,  $\text{LiFe}_{0.5}\text{Ni}_{0.5}\text{SiO}_4$  has 6% and  $\text{LiFe}_{0.5}\text{Co}_{0.5}\text{SiO}_4$  has 7%, and the increased gap is smaller than pristine silicates. In this study, we know that iron suppresses the manganese anisotropy at silicate structures, and a combination of transition metals suppresses the shear anisotropy, therefore multicomponent silicates prevent the shear directional cracking during Li insertion/extraction process. Bulk percentage anisotropic factors are shown in Fig.2.3.9b. Original structures  $\text{Li}_2\text{Fe}_{0.5}\text{TM}_{0.5}\text{SiO}_4$  (TM = Mn, Ni and Co) have similar the bulk percentage anisotropic factors 1 ~ 2%. When extract Li ions, the values are increased all structures,  $\text{LiFe}_{0.5}\text{Mn}_{0.5}\text{SiO}_4$  has 10%,  $\text{Li}_2\text{Fe}_{0.5}\text{Ni}_{0.5}\text{SiO}_4$  has 11% and  $\text{Li}_2\text{Fe}_{0.5}\text{Co}_{0.5}\text{SiO}_4$  has 8%. However, the values are higher than pristine silicates except for manganese silicate. For the research, remarkable anisotropy of manganese can be suppressed with multicomponent system, but anisotropy is a little increased at  $\text{Li}_2\text{Fe}_{0.5}\text{Ni}_{0.5}\text{SiO}_4$  multicomponent system. It is speculated about the calculation results. Firstly, electrostatic repulsion is not decreased at Fe between Ni at the entire bulk system, so the anisotropic factors not decreased because Fe does little to contribute to the Ni silicates.<sup>36</sup> Secondly,

percentage anisotropic factors are calculated using the maximum and minimum values of modulus, and the gap is bigger and bigger, calculated the factors are more increased. Because the calculated gap Fe-Ni multicomponent silicate is bigger than pristine silicate structures, the factors are increased, but the difference is a little.

## 2.4. Summary

In this study, the mechanical properties of pristine orthosilicate that have four different transition metal types  $\text{Li}_2\text{TMSiO}_4$  (TM = Fe, Mn, Ni and Co) cathode materials have been investigated using first principles density functional study calculations. Furthermore, the mechanical properties of binary multicomponent orthosilicate based on the family of Fe  $\text{Li}_2\text{Fe}_{0.5}\text{TM}_{0.5}\text{SiO}_4$  (TM = Mn, Ni and Co) cathode materials have been calculated using the same method with pristine orthosilicate's. At first, all fully delithiated structures are cannot calculate mechanical properties because the appropriated fitting of the structures is impossible, and the results have good agreement with previous experimental results.

The several moduli like bulk, shear and young of pristine orthosilicates have similar values, and the several moduli of intermediate delithiated state orthosilicates values are decreased. And the degree of reduction is very similar with almost orthosilicates except Mn silicate  $\text{Li}_x\text{MnSiO}_4$  ( $x= 2, 1$ ), and the moduli of Mn silicate are more decreased than other transition metal silicates because of Jahn-teller distortion occur with  $\text{Mn}^{2+}/\text{Mn}^{3+}$  discharge

process that destabilizes the host structure. Poisson ratio of all structures has a similar value of 0.28 ~ 0.3 even though extracted Li ions. Shear and percentage anisotropic factors are increased when extracted Li ions. And the degree of increased is biggest at Mn silicate because of Jahn-teller distortion.

Several moduli of binary multicomponent orthosilicates are very similar with pristine silicates, however when extracted Li ions, the values are less decreased than pristine orthosilicates. The binary system's Poisson ratio has similar value with pristine system, too, but the value is decreased to 0.25 when extract Li ions, and the tendency is different from the pristine system. The tendency of shear and percentage anisotropic factors of binary multicomponent silicates is the same with pristine silicates, but the increased gap is different.

The reasons for the difference being that the doping of other transition metal at Mn silicate is suppressed of Jahn-tell distortion caused by  $Mn^{3+}$ . Hence, the huge difference that only appeared pristine Mn silicate is shrinking, and the gap is closing compared with other multicomponent silicates cathode materials. Moreover, at multicomponent one, the inclusion of more than one type of transition metals is decreased strong repulsion of the pristine Fe silicate system, therefore mechanical behavior of multicomponent silicates is to be different from the pristine silicate's behavior. The mechanical properties of the silicates show that binary multicomponent system has superior performance than pristine one, and it means multicomponent silicates prevent the probability of crack of electrode particle, so have better cyclability than pristine system. Consequently, the calculation results mean that

silicates can have different mechanical characteristics according to types of transition metals, or composition ratio of transition metals. Of course, further experimental work should be progressed to validate the conclusion, nevertheless, the research results can suggest such strategy of design of silicate cathode materials of lithium ion batteries not only electrochemical but also mechanical aspect, also help the prediction of macro behavior of electrode for scale bridging, multiscale analysis.

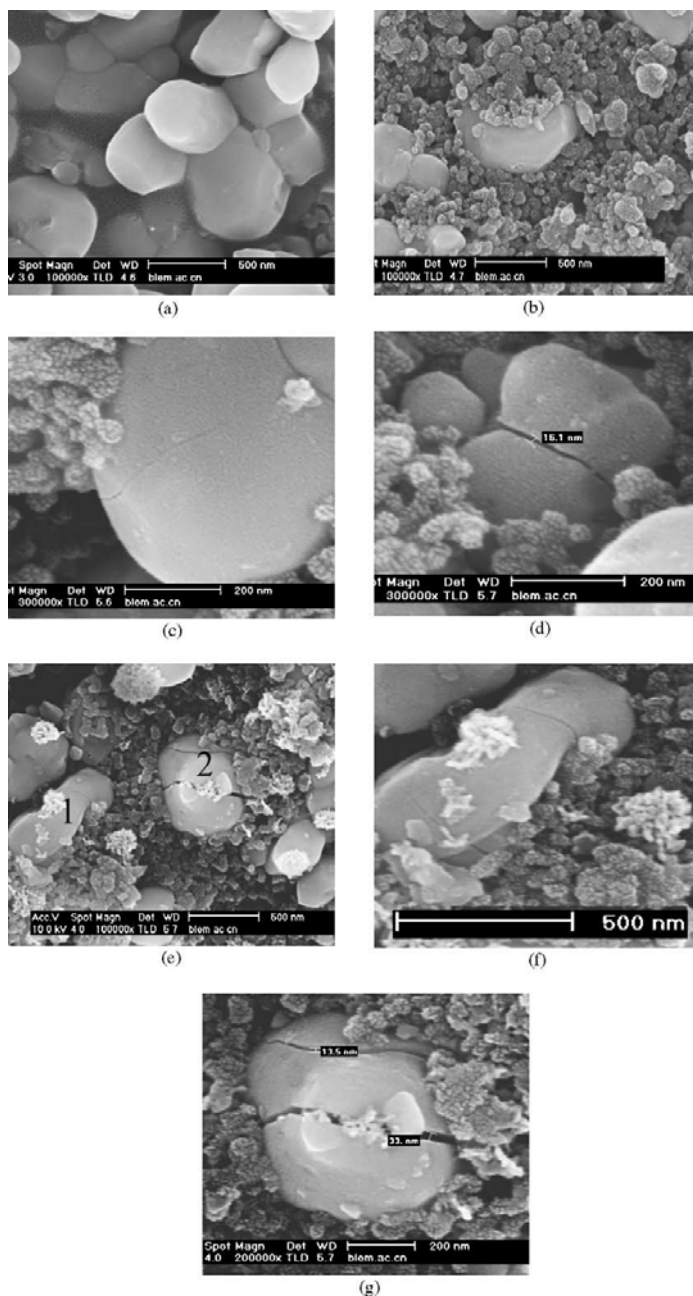
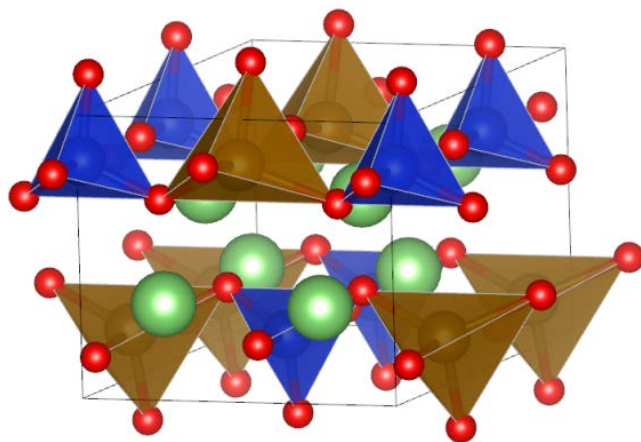
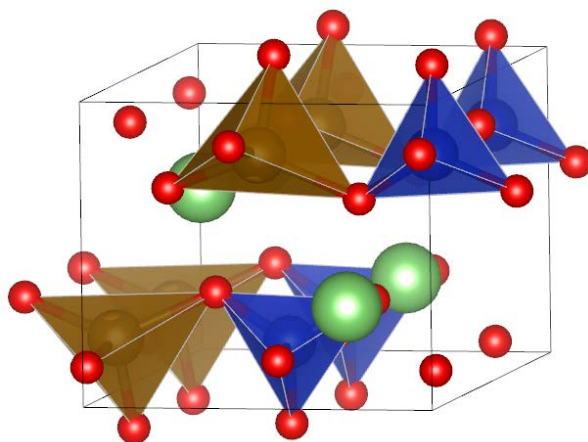


**Figure 2.1.** The SEM images of  $\text{LiFePO}_4$ . (a) The prepared sample; (b) the electrode before cycling; (c) the electrode after 10 cycles; (d) the electrode after 30cycles; (e) the electrode after 60 cycles; (f) particle 1 in the image (e); and (g) particle 2 in the image (e).<sup>45</sup>

**(a)**



**(b)**



**(c)**

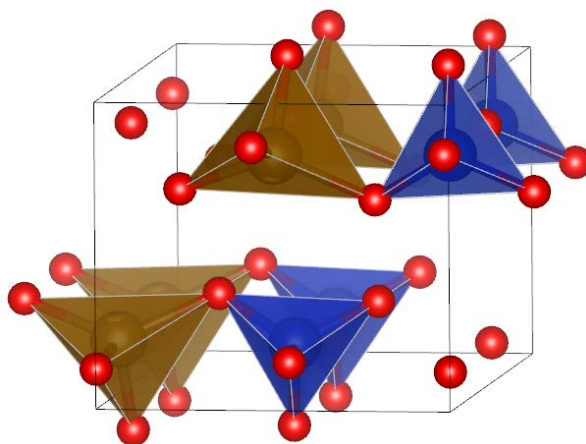
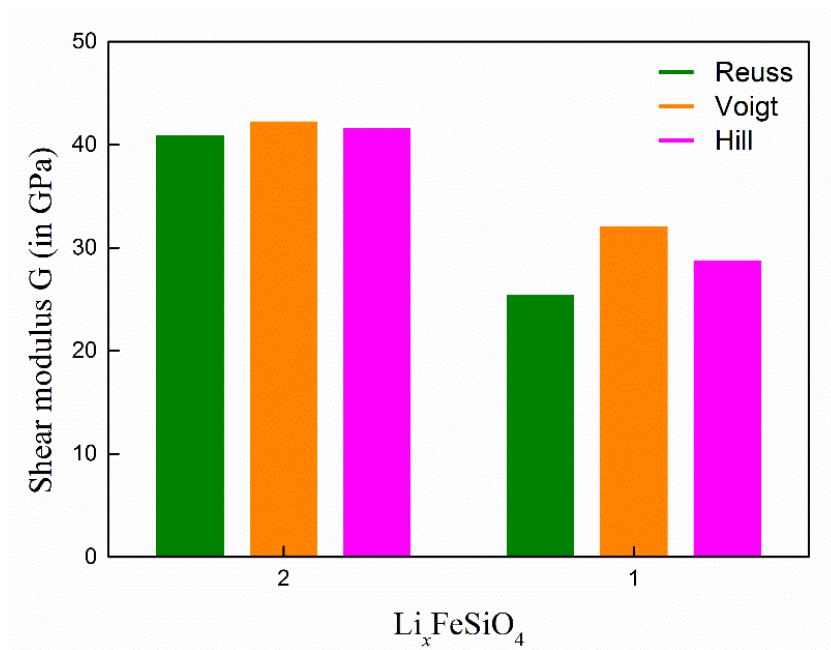
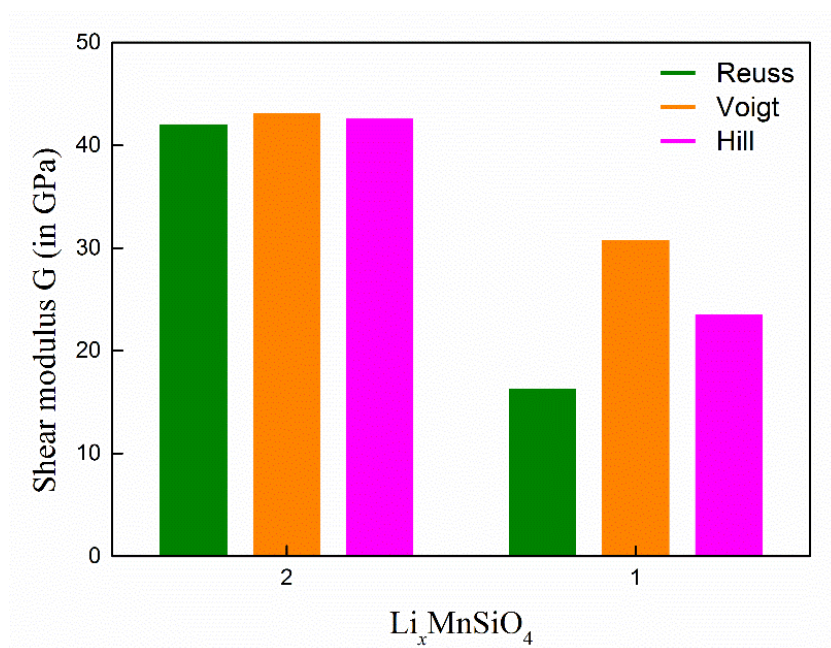


**Fig.2.2.1. Schematics of silicate structure (a)  $\text{Li}_2\text{TMSiO}_4$ , their semi-delithiated structure (b)  $\text{LiTMSiO}_4$  and delithiated structure (c)  $\text{TMSiO}_4$  (TM = Fe, Mn, Ni and Co)**

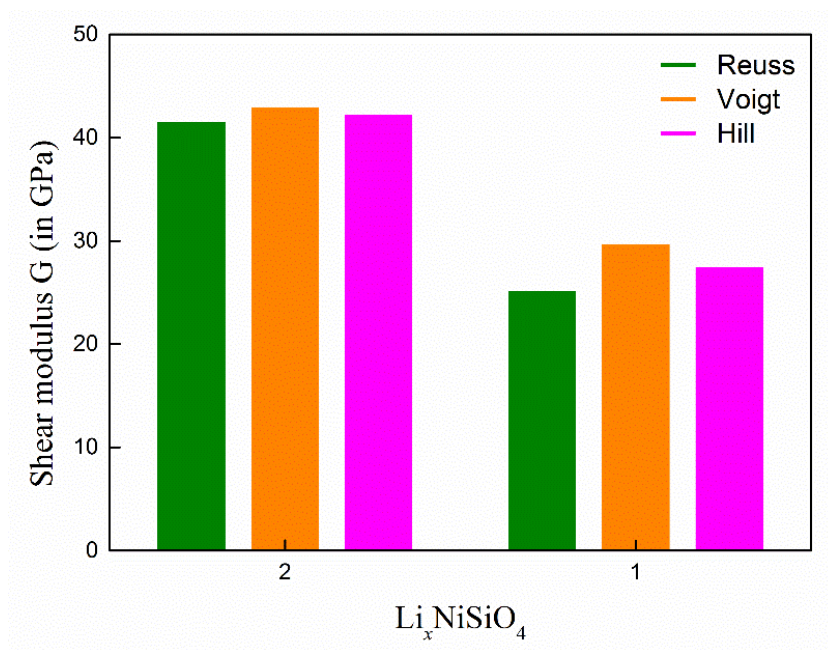
**(a)**



**(b)**



(c)



(d)

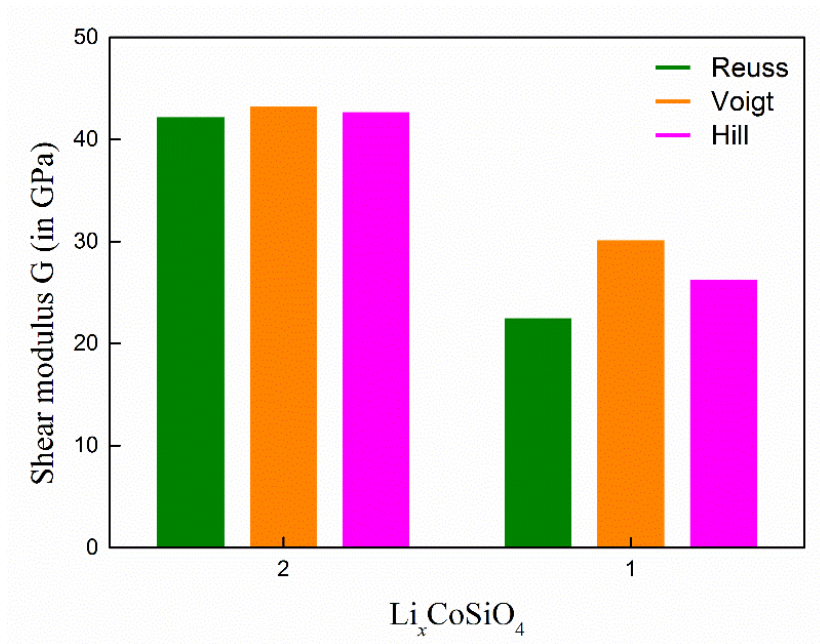
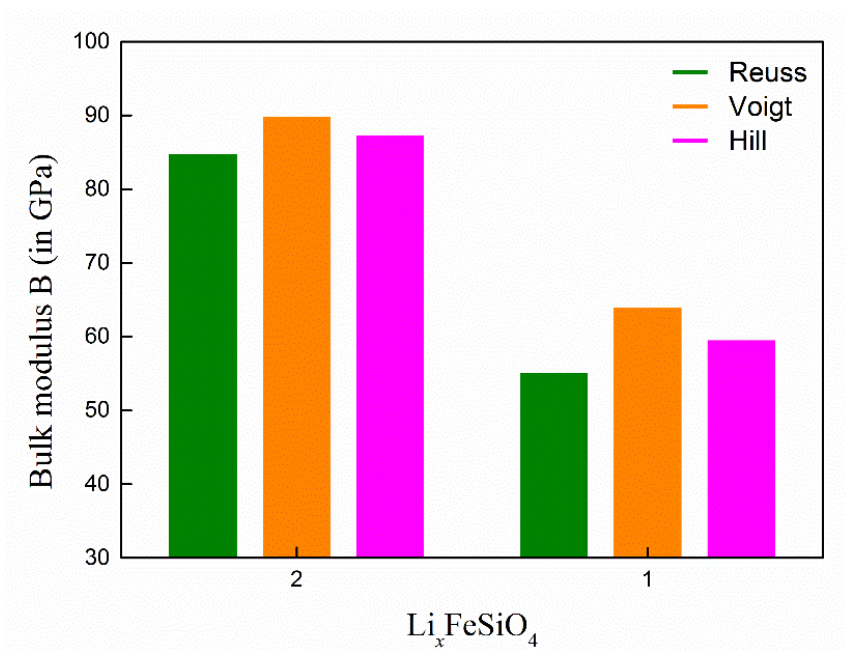
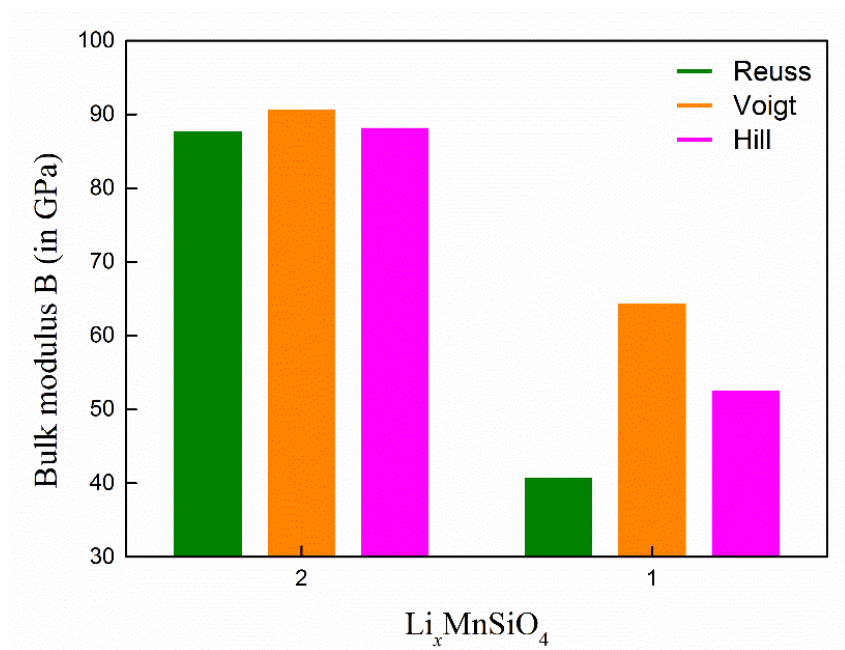


**Fig.2.2.2. Shear moduli of silicates material  $\text{Li}_2\text{TMSiO}_4$  and their semi-delithiated structures  $\text{LiTMSiO}_4$  (TM = Fe, Mn, Ni and Co) (a)  $\text{Li}_2\text{FeSiO}_4$  and  $\text{LiFeSiO}_4$ , (b)  $\text{Li}_2\text{MnSiO}_4$  and  $\text{LiMnSiO}_4$ , (c)  $\text{Li}_2\text{NiSiO}_4$  and  $\text{LiNiSiO}_4$  and (d)  $\text{Li}_2\text{CoSiO}_4$  and  $\text{LiCoSiO}_4$ .**

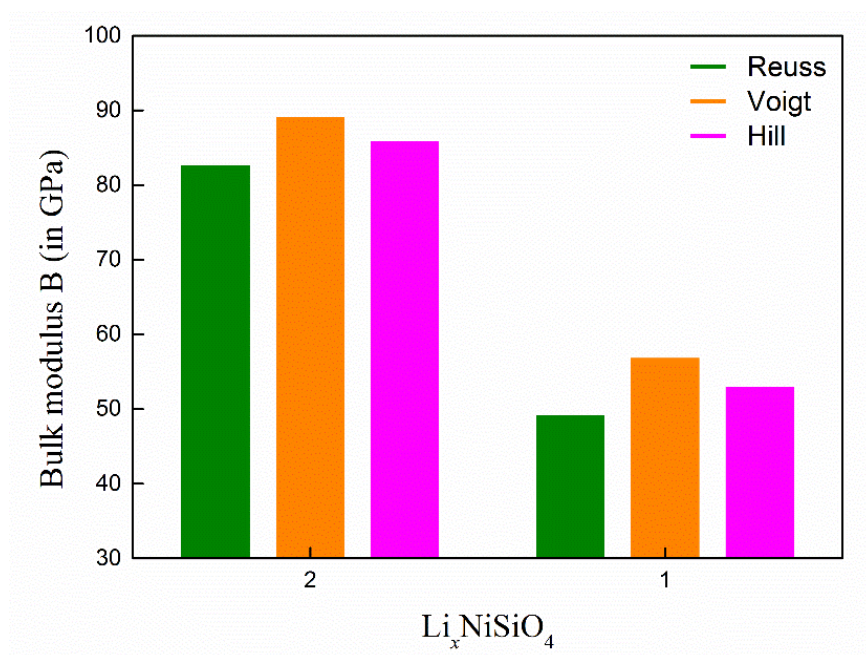
**(a)**



**(b)**



(c)



(d)

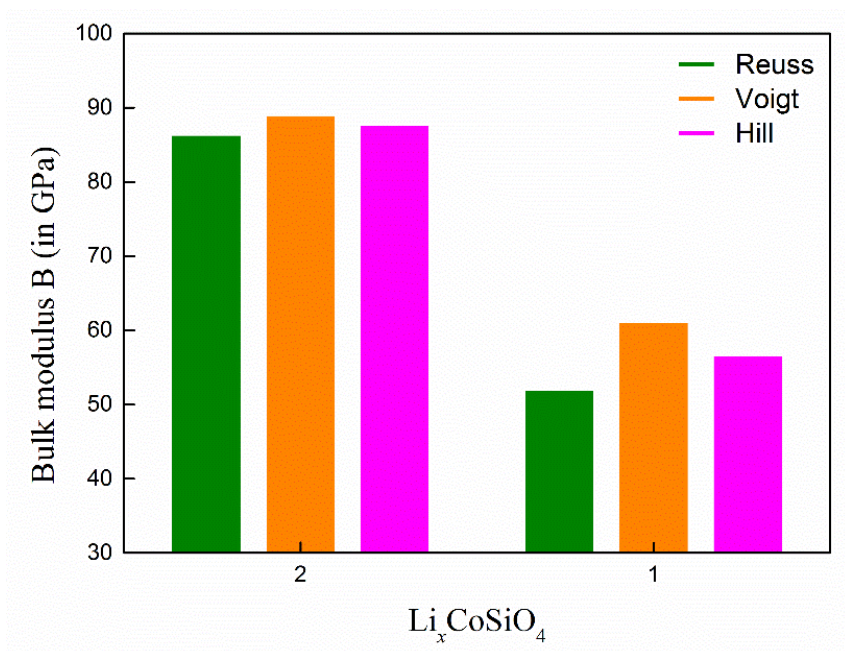


**Fig.2.2.3. Bulk moduli of silicates material  $\text{Li}_2\text{TMSiO}_4$  and their semi-delithiated structures  $\text{LiTMSiO}_4$  (TM = Fe, Mn, Ni and Co) (a)  $\text{Li}_2\text{FeSiO}_4$  and  $\text{LiFeSiO}_4$ , (b)  $\text{Li}_2\text{MnSiO}_4$  and  $\text{LiMnSiO}_4$ , (c)  $\text{Li}_2\text{NiSiO}_4$  and  $\text{LiNiSiO}_4$  and (d)  $\text{Li}_2\text{CoSiO}_4$  and  $\text{LiCoSiO}_4$ .**

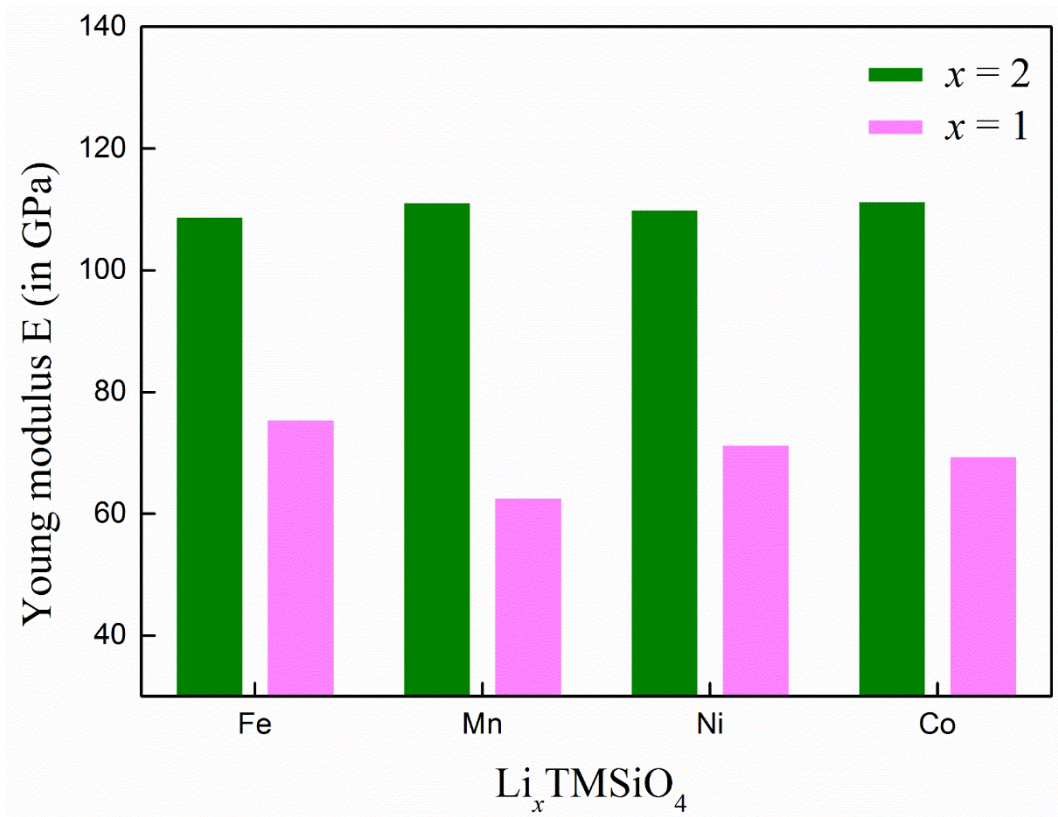


**Fig.2.2.4.** Young moduli of silicates material  $\text{Li}_2\text{TMSiO}_4$  and their semi-delithiated structures  $\text{LiTMSiO}_4$  (TM = Fe, Mn, Ni and Co), and down label show the type of transition metal, and green bars are  $\text{Li}_2\text{TMSiO}_4$  and pink bars are  $\text{LiTMSiO}_4$  (TM = Fe, Mn, Ni and Co).

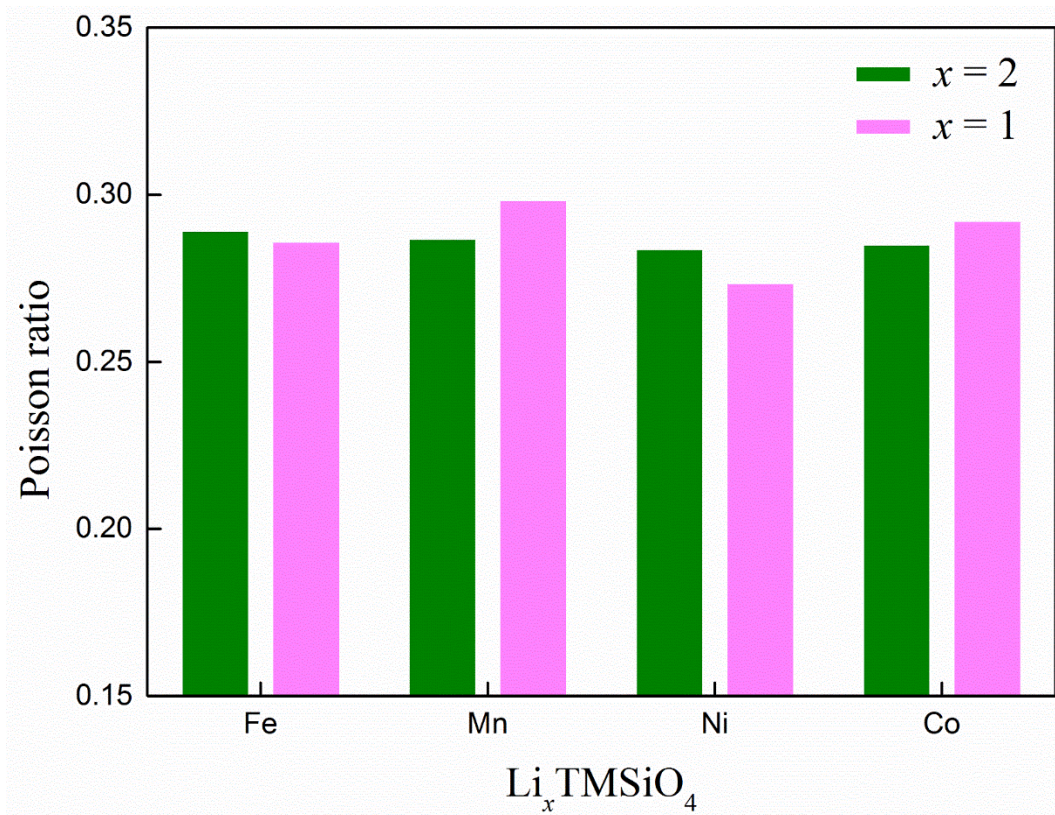
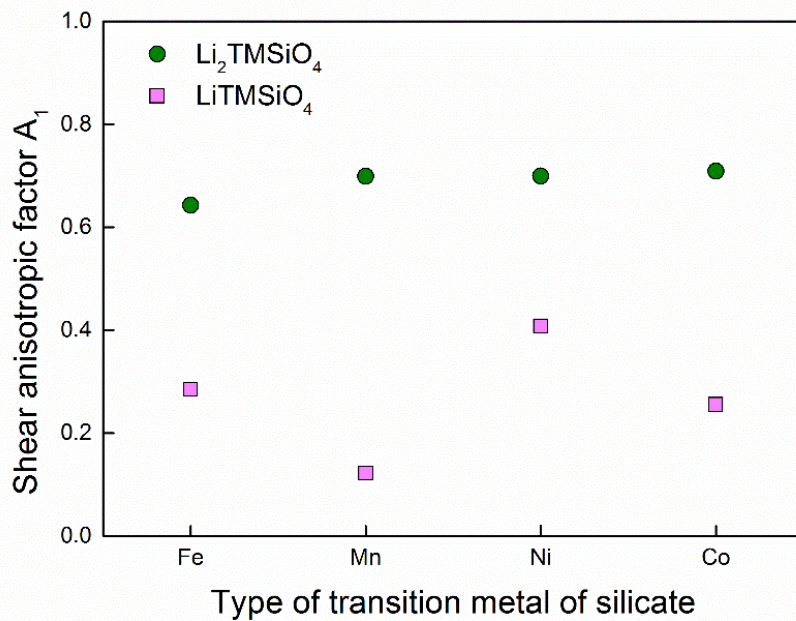
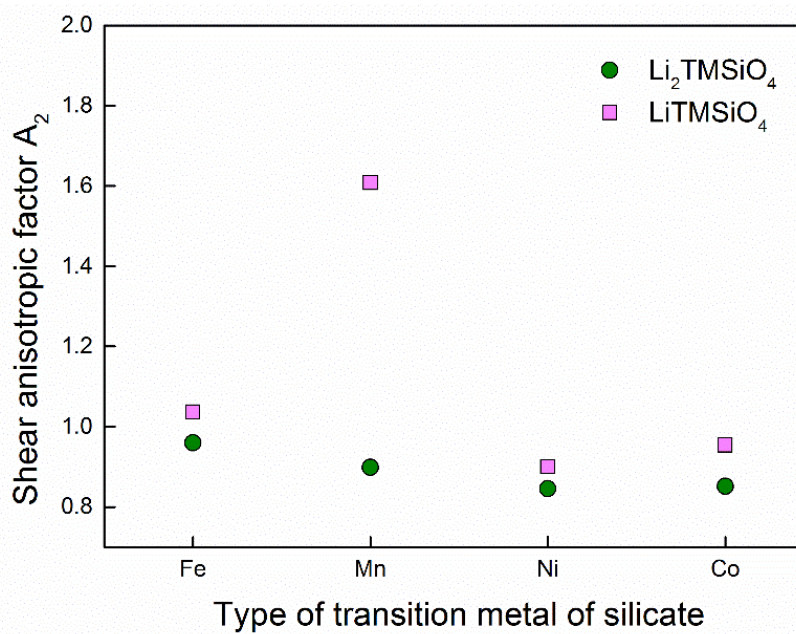


**Fig.2.2.5. Poisson ratio of silicates material  $\text{Li}_2\text{TMSiO}_4$  and their semi-delithiated structures  $\text{LiTMSiO}_4$  (TM = Fe, Mn, Ni and Co), and down label show the type of transition metal, and green bars are  $\text{Li}_2\text{TMSiO}_4$  and pink bars are  $\text{LiTMSiO}_4$  (TM = Fe, Mn, Ni and Co).**

(a)



(b)



(c)

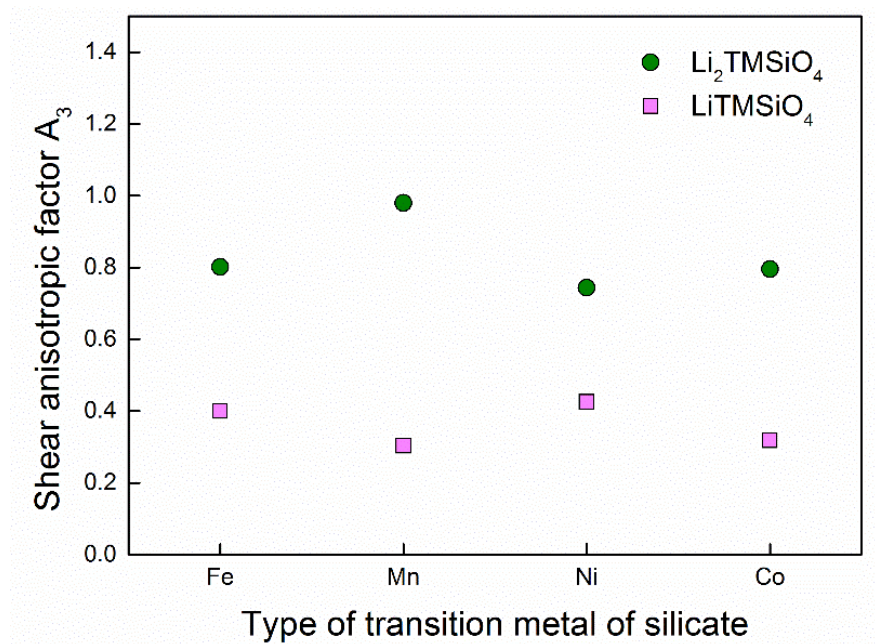
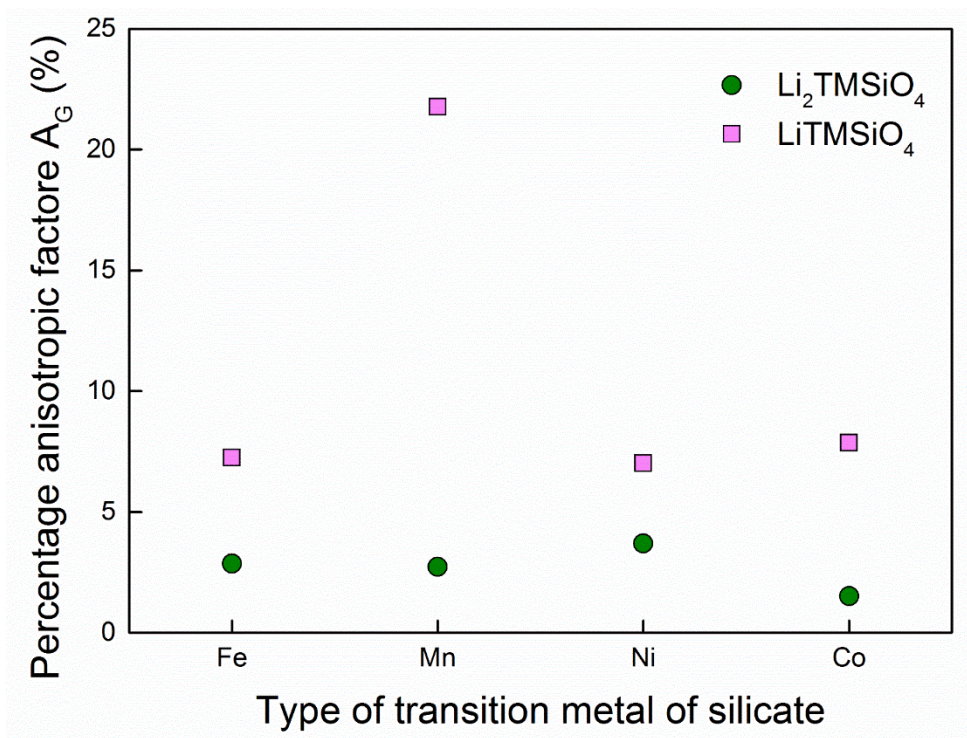


**Fig.2.2.6. Shear anisotropic factors (a)  $A_1$ , (b)  $A_2$  and (c)  $A_3$  of silicates material  $\text{Li}_2\text{TMSiO}_4$  and their semi-delithiated structures  $\text{LiTMSiO}_4$  (TM = Fe, Mn, Ni and Co), and down label show the type of transition metal, and green points are  $\text{Li}_2\text{TMSiO}_4$  and pink points are  $\text{LiTMSiO}_4$  (TM = Fe, Mn, Ni and Co).**

(a)



(b)

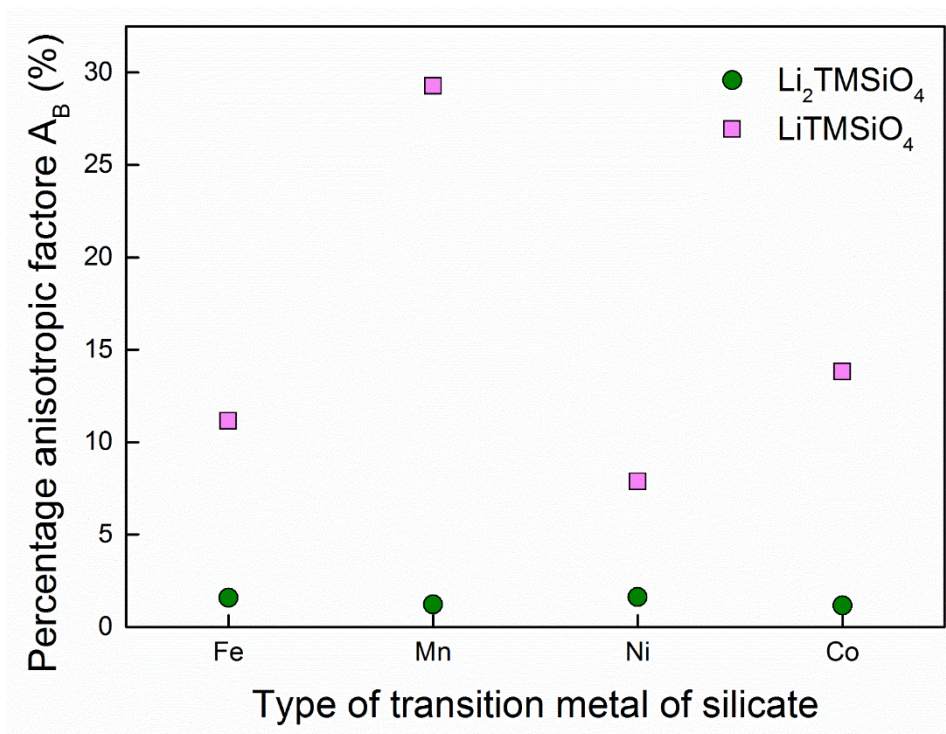
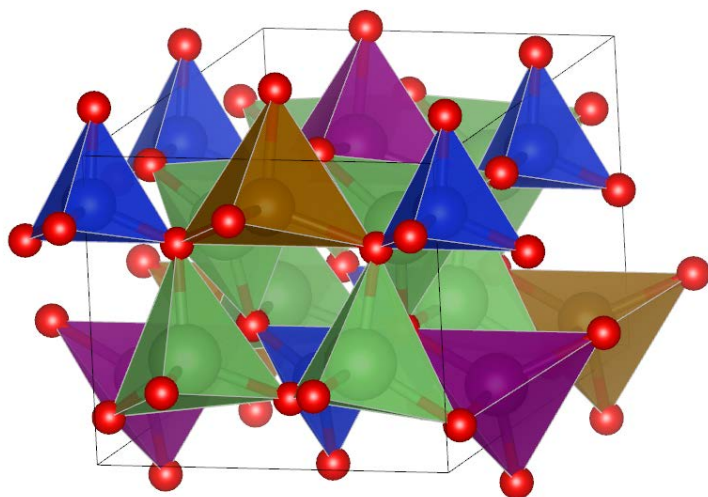


**Fig.2.2.7. Shear percentage anisotropic factors (a)  $A_G$  and bulk percentage anisotropic factors (b)  $A_B$  of silicates material  $Li_2TMSiO_4$  and their semi-delithiated structures  $LiTMSiO_4$  (TM = Fe, Mn, Ni and Co), and down label show the type of transition metal, and green points are  $Li_2TMSiO_4$  and pink points are  $LiTMSiO_4$  (TM = Fe, Mn, Ni and Co).**

(a)



(b)

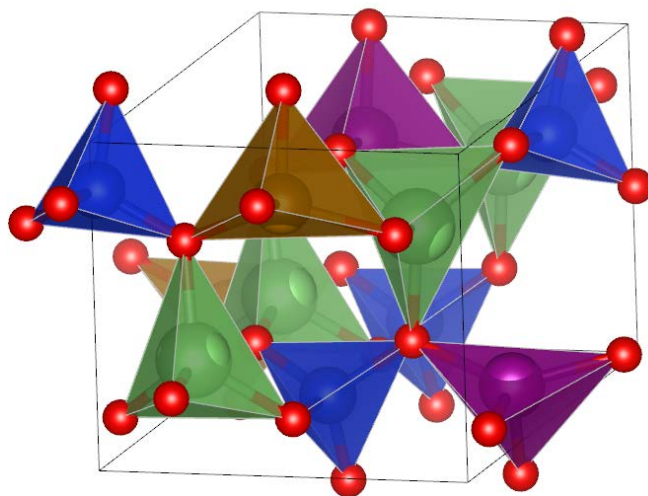
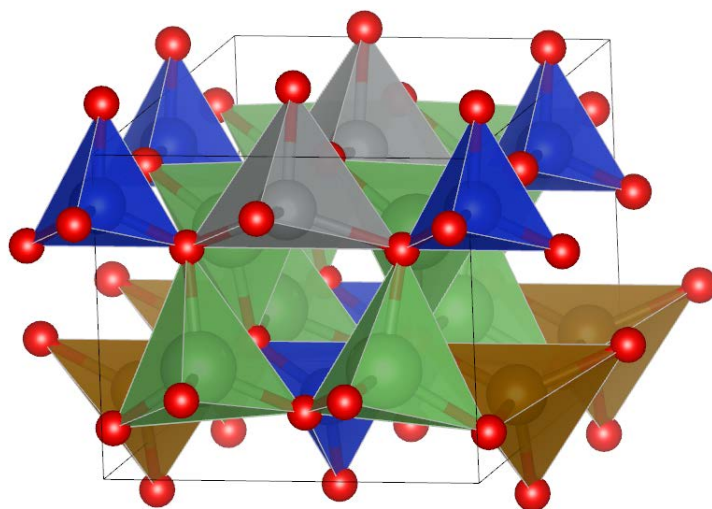


**Fig.2.3.1.** Entire schematics of multicomponent silicate structure (a)  $\text{Li}_2\text{MnSiO}_4$  and their semi-delithiated structure (b)  $\text{LiMnSiO}_4$ .

(a)



(b)

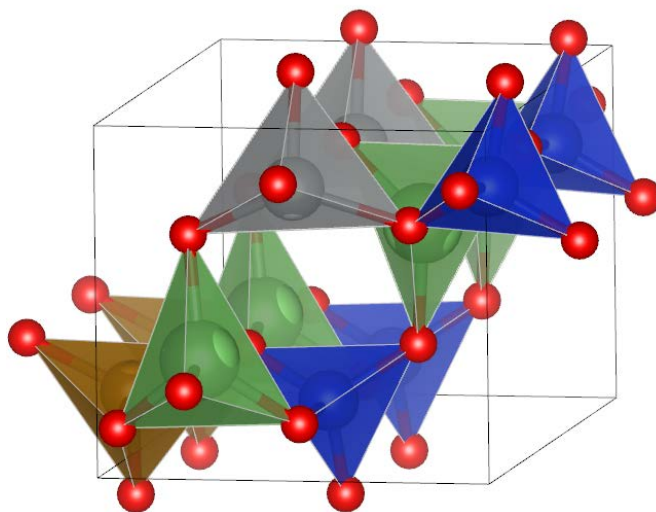
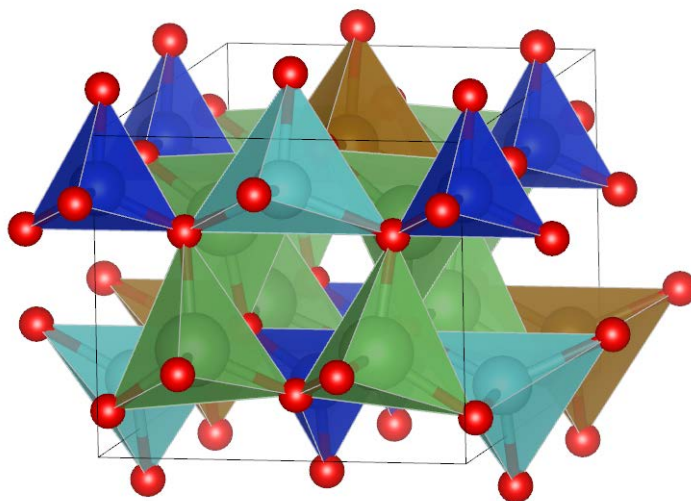


**Fig.2.3.2. Entire schematics of multicomponent silicate structure (a)  $\text{Li}_2\text{NiSiO}_4$  and their semi-delithiated structure (b)  $\text{LiNiSiO}_4$ .**

(a)



(b)

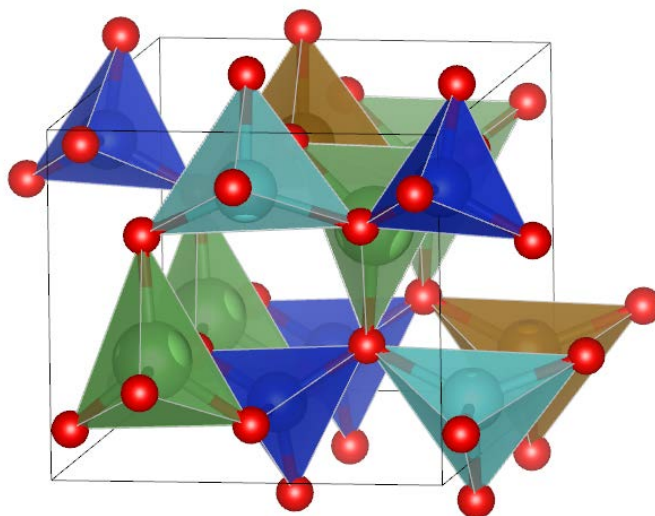
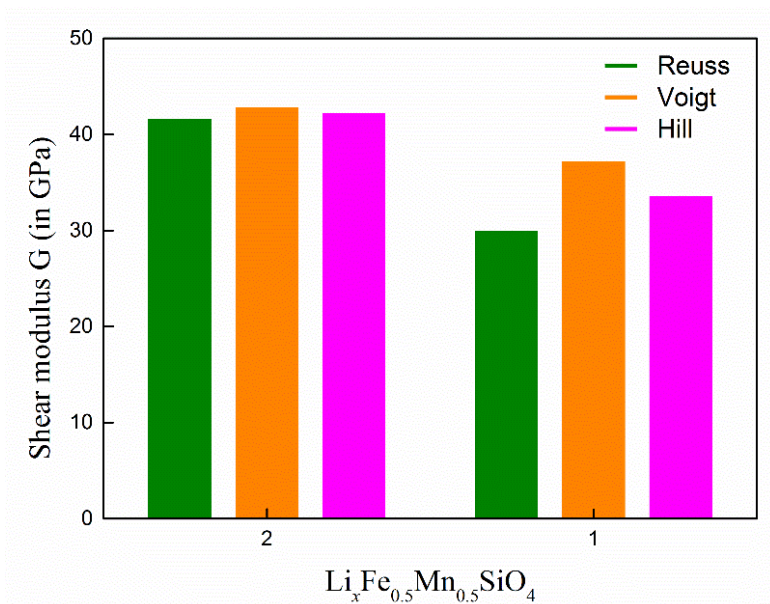
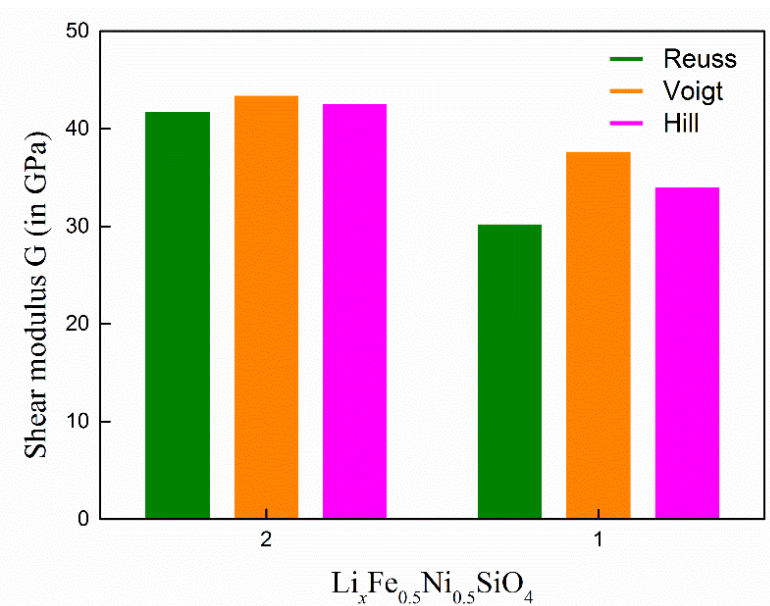


**Fig.2.3.3. Entire schematics of multicomponent silicate structure (a)  $\text{Li}_2\text{CoSiO}_4$  and their semi-delithiated structure (b)  $\text{LiCoSiO}_4$ .**

(a)



(b)



(c)

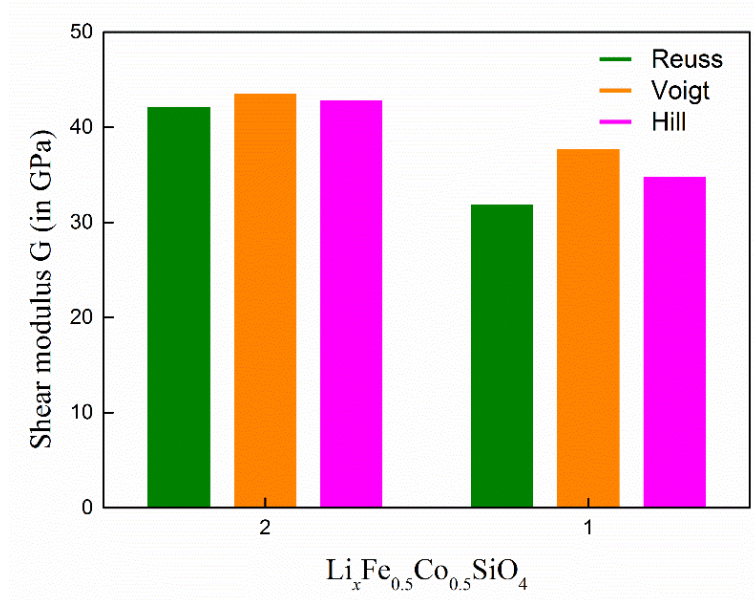
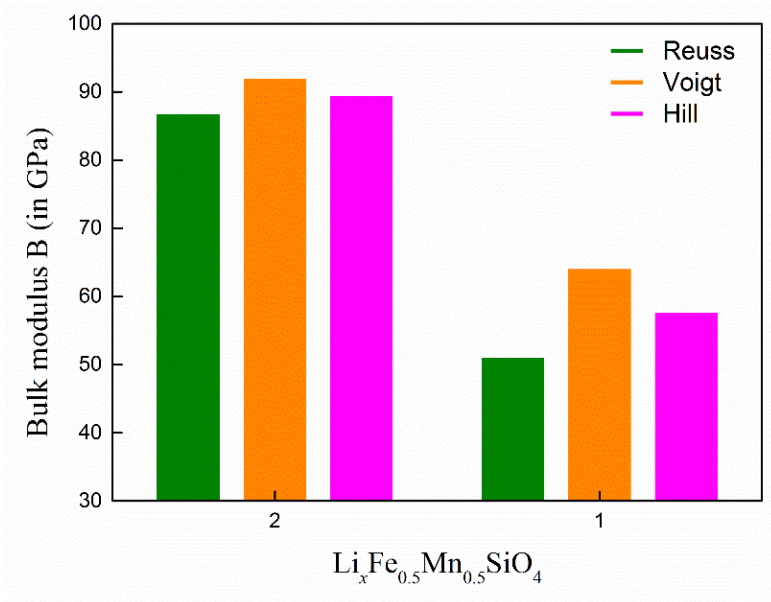
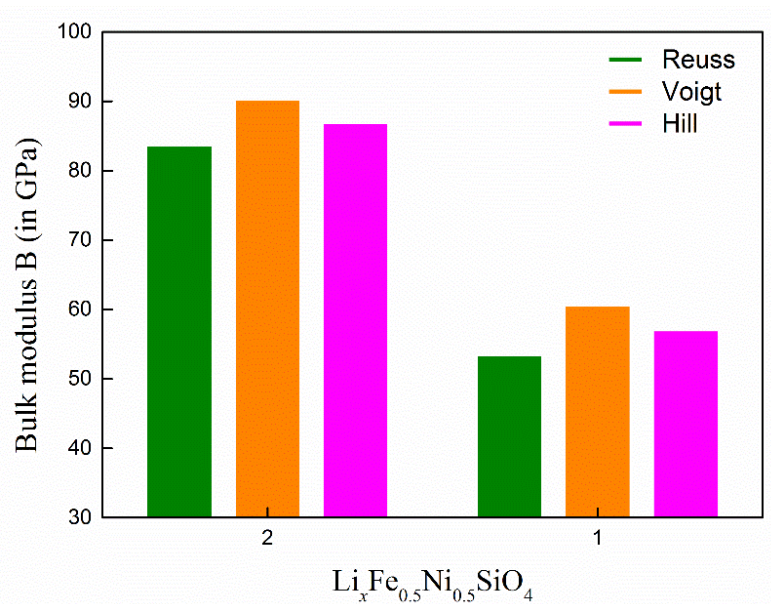


**Fig.2.3.4. Shear moduli of multicomponent silicates material  $\text{Li}_2\text{Fe}_{0.5}\text{TM}_{0.5}\text{SiO}_4$  and their semi-delithiated structures  $\text{LiFe}_{0.5}\text{TM}_{0.5}\text{SiO}_4$  (TM = Mn, Ni and Co) (a)  $\text{Li}_2\text{Fe}_{0.5}\text{Mn}_{0.5}\text{SiO}_4$  and  $\text{LiFe}_{0.5}\text{Mn}_{0.5}\text{SiO}_4$ , (b)  $\text{Li}_2\text{Fe}_{0.5}\text{Ni}_{0.5}\text{SiO}_4$  and  $\text{LiFe}_{0.5}\text{Ni}_{0.5}\text{SiO}_4$ , and (c)  $\text{Li}_2\text{Fe}_{0.5}\text{Co}_{0.5}\text{SiO}_4$  and  $\text{LiFe}_{0.5}\text{Co}_{0.5}\text{SiO}_4$ .**

**(a)**



**(b)**



(c)

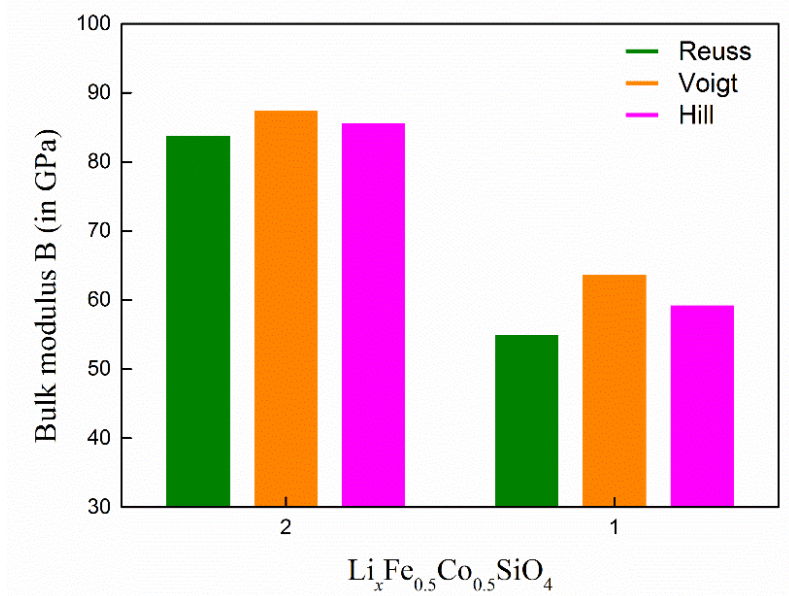


**Fig.2.3.5. Bulk moduli of multicomponent silicates material  $\text{Li}_2\text{Fe}_{0.5}\text{TM}_{0.5}\text{SiO}_4$  and their semi-delithiated structures  $\text{LiFe}_{0.5}\text{TM}_{0.5}\text{SiO}_4$  (TM = Mn, Ni and Co) (a)  $\text{Li}_2\text{Fe}_{0.5}\text{Mn}_{0.5}\text{SiO}_4$  and  $\text{LiFe}_{0.5}\text{Mn}_{0.5}\text{SiO}_4$ , (b)  $\text{Li}_2\text{Fe}_{0.5}\text{Ni}_{0.5}\text{SiO}_4$  and  $\text{LiFe}_{0.5}\text{Ni}_{0.5}\text{SiO}_4$ , and (c)  $\text{Li}_2\text{Fe}_{0.5}\text{Co}_{0.5}\text{SiO}_4$  and  $\text{LiFe}_{0.5}\text{Co}_{0.5}\text{SiO}_4$ .**

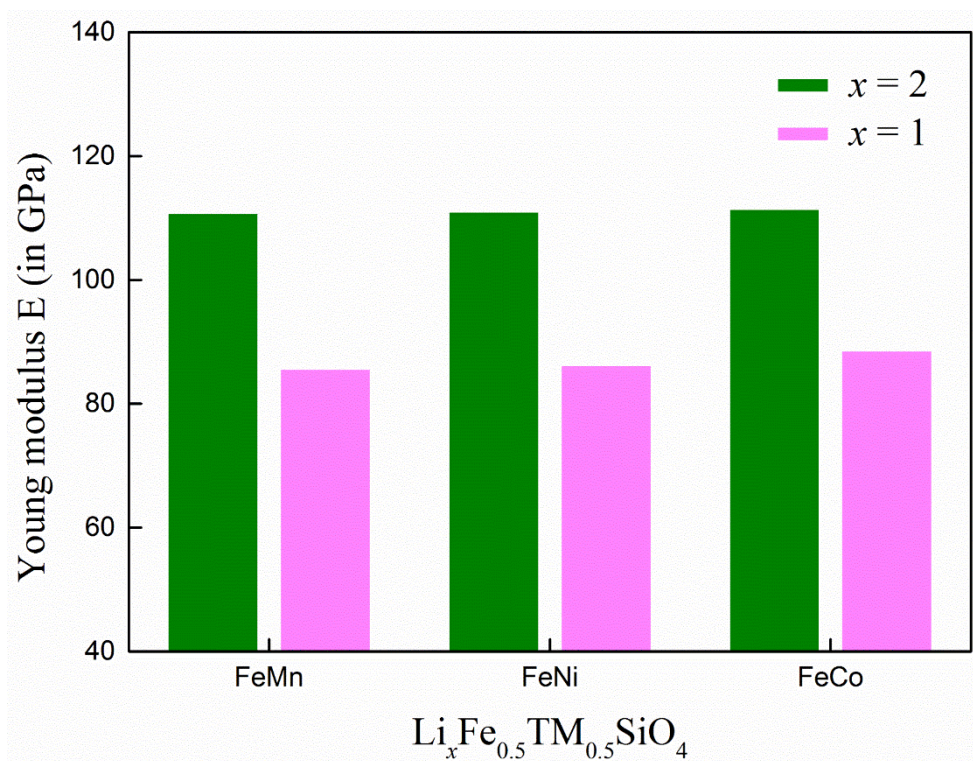


**Fig.2.3.6. Young moduli of multicomponent silicates material  $\text{Li}_2\text{Fe}_{0.5}\text{TM}_{0.5}\text{SiO}_4$  and their semi-delithiated structures  $\text{LiFe}_{0.5}\text{TM}_{0.5}\text{SiO}_4$  (TM = Mn, Ni and Co), down label show the combination of transition metals  $\text{Li}_2\text{Fe}_{0.5}\text{Mn}_{0.5}\text{SiO}_4$  and  $\text{LiFe}_{0.5}\text{Mn}_{0.5}\text{SiO}_4$ ,  $\text{Li}_2\text{Fe}_{0.5}\text{Ni}_{0.5}\text{SiO}_4$  and  $\text{LiFe}_{0.5}\text{Ni}_{0.5}\text{SiO}_4$ , and  $\text{Li}_2\text{Fe}_{0.5}\text{Co}_{0.5}\text{SiO}_4$  and  $\text{LiFe}_{0.5}\text{Co}_{0.5}\text{SiO}_4$ . Green bars are  $\text{Li}_2\text{Fe}_{0.5}\text{TM}_{0.5}\text{SiO}_4$  and pink bars are  $\text{LiFe}_{0.5}\text{TM}_{0.5}\text{SiO}_4$ .**

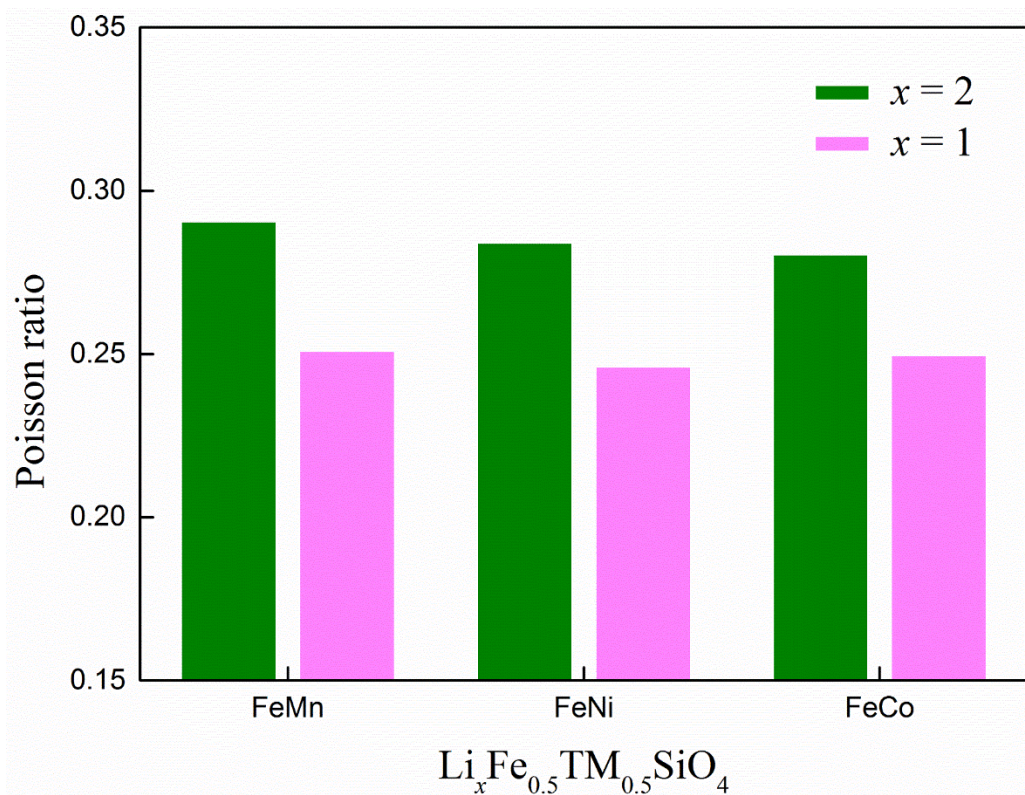
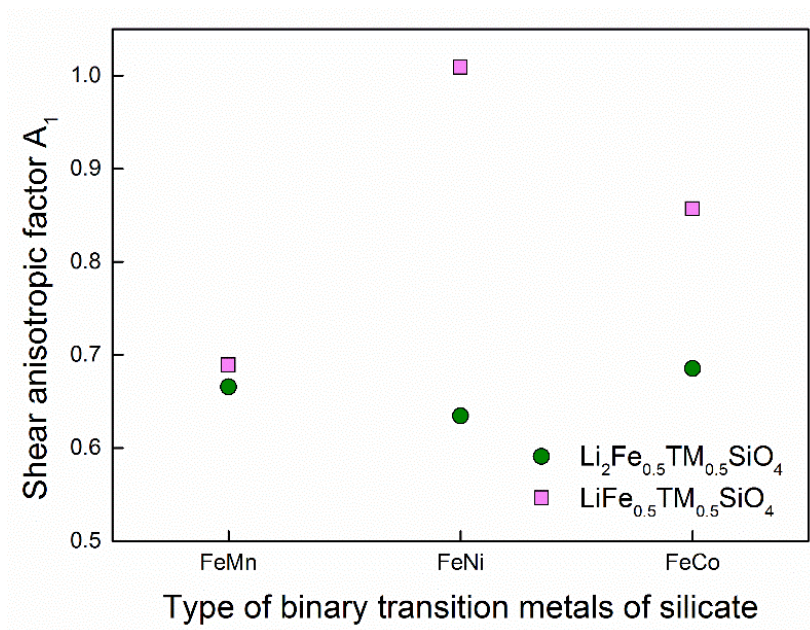
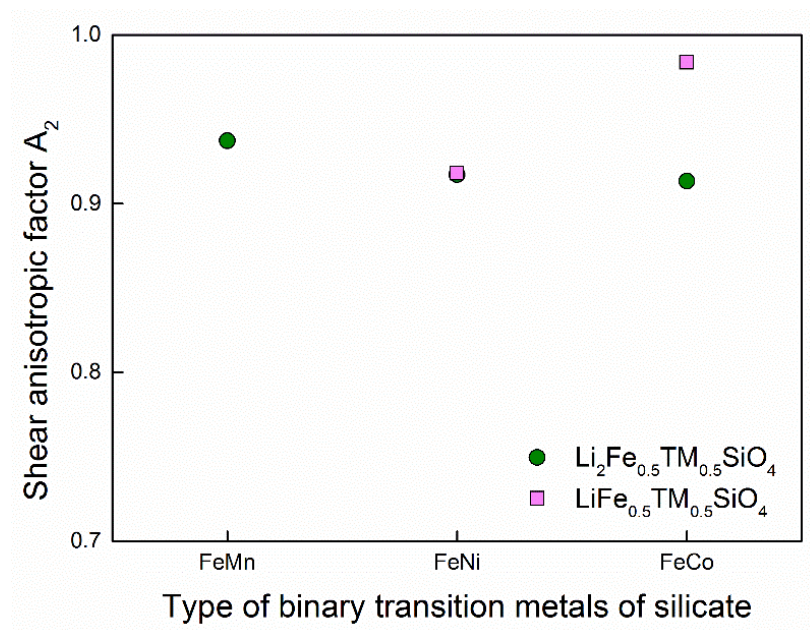


**Fig.2.3.7. Poisson ratio of multicomponent silicates material  $\text{Li}_2\text{Fe}_{0.5}\text{TM}_{0.5}\text{SiO}_4$  and their semi-delithiated structures  $\text{LiFe}_{0.5}\text{TM}_{0.5}\text{SiO}_4$  (TM = Mn, Ni and Co), down label show the combination of transition metals  $\text{Li}_2\text{Fe}_{0.5}\text{Mn}_{0.5}\text{SiO}_4$  and  $\text{LiFe}_{0.5}\text{Mn}_{0.5}\text{SiO}_4$ ,  $\text{Li}_2\text{Fe}_{0.5}\text{Ni}_{0.5}\text{SiO}_4$  and  $\text{LiFe}_{0.5}\text{Ni}_{0.5}\text{SiO}_4$ , and  $\text{Li}_2\text{Fe}_{0.5}\text{Co}_{0.5}\text{SiO}_4$  and  $\text{LiFe}_{0.5}\text{Co}_{0.5}\text{SiO}_4$ . Green bars are  $\text{Li}_2\text{Fe}_{0.5}\text{TM}_{0.5}\text{SiO}_4$  and pink bars are  $\text{LiFe}_{0.5}\text{TM}_{0.5}\text{SiO}_4$ .**

(a)



(b)



(c)

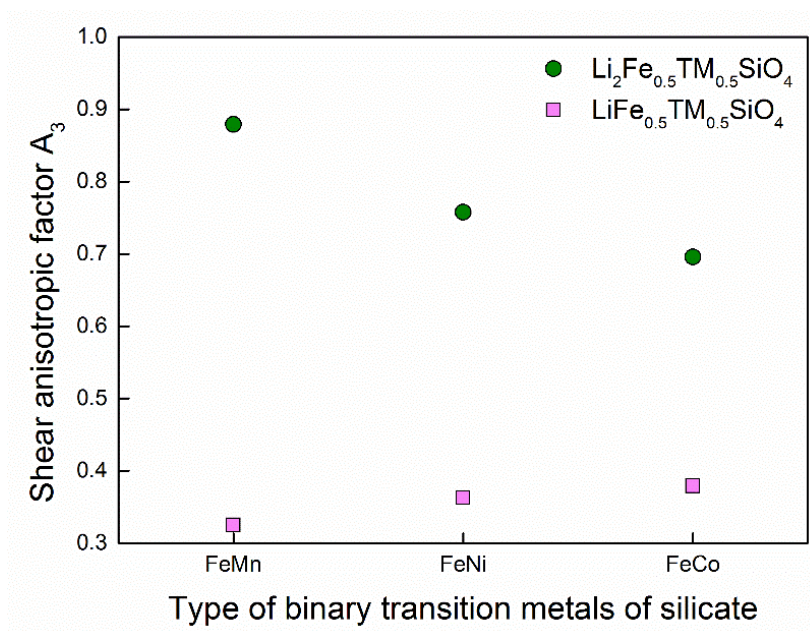
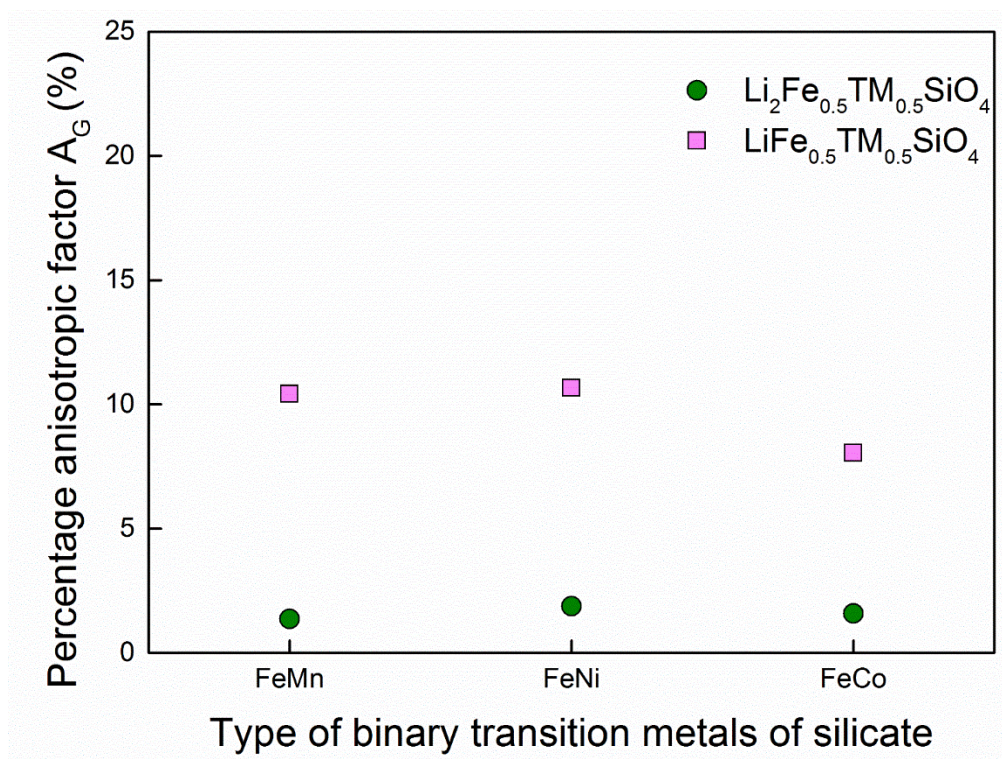


**Fig.2.3.8. Shear anisotropic factors (a)  $A_1$ , (b)  $A_2$  and (c)  $A_3$  of multicomponent silicates material  $\text{Li}_2\text{Fe}_{0.5}\text{TM}_{0.5}\text{SiO}_4$  and their semi-delithiated structures  $\text{LiFe}_{0.5}\text{TM}_{0.5}\text{SiO}_4$  (TM = Mn, Ni and Co), down label show the combination of transition metals  $\text{Li}_2\text{Fe}_{0.5}\text{Mn}_{0.5}\text{SiO}_4$  and  $\text{LiFe}_{0.5}\text{Mn}_{0.5}\text{SiO}_4$ ,  $\text{Li}_2\text{Fe}_{0.5}\text{Ni}_{0.5}\text{SiO}_4$  and  $\text{LiFe}_{0.5}\text{Ni}_{0.5}\text{SiO}_4$ , and  $\text{Li}_2\text{Fe}_{0.5}\text{Co}_{0.5}\text{SiO}_4$  and  $\text{LiFe}_{0.5}\text{Co}_{0.5}\text{SiO}_4$ . Green points are  $\text{Li}_2\text{Fe}_{0.5}\text{TM}_{0.5}\text{SiO}_4$  and pink points are  $\text{LiFe}_{0.5}\text{TM}_{0.5}\text{SiO}_4$ .**

(a)



(b)

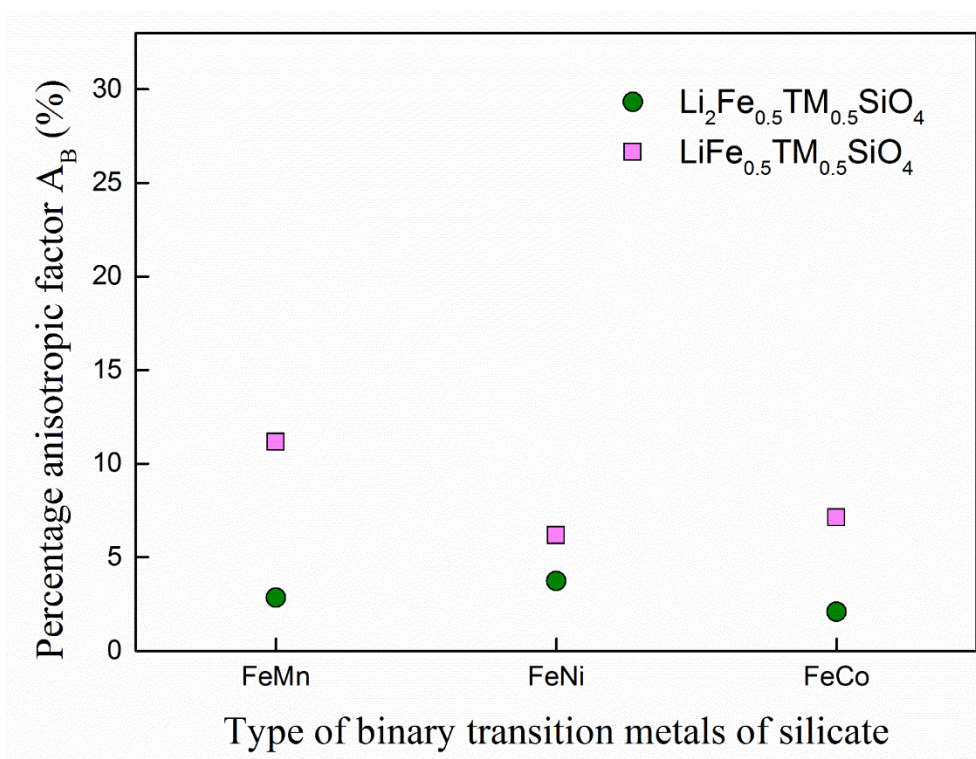


**Fig.2.3.9.** Shear percentage anisotropic factor (a)  $A_G$  and bulk percentage anisotropic factor (b)  $A_B$  of multicomponent silicates material  $\text{Li}_2\text{Fe}_{0.5}\text{TM}_{0.5}\text{SiO}_4$  and their semi-delithiated structures  $\text{LiFe}_{0.5}\text{TM}_{0.5}\text{SiO}_4$  (TM = Mn, Ni and Co), down label show the combination of transition metals  $\text{Li}_2\text{Fe}_{0.5}\text{Mn}_{0.5}\text{SiO}_4$  and  $\text{LiFe}_{0.5}\text{Mn}_{0.5}\text{SiO}_4$ ,  $\text{Li}_2\text{Fe}_{0.5}\text{Ni}_{0.5}\text{SiO}_4$  and  $\text{LiFe}_{0.5}\text{Ni}_{0.5}\text{SiO}_4$ , and  $\text{Li}_2\text{Fe}_{0.5}\text{Co}_{0.5}\text{SiO}_4$  and  $\text{LiFe}_{0.5}\text{Co}_{0.5}\text{SiO}_4$ . Green points are  $\text{Li}_2\text{Fe}_{0.5}\text{TM}_{0.5}\text{SiO}_4$  and pink points are  $\text{LiFe}_{0.5}\text{TM}_{0.5}\text{SiO}_4$ .

**Table.2.2.1. Elastic constants (given in GPa) of  $\text{Li}_2\text{TMSiO}_4$  and  $\text{LiTMSiO}_4$  (TM = Fe and Mn).**

Type of TM	$\text{Li}_x\text{FeSiO}_4$		$\text{Li}_x\text{MnSiO}_4$	
	2	1	2	1
<b>c11</b>	202.3	201.8	191.2	262.9
<b>c22</b>	130.3	85.1	130.9	77.3
<b>c33</b>	141.2	100.9	149.6	54.3
<b>c44</b>	34.8	16.9	36.3	7.2
<b>c55</b>	43.2	34.5	44.1	35.0
<b>c66</b>	40.1	20.0	44.2	19.9
<b>c12</b>	66.3	43.2	70.9	38.7
<b>c13</b>	63.4	32.3	66.7	39.4
<b>c23</b>	45.7	26.3	42.2	22.3

**Table.2.2.2. Elastic constants (given in GPa) of  $\text{Li}_2\text{TMSiO}_4$  and  $\text{LiTMSiO}_4$  (TM = Ni and Co).**

Type of TM	$\text{Li}_x\text{NiSiO}_4$		$\text{Li}_x\text{CoSiO}_4$	
	2	1	2	1
<b>c11</b>	208.6	179.5	188.5	203.6
<b>c22</b>	133.2	79.6	136.7	83.4
<b>c33</b>	137.2	88.8	151.2	91.8
<b>c44</b>	38.1	22.2	39.5	15.1
<b>c55</b>	40.3	27.8	41.9	29.9
<b>c66</b>	39.2	18.6	38.6	16.6
<b>c12</b>	65.5	42.1	65.6	38.7
<b>c13</b>	64.0	25.2	58.4	29.6
<b>c23</b>	39.8	22.4	45.6	24.9

**Table.2.3.1. Elastic constants (given in GPa) of  $\text{Li}_2\text{Fe}_{0.5}\text{TM}_{0.5}\text{SiO}_4$  and  $\text{LiFe}_{0.5}\text{TM}_{0.5}\text{SiO}_4$  (TM = Mn, Ni and Co).**

Type of TM	$\text{Li}_x\text{FeMnSiO}_4$		$\text{Li}_x\text{FeNiSiO}_4$		$\text{Li}_x\text{FeCoSiO}_4$	
	2	1	2	1	2	1
<b>c11</b>	200.3	228.2	212.7	188.3	199.7	202.3
<b>c22</b>	132.9	81.6	130.0	84.3	133.8	85.4
<b>c33</b>	145.5	85.6	141.1	96.7	143.9	98.0
<b>c44</b>	35.4	42.3	35.9	56.4	36.9	47.8
<b>c55</b>	44.0	32.8	43.1	29.6	42.5	31.5
<b>c66</b>	42.2	18.6	40.0	17.7	39.6	20.7
<b>c12</b>	70.6	40.6	65.8	38.7	52.9	34.9
<b>c13</b>	66.4	34.0	63.8	30.6	64.0	38.6
<b>c23</b>	45.3	24.6	41.7	26.1	45.7	27.7

### 3. Novel design and study of poly-oxyanion $\text{LiFeP}_{1-x}\text{Si}_x\text{O}_4$

#### 3.1. Overview of phosphate and silicate materials

In recent times, poly-oxyanion compounds have emerged as promising cathode materials of LIBs, and poly-oxyanion compounds mean that have not only metal and oxygen but also anion complexes. The olivine crystal structure  $\text{LiMPO}_4$  (M=Fe, Mn, Co Ni and so on) forms an important class of cathodes of Li rechargeable battery cathodes. In particular,  $\text{LiFePO}_4$  (LFP) has received much attention as a promising cathode material for LIBs, since the discovery of the Padhi et al., for its higher reversible capacity ( $\sim 170\text{mAhg}^{-1}$ ), environment friendly characteristics, high thermal stability, cycle life, and lower cost as compared to commercially used cathode materials like  $\text{LiCoO}_2$  (LCO).<sup>11-12</sup> However, it has major limitations of poor ionic and electronic conductivity, in addition to lower energy density and intercalation voltage ( $\sim 3.5\text{V}$ ).<sup>59</sup> Moreover, it has poor Li ion diffusivity due to only one dimensional lithium ion diffusion channel, unlike  $\text{LiCoO}_2$  and  $\text{LiMn}_2\text{O}_4$  which has two-dimensional and three-dimensional Li ion diffusion channels, respectively. Nevertheless recent works overcome the limitations of LFP, and one of main breakthroughs is carbon coating, and development of the carbon coating enhances the low electronic conductivity of LFP. However other disadvantages of the LFP interrupt the use of cathode of LIBs is limited in commercial electronic devices.

Meanwhile, Goodenough et al. suggested orthosilicate  $\text{Li}_2\text{MSiO}_4$  (M=Fe, Mn, Co, Ni

and so on) as a cathode material of LIBs. This material has generated great interest as it has a theoretical capacity of 330mAhg<sup>-1</sup> due to its characteristic of reversible extraction/insertion of two lithium ions. In particular, Li<sub>2</sub>FeSiO<sub>4</sub> (LFS) has the advantages of low cost, nontoxicity, and environment friendly features due to the presence of the transition metal Fe.<sup>34, 56</sup> However, it has poor electronic conductivity and shows phase transformation after the extraction of one lithium ion or excess its, and hence, it does not exhibit the predicted theoretical capacity. Therefore, many researchers are interested in developing poly-oxyanion compounds to overcome the aforementioned disadvantages for gainful use as electrodes in commercial LIBs.<sup>28</sup>

Recently, multicomponent poly-oxyanion cathode materials that include multiple transition metals in pristine structures, such as olivine or tetrahedral structures, were investigated. These cathode materials have different kinetic and electrochemical properties as compared to poly-oxyanion cathode materials that have only one type of transition metal. Poly-oxyanion compounds have different physical and electrochemical properties not only due to the number of transition metals but also the number of anions. Many scientists have studied poly-oxyanion compounds possessing other anion atoms, or pristine cathode materials doped with different anion atoms.<sup>60-64</sup> The inductive effect of different oxyanion groups (XO<sub>4</sub><sup>n-</sup>, X=P, Si and so on) yields different X Mulliken-electronegativity. The inductive effect signifies the polarization of the M-O bond according to that of the X-O bond and thus, the X electronegativity determines the polarization of both X-O and M-O bond, as well as the ionic covalent feature of the M-O bond of the poly-oxyanion compound.

In addition, the intercalation voltages and other electrochemical properties of the compound to be used as a cathode material of LIBs, are also shown. Si has the lowest electronegativity ( $\sim 1.90$ ), and therefore, has strong Si-O bonds and better lattice stabilization as compared to other X-O bonds.

### 3.2. Theoretical design of $\text{LiFeP}_{1-x}\text{Si}_x\text{O}_4$

Computational methods: The ab initio calculations were based on the DFT method as implemented in the VASP code. A generalized gradient approximation (GGA) was used with the Perdew-Burke-Ernzerhof (PBE) functional of the exchange and correlation energy.<sup>48</sup> For calculation, a projector augmented wave (PAW) method was selected to describe the interactions between the ion core and valence electrons. For accurate interactions inside the d-orbitals of the transition metal, we used GGA+U scheme. Within GGA+U scheme, effective Hubbard  $U$   $U_{\text{eff}} = U - J$ , was used for Fe (4.3 eV) in the overall calculation. There was a difference of only a few milli-electron volts by using the GGA+U method. We used an energy cutoff for the plane wave basis set was 600 eV and the k-point mesh in the Monkhorst pack scheme was set to  $4 \times 4 \times 4$ . The atomic coordinates and cell parameters were fully relaxed in order to optimize the crystal structures. The lithium ionic conductivity and lithium migration energy were calculated by using the climbing-image nudged elastic band (NEB) method for the LFPS structures.<sup>65</sup>

In this study, the crystal structure of the polyoxyanion compound, when P and Si anions

are mixed, is to be determined. As the structure of the synthesized phosphor-silicate is not known, all the possible structures must be considered, which are shown Fig.2.2.1.

Next the initial approach is to carry out the calculation for complete optimization of the olivine structure of  $\text{LiFePO}_4$  based on DFT studies. The olivine structure of  $\text{LiFePO}_4$  is orthorhombic of the space group  $Pnma$ , with a few distorted hexagonal close packed oxygen arrays. The Li and Fe ions are located at the octahedral sites at the edge and corner sharing, while the P atoms occupy the tetrahedral sites. At these sites, the P ions were replaced by Si ions at the same positions, and the structure was fully relaxed by using ab-initio calculations.

Next, the structural optimization of all the  $\text{Li}_2\text{FeSiO}_4$  structures was carried out through DFT calculations. The silicate  $\text{Li}_2\text{FeSiO}_4$  is tetrahedral in structure and exhibits polymorphism, viz. of the space groups  $Pmn2_1$ ,  $P2_1/n$  and  $Pmnb$ , of which  $Pmn2_1$  and  $Pmnb$  are orthorhombic whereas  $P2_1/n$  is monoclinic in structure. Therefore, all the crystal structures must be determined, and by experimental observation, the modeling of pristine silicates  $\text{Li}_2\text{FeSiO}_4$  was first established and then the substitution of Si by P was carried out. However, the phosphor-silicate structure cannot be optimized as the numbering of Li ions do not match with those in the olivine structure. Phase transformation of silicate  $\text{Li}_2\text{FeSiO}_4$  occur when more than 1 mol Li ions are extracted, hence, only 1 mol Li ion was extracted from all the polymorphism structures of  $\text{Li}_2\text{FeSiO}_4$  to develop the same chemical equation as for the olivine structure. The formation energies of the olivine and tetrahedral structures with the mixed P and Si were determined on the basis of first principles study by using

Equation 1 given below:

$$\text{Formation energy}_{\text{LiFeSi}_{1-x}\text{P}_x\text{O}_4} = E_{\text{LiFeSi}_{1-x}\text{P}_x\text{O}_4} - [(1-x)E_{\text{LiFeSiO}_4} + xE_{\text{LiFePO}_4}] \quad (3.2.1)$$

where E is the total energy of the material sub-text and x is the number of silicon atoms that have been added per formula unit.

The formation energies determined by the computational studies are shown in Fig.3.1. As can be seen from the figure, the formation energies of the phosphor-silicate have the lowest value for the entire range of silicon ratios. This means that the most optimized structure is the olivine structure, and if phosphorus and silicon are mixed in the poly-oxyanion compound experimentally, the synthesized olivine structure is obtained. Among the tetrahedral structures, the most optimized structure was that of  $P2_1/n$  when the Si ratio was altered from 0 to 0.18. However, for the Si ratio from 0.18 to 0.35, the space group  $Pmn2_1$  structure was the most optimized, and when the Si ratio was more than 0.35, the space group  $Pmnb$  structure was the most optimized structure until the final crystal structure  $\text{LiFeSiO}_4$ . Therefore, besides the olivine structure, the most optimized of the tetrahedral structures was different, depending on the proportion of P and Si. Thermodynamically, the olivine structure is the most optimized structure for mixed phosphorus and silicon; hence, this structure was selected and detailed computational studies were simulate. Fig. 2b shows formation energies of all the possible structures for the substitution of P by Si using DFT calculation. And the entire schemes of thermodynamically ground state structures of olivine  $\text{LiFe}_{1-x}\text{Si}_x\text{O}_4$  ( $x = 0 \sim 1$ ) given in Fig.3.2. It is known that silicon ions cannot intercalate all the phosphorus positions as some formation energies are positive.

However, the calculation has to be mentioned as mixing of P and Si at other sites or other structures in real experiments be sure to occur due to non-ideal and non-equilibrium states involved during synthesis hence DFT calculations very important for show the optimized structure in this study.

### 3.3. Improved the performance of $\text{LiFeP}_{1-x}\text{Si}_x\text{O}_4$

In Fig.3.3, the structural parameters, viz., the lattice parameter and volume of the phosphor-silicate olivine structure are presented, which were calculated by using both the GGA and GGA+U potentials. The values as determined with the GGA potential are more accurate. Therefore, only these are shown in Fig.3.3 and there is good agreement with the values determined in previous works. The lattice parameters a, b, and c decrease almost linearly, but the difference is negligibly small.

The volume shows the same tendency as the lattice parameters. In addition, as shown in Fig. 3.2, there is almost no distortion of the entire structures. This signifies that lattice and angle distortion is negligible, and thus, the structure does not collapse on substitution of P by Si. As the electrochemical performance of the batteries is not degraded, there is a spacing advantage such as energy densities. The effect of increase in the concentration of Si doping on the bonding distance between Li, Fe, P and Si and O is shown in Fig.3.4.<sup>66</sup> Several kinetic characteristics of the LIBs are illustrated by a study of the bonding distance.

The bonding distance between phosphorus and silicon and oxygen is shown in Fig.3.4a

and Fig.3.4b. It can be seen that it remains almost the same even though the silicon ratio is increased. This means that the bonding anion with oxygen is very strong; and this provides the stability of the structure. And these anions are cannot performed charge carrier when progress charge and discharge of LIBs.<sup>67</sup>

The bonding distance between lithium and iron and oxygen in shown in Fig.3.4c and Fig.3.4d. It can be seen that the bonding length between Fe and O decreases with increasing silicon ratio which means that the bonding is strong. In the orthorhombic olivine structure  $\text{LiFePO}_4$ , an anti-site defect occurs when there is a lithium vacancy following the extraction of lithium (discharging process). An anti-site defect is that when the iron ion moves from its original position, a lithium vacancy occurs, but the critical defect hinders the lithium ion mobility because the lithium ion path is only a one-dimensional path in olivine structure. However, in the phosphor-silicate, the anti-site defect is diminished as the Fe-O bonding is strong, and the mobility of the iron is decreased even if a lithium vacancy occurs. And these illustrations of bonding length between Li and O demonstrate that the ionic conductivity of iron phosphor-silicate is better as compared to that of pristine  $\text{LiFePO}_4$ . Moreover, the bonding length between Li and O increase when the silicon ratio is increased, i.e., the Li mobility becomes better kinetically. Hence, the ionic conductivity of the phosphor-silicate improves with increase in the silicon ions instead of phosphorus.

For a detailed study of the lithium ionic conductivity, lithium migration energy barriers of the pristine phosphor-silicates were calculated by using the NEB method and the schematics of migration path is shown in Fig.3.5<sup>61</sup> and the result is shown in Fig.3.6.<sup>68-69</sup> It

is so difficult for show the lithium migration energy barrier depend on amount of lithium concentration in real time because electrode material generates phase separation or transition during charge/discharge process and this process is dynamic one while DFT study is static calculation. Hence many previous studies confirmed lithium migration energy barrier on certain single phased crystal structure.<sup>62</sup>

The higher the lithium migration energy barrier, the more difficult it is for the lithium ion to move along the migration path. And the lithium migration energy overs 1 eV, lithium ion almost cannot pass the decided path for NEB method. For accuracy of calculation, all the structures were fully relaxed; and the lithium ion was moved. It is known from previous studies, that lithium migrates only in a one- dimensional path along the (010) direction and describes a curved trajectory between adjacent Li sites; hence, the migration energy barriers in the (010) direction were calculated in two steps.<sup>62</sup> The lithium migration energy barrier for  $\text{LiFePO}_4$ ,  $\text{LiFeP}_{0.5}\text{Si}_{0.5}\text{O}_4$  and  $\text{LiFeSiO}_4$  was calculated for the two paths to investigate its variation with the silicon ratio. For pristine phosphate  $\text{LiFePO}_4$ , the value of the migration energy barrier was 0.180 eV for the first as well as the second path, and these results are in good agreement with the previous calculation.<sup>70-72</sup> For  $\text{LiFeP}_{0.5}\text{Si}_{0.5}\text{O}_4$ , the energy barrier for the first path was 0.250 eV and that for the second path was 0.240 eV. Finally, the energy barrier or both the first and second path was 0.280 eV for  $\text{LiFeSiO}_4$ . It can be observed that the lithium migration barrier is higher for a greater silicon ratio, or, the Li ionic diffusivity deteriorates thermodynamically for increased silicon ratio. This is contrary to the result indicated in relation to the bonding distance between lithium and

oxygen for increased Si ratio. Therefore, it is inferred that a strong Si-O bond has a greater influence than kinetically large Li-O bonding length. However, the values do not increase significantly enough to hinder the lithium ionic diffusivity ( $< 0.3$  eV); hence, the lithium ionic conductivity shows little change even if the Si ratio increases. Using first principles study, a Bader charge analysis was conducted and the net charge with increase in the Si ratio is shown in Fig.3.7. The parameters for phosphorus, silicon and lithium are not shown as they maintain values of zero or one. The important points are Bader charges of iron and oxygen and it can be seen from the figure that the net charge of iron decreases whereas that of oxygen increases with an increase in the silicon ratio. Research work based on DFT calculations gives an accurate estimation of the Li intercalation voltage for crystal structures of several cathode materials and many previous DFT calculation studies show confirm the estimation and compared with experiment results. The equation for calculating the theoretical voltage is given below.

$$V_{LiFeP_{1-x}Si_xO_4} = \frac{G_{Li_{y_2}FeP_{1-x}Si_xO_4} - G_{Li_{y_1}FeP_{1-x}Si_xO_4} + (y_2 - y_1)G_{Li}}{y_2 - y_1} \quad (3.3.1)$$

In poly-oxyanion cathodes like  $LiFeXO_4$  and  $Li_2FeXO_4$  (X may be P or Si), octahedral  $FeO_6$  and tetrahedral  $XO_4$  form linkages of the Fe-O-X-O-Fe type, and the strength of the X-O bonding has more influence than the Fe-O bonding on the intercalation voltage due to inductive effect.

According to previous reports, the lithium intercalation voltage of olivine  $LiFePO_4$  is 3.47 V, which corresponds to the result obtained in the present work. The intercalation

voltage of  $\text{LiFeSiO}_4$  increases to 4.97 V showing that substitution of P by Si effected significant improvement due to stronger Si-O bonding than that in pristine phosphates. This shows that the newly type of cathode material has a higher intercalation voltage than the original iron phosphate  $\text{LiFePO}_4$  and it can be controlled by the proportion of Si. As shown in Fig. 3.8a, the intercalation voltage gradually increases with the proportion of Si and the intercalation voltages of  $\text{LiFePO}_4$  and  $\text{LiFeSiO}_4$  obtained in this study compare well with the previous reports and experiment values. The voltage-capacity plot of the three structures viz.,  $\text{LiFePO}_4$ ,  $\text{LiFeP}_{0.5}\text{Si}_{0.5}\text{O}_4$  and  $\text{LiFeSiO}_4$ , is shown in Fig.3.8b to enable a direct comparison.

The phosphate olivine structure reacts in two phase reaction, and hence, it has only one intercalation voltage value.<sup>73</sup> All the structures have steady voltage values that are different but the capacity is the same because of the same Li content. The phosphor-silicate that has more proportion of silicon has more energy density. As can be seen in Fig.3.1a, the olivine crystal structure  $\text{LiFePO}_4$  in which P is substituted by Si is a thermodynamically stable structure.

Therefore, it is established that the cathode material  $\text{LiFeP}_{1-x}\text{Si}_x\text{O}_4$  has higher intercalation voltage than the original cathode material  $\text{LiFePO}_4$  although the capacity is the same and the voltage can be controlled by gradual substitution of P by Si, theoretically. The energy density of  $\text{LiFeP}_{1-x}\text{Si}_x\text{O}_4$  increases more than that of the original structure  $\text{LiFePO}_4$  as it is the product of voltage and capacity. These results are helpful at low energy density and voltage of  $\text{LiFePO}_4$  which is a major hurdle to its applications. Besides, the

volume of  $\text{LiFeP}_{1-x}\text{Si}_x\text{O}_4$  decreases and the voltage increases with gradual substitution of P by Si as shown in Fig.3.3 and Fig.3.8b. From Fig.3.9, it can be established that the volumetric energy density increases by 20% when half of the P is substituted by Si, and by 42% when all the P is substituted by Si.

In Fig.3.10, the total density of states (TDOS) for the pristine material  $\text{LiFePO}_4$  and that in which half of the P is substituted by Si viz.,  $\text{LiFeP}_{0.5}\text{Si}_{0.5}\text{O}_4$  are shown to facilitate a comparison of LFP with LFPS. The figures on the left are the TDOS for the lithiation structures, viz.,  $\text{LiFePO}_4$  and  $\text{LiFeP}_{1-x}\text{Si}_{1-x}\text{O}_4$ . The entire shape of the TDOS of the LFP and LFPS is similar as only Fe ions have a d-orbital and P and Si belong to the same group of the periodic table. However, the band gap, i.e., the gap between the lower Fermi level of the valence band and upper Fermi level of the conduction band, is narrower in LFPS (~1 eV) than in LFP (~4 eV). The results of the calculation in this study show that the electronic conductivity in LFPS is higher than in LFP because band gap can shows how better electronic conductivity of the electrode of LIBs. This is because in the polyoxyanion group, the inductive effect of the anion leads to a higher intercalation voltage than in other cathode materials, but simultaneously causes a lower electronic conductivity due to the isolated valence electrons of the transition metals. However, in LFPS, there are a lesser number of isolated valence electrons of the transition metal Fe as they have moved to the oxygen atoms due to the highly charge state of the Si-O polyhedral shape. The TDOS of the delithiation structures of LFP and LFPS are similar as all the Li ions are extracted, and the remaining ions are Fe, P and Si. The metal Fe ions have only free valence electrons, and P

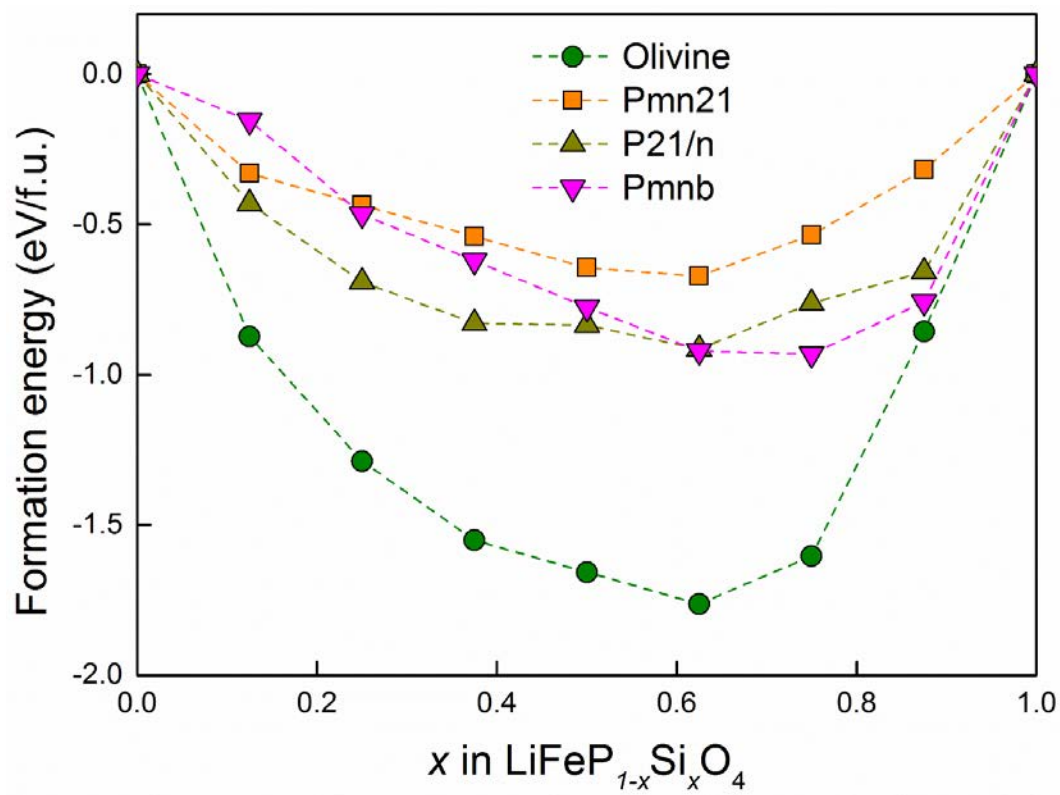
and Si have strong stability as can be seen from the Bader charge figures. Therefore, electrons can move more actively in LFPS hence, the electronic conductivity is better than in LFP.

### 3.4. Summary

In this study, the most optimized structure of poly-oxyanion cathode material with mixed P and Si was investigated by using DFT calculations from first principles. It was found that the most optimized structure was the olivine structure of the Pnma space group for all the mixed P and Si cases thermodynamically, and the new design structure was named LFPS ( $\text{LiFeP}_{1-x}\text{Si}_x\text{O}_4$ ,  $x=0\sim 1$ ). There is no distortion the structure as regards the lattice parameters and volume. The Fe-O bonding length becomes shorter when P is substituted by Si which means that the Fe-O bonding is stronger in the LFPS structure thus preventing the anti-site defect in a delithiated LFPS structure. The Li-O bonding length and lithium migration barrier were studied to examine the lithium ionic conductivity. The Li-O bonding length becomes longer linearly when P is substituted by Si whereas the calculated lithium migration energy barriers of the olivine LFPS and LFS ( $\text{LiFeP}_{0.5}\text{Si}_{0.5}\text{O}_4$  and  $\text{LiFeSiO}_4$ ) structures show higher values as compared to that of the pristine LFP ( $\text{LiFePO}_4$ ) structure, due to an increased Si ratio. Hence, it is predicted that the ionic conductivity of the pristine LFP is better than that of LFPS, but the increased values of the migration energy barriers of the olivine LFPS and LFS viz., 0.180 eV and 0.245 eV, respectively, are very

close to the values of the pristine LFP (0.280 eV), and thus sufficient for use as a cathode material or Li-ion batteries ( $< 0.3$  eV). In addition, the intercalation voltage of that LFPS structure increases ( $\sim 4.97$  eV) and the energy density also increases ( $\sim 42\%$ ) when P is substituted by Si continuously. An investigation of the TDOS and band gap shows that the electronic conductivity of LFPS is better than that of LFP. The present study suggests the development of a promising candidate for the cathode material of LIBs with a new method of improving its performance. For further investigations, the results will be validated by experiments and a deeper study will be conducted by using first principles study.

(a)



(b)

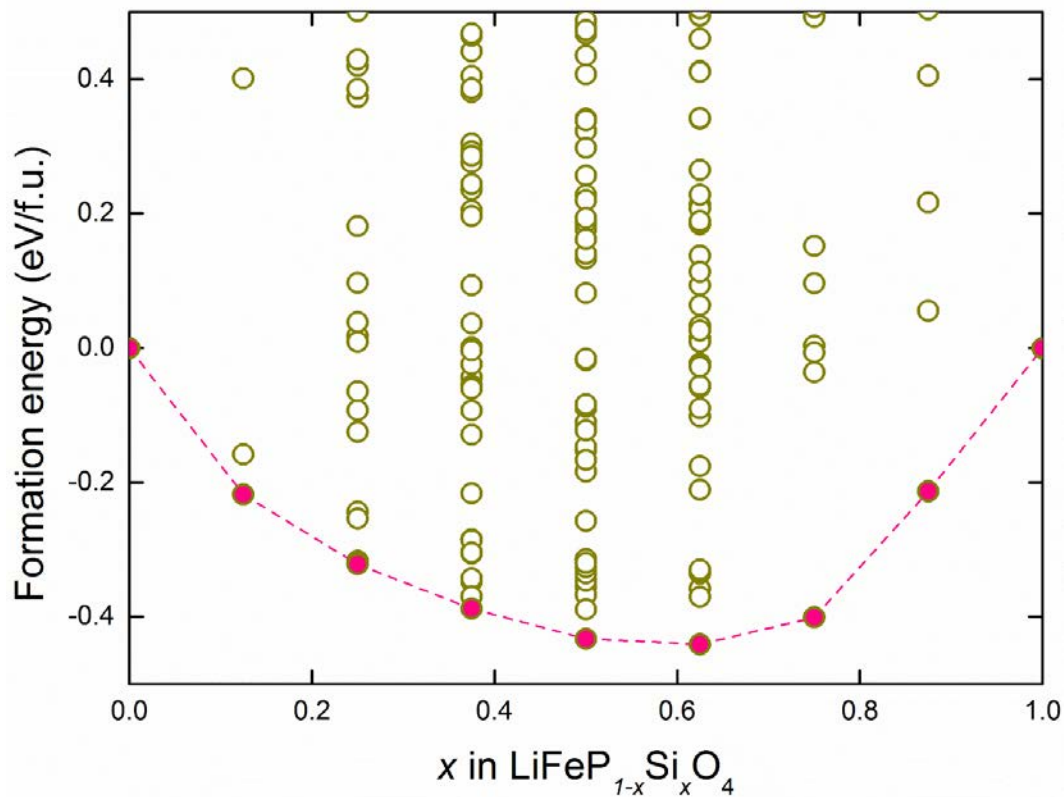
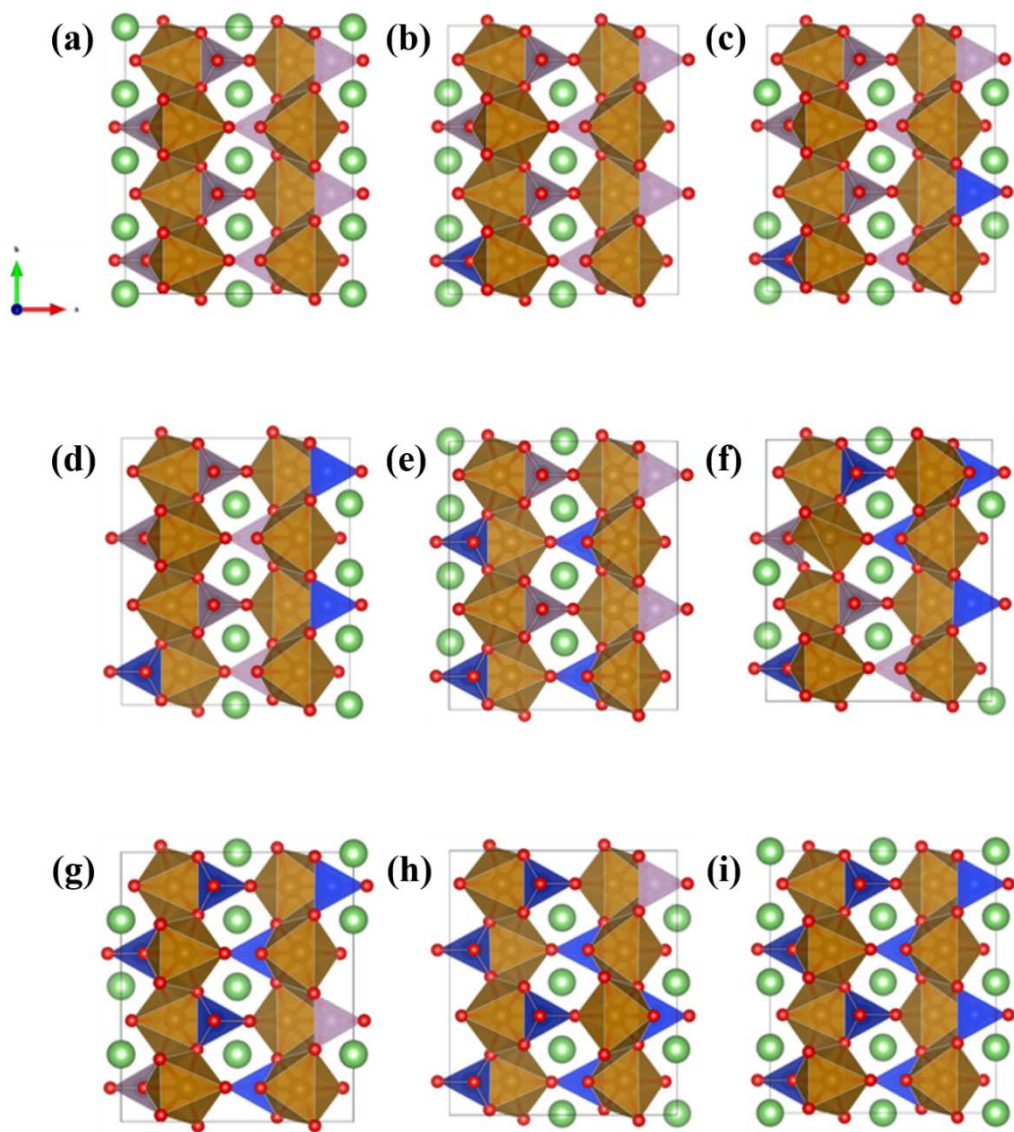
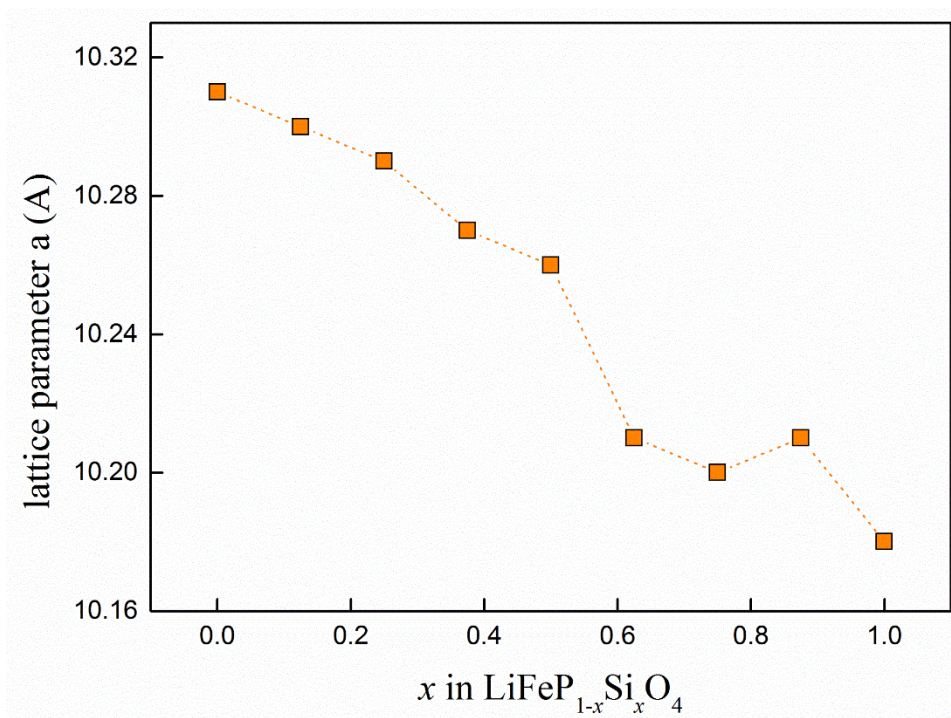


Fig.3.1. (a) Formation energies of the most optimized olivine and tetrahedral structures for mixed phosphorus and silicon. Chemical equation is  $\text{LiFeP}_{1-x}\text{Si}_x\text{O}_4$ . (b) Formation energies of all possible structure at only olivine crystal structure. Pink points mean that most optimized structures thermodynamically.

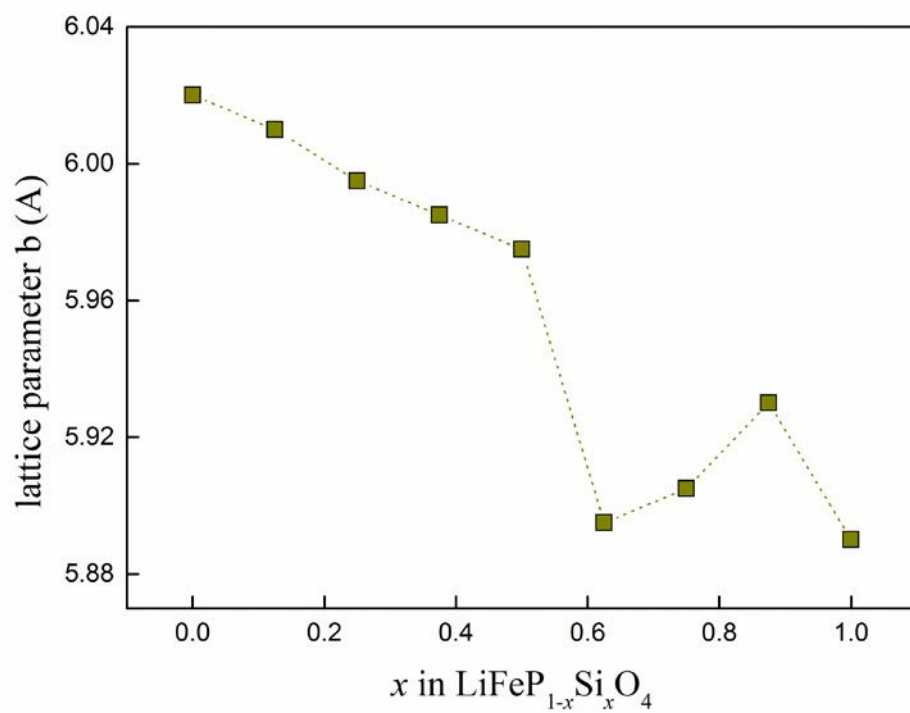


**Fig.3.2.** Ground state structures of olivine  $\text{LiFeP}_{1-x}\text{Si}_x\text{O}_4$  (a)  $x = 0$  (b)  $x = 0.125$  (c)  $x = 0.250$  (d)  $x = 0.375$  (e)  $x = 0.5$  (f)  $x = 0.625$  (g)  $x = 0.75$  (h)  $x = 0.875$  (i)  $x = 1$ . Green color represents Li atoms; blue, Si; gray, P; brown Fe.

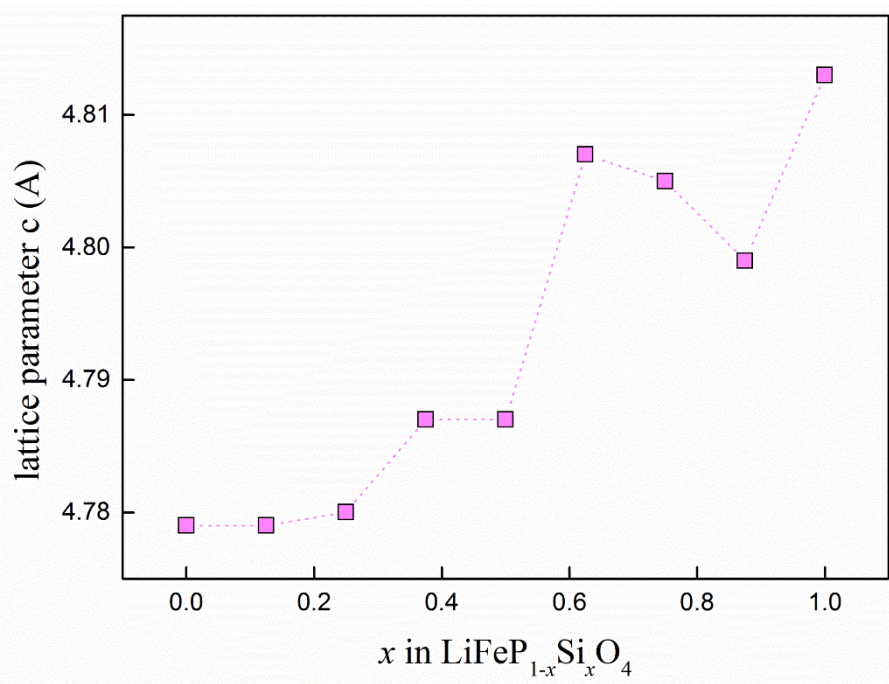
(a)



(b)



(c)



(d)

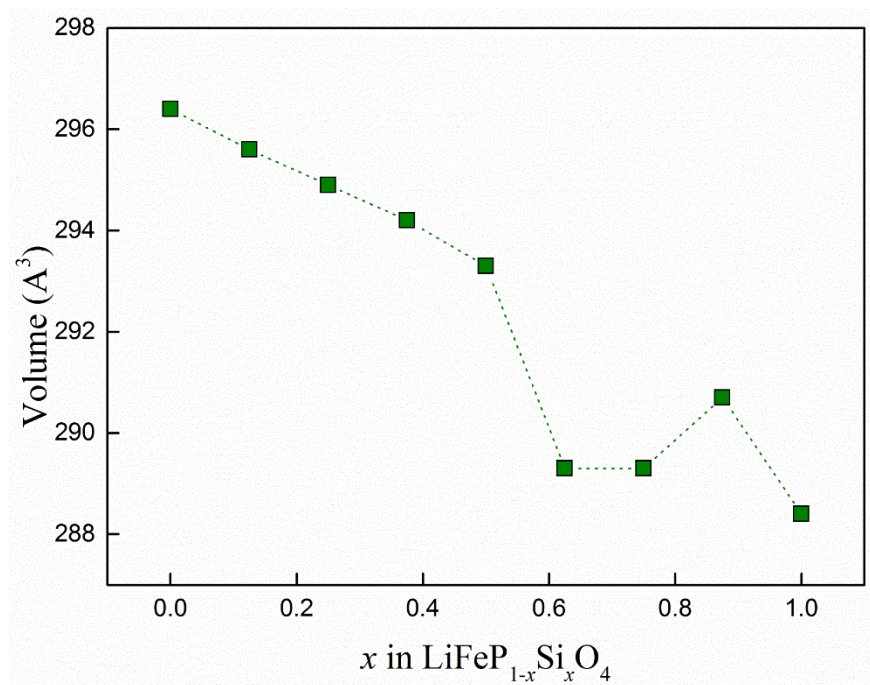
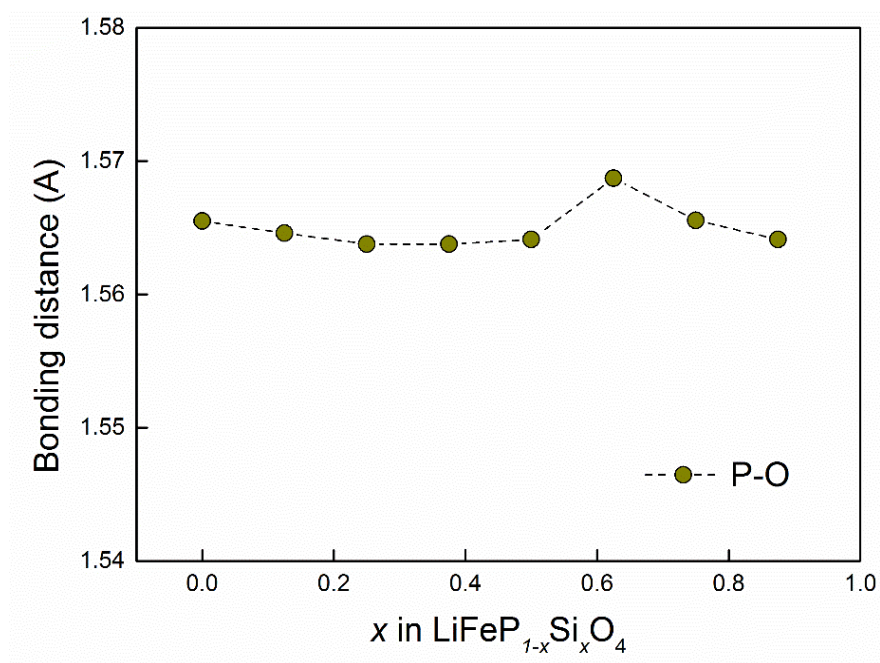
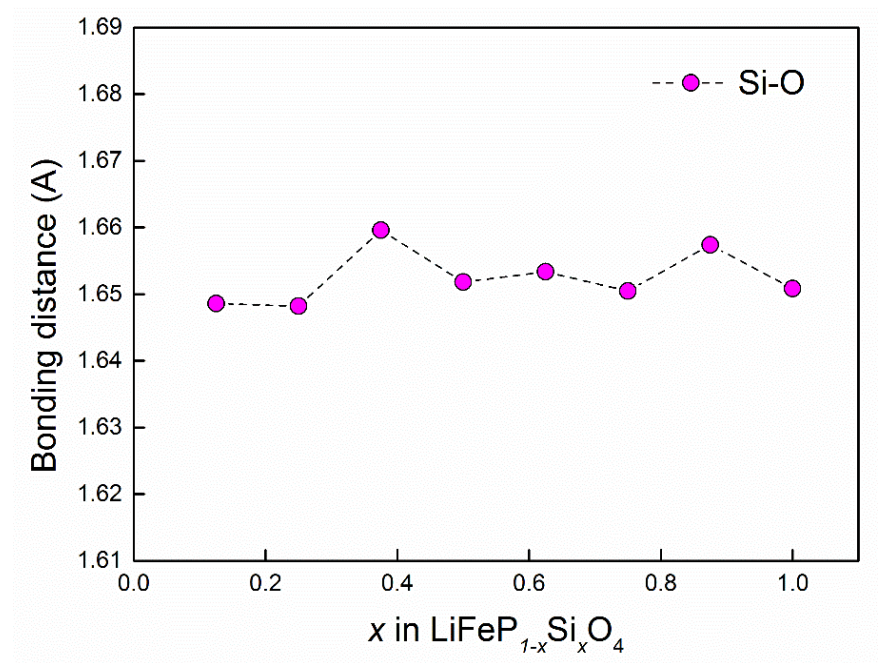


**Fig.3.3.** Lattice parameters (a) a, (b) b, and (c) c (Å) and (d) volume (Å<sup>3</sup>) per formula unit (f.u.) for olivine structures LiFeP<sub>1-x</sub>Si<sub>x</sub>O<sub>4</sub> that was the most optimized structure thermodynamically.

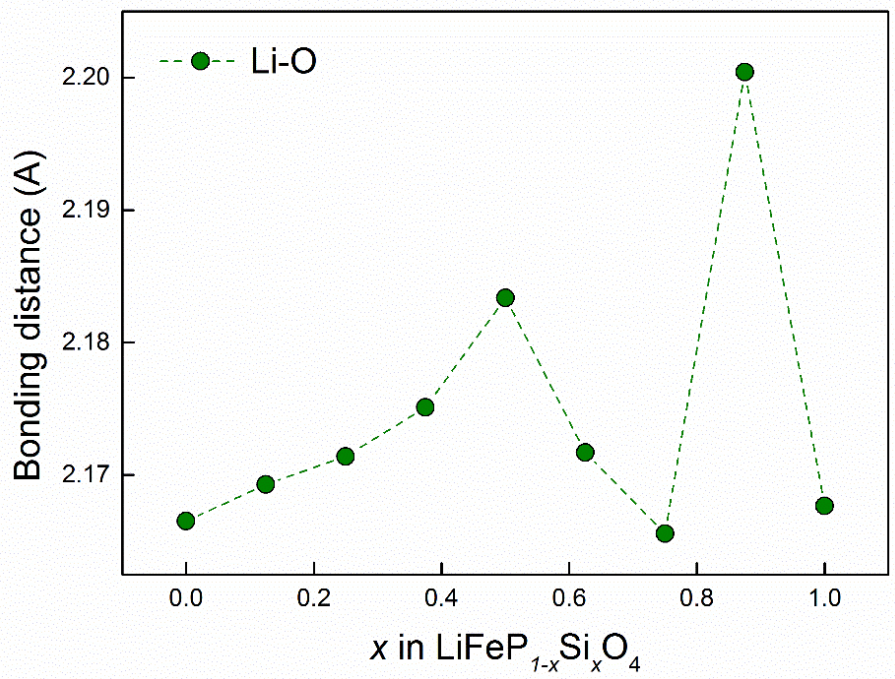
(a)



(b)



(c)



(d)

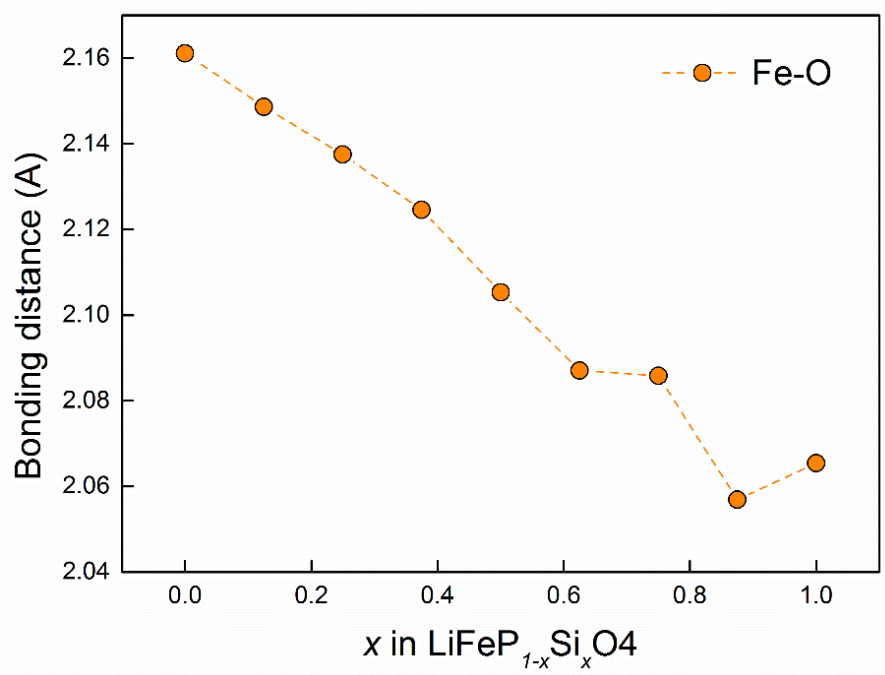


**Fig.3.4. Bonding distance of most optimized olivine structure. Bonding distance between (a) P and O. (b) Si and O (c) Li and O and (d) Fe and O.**

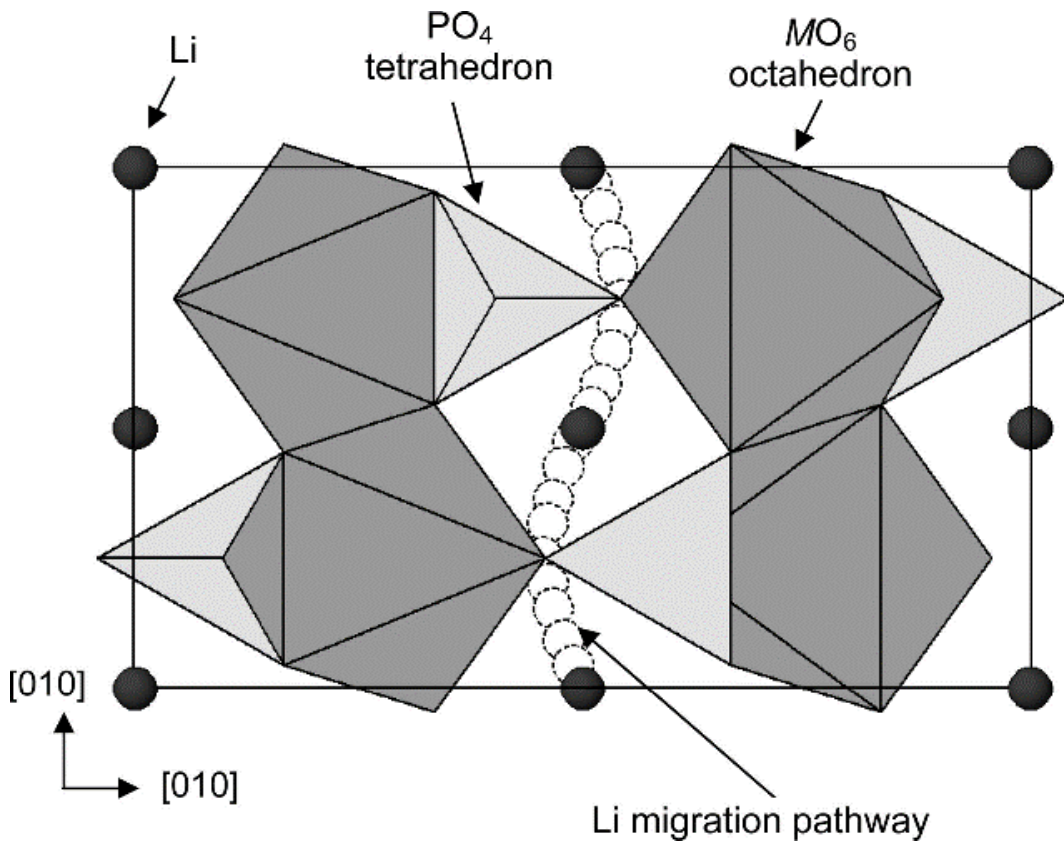


**Fig.3.5. Li migration path of olivine crystal structure. The diffusion path direction is only 1D  $(010)$  direction.<sup>61</sup>**

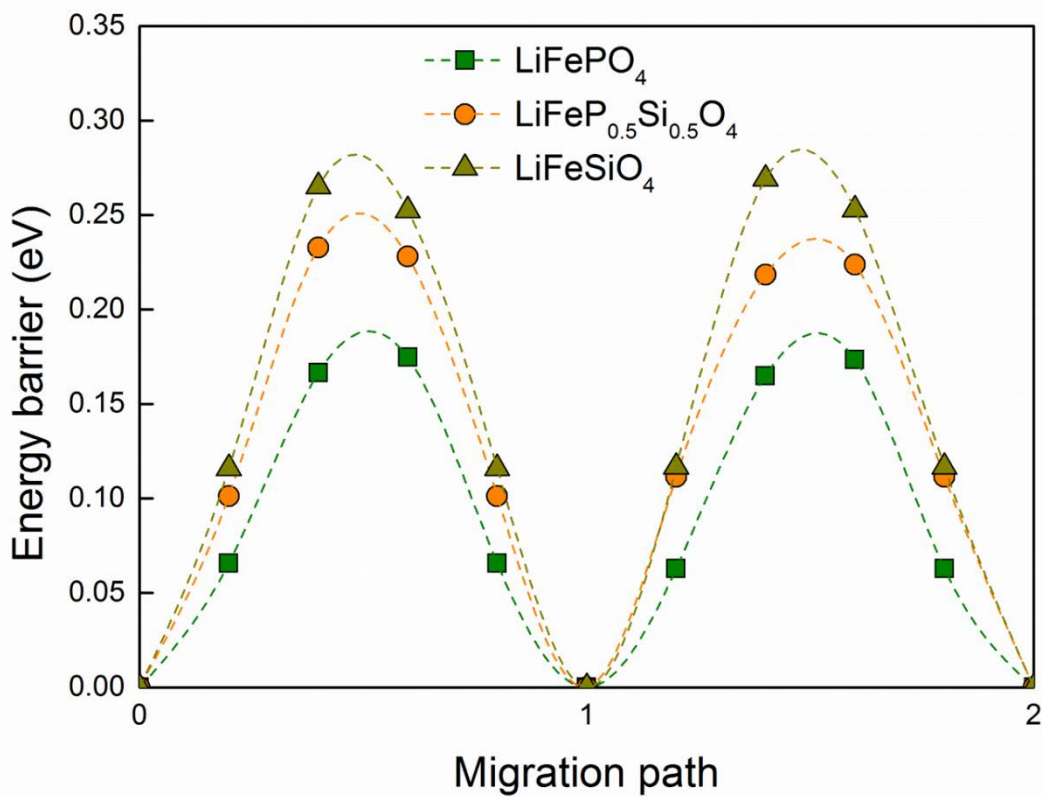
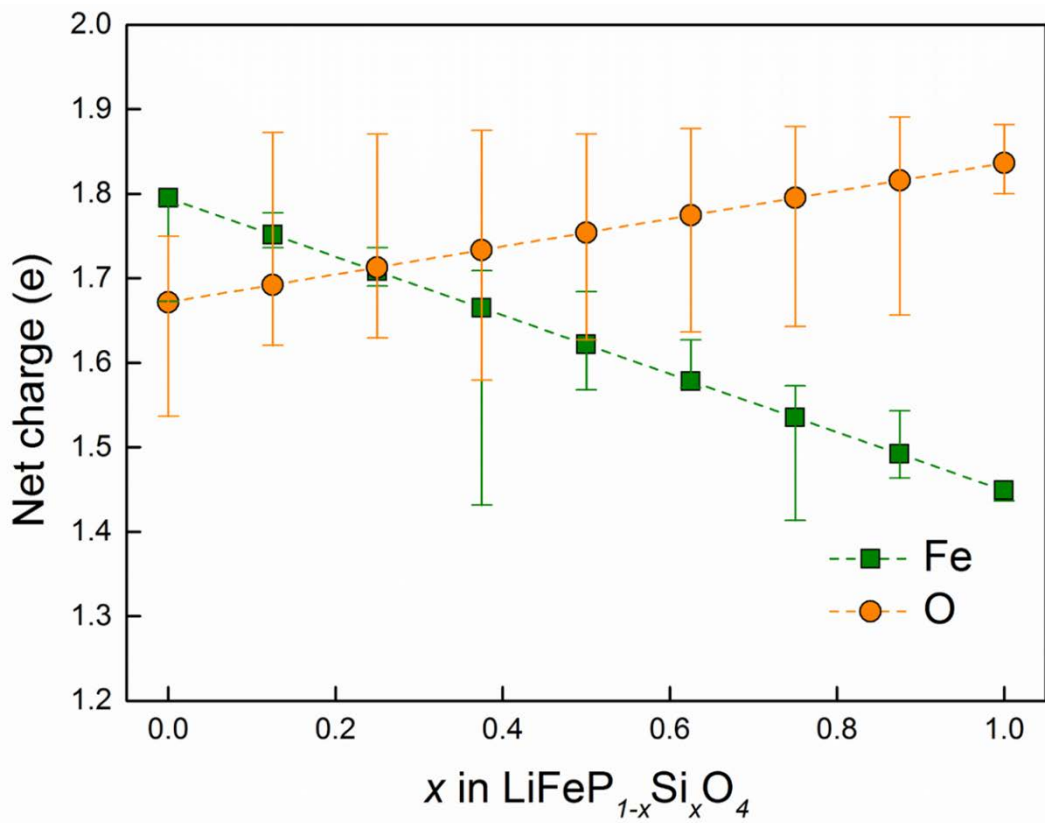
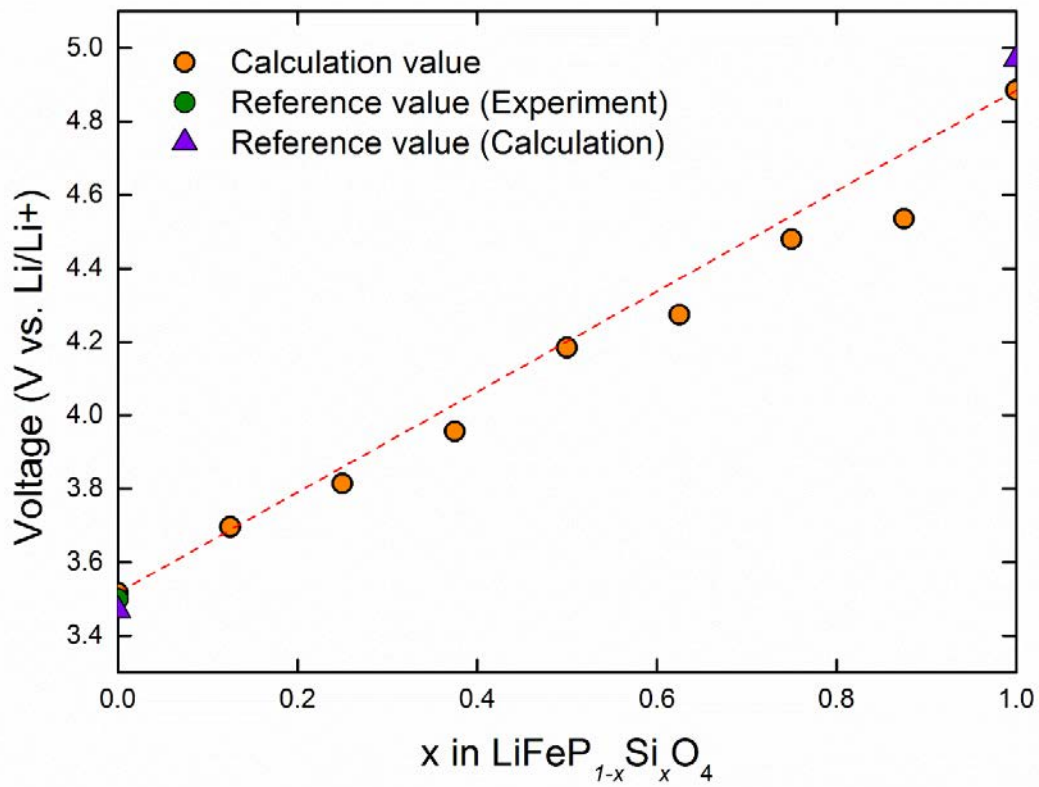


Fig.3.6. Calculated lithium migration energy barriers along the (010) path of LiFePO<sub>4</sub>, LiFeP<sub>0.5</sub>Si<sub>0.5</sub>O<sub>4</sub> and LiFeSiO<sub>4</sub>.



**Fig.3.7. Bader charge of Fe & O of iron phosphor-silicate for olivine structure  $\text{LiFeP}_x\text{Si}_{1-x}\text{O}_4$  with increase in P ratio.**

(a)



(b)

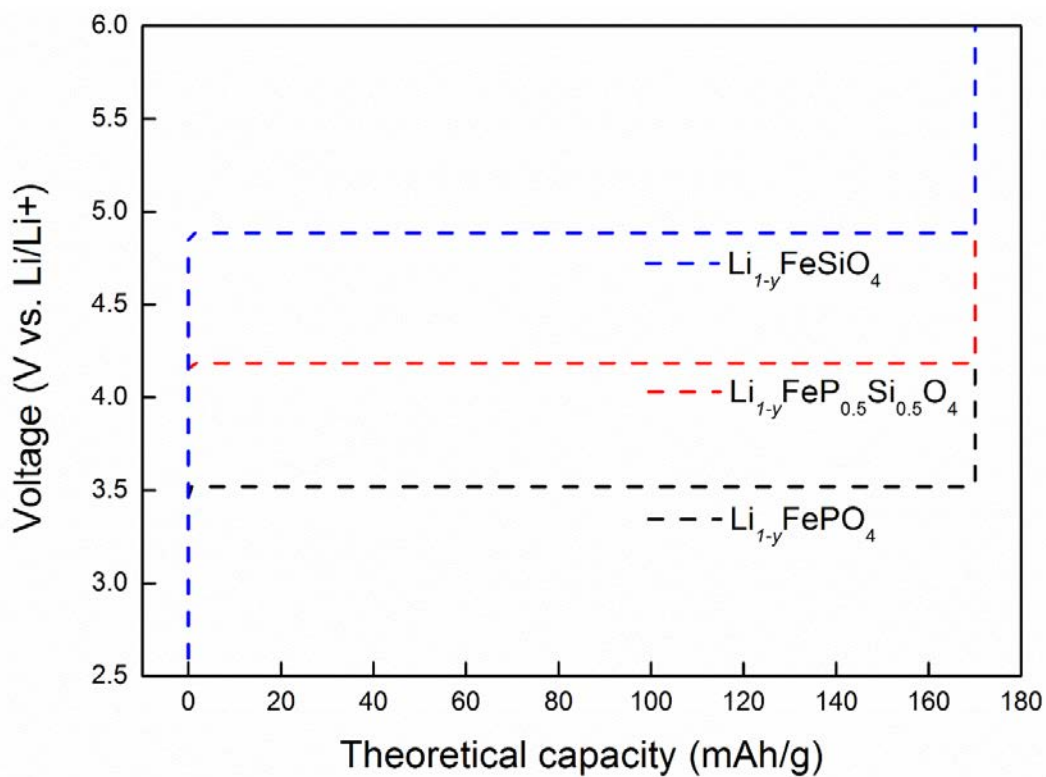
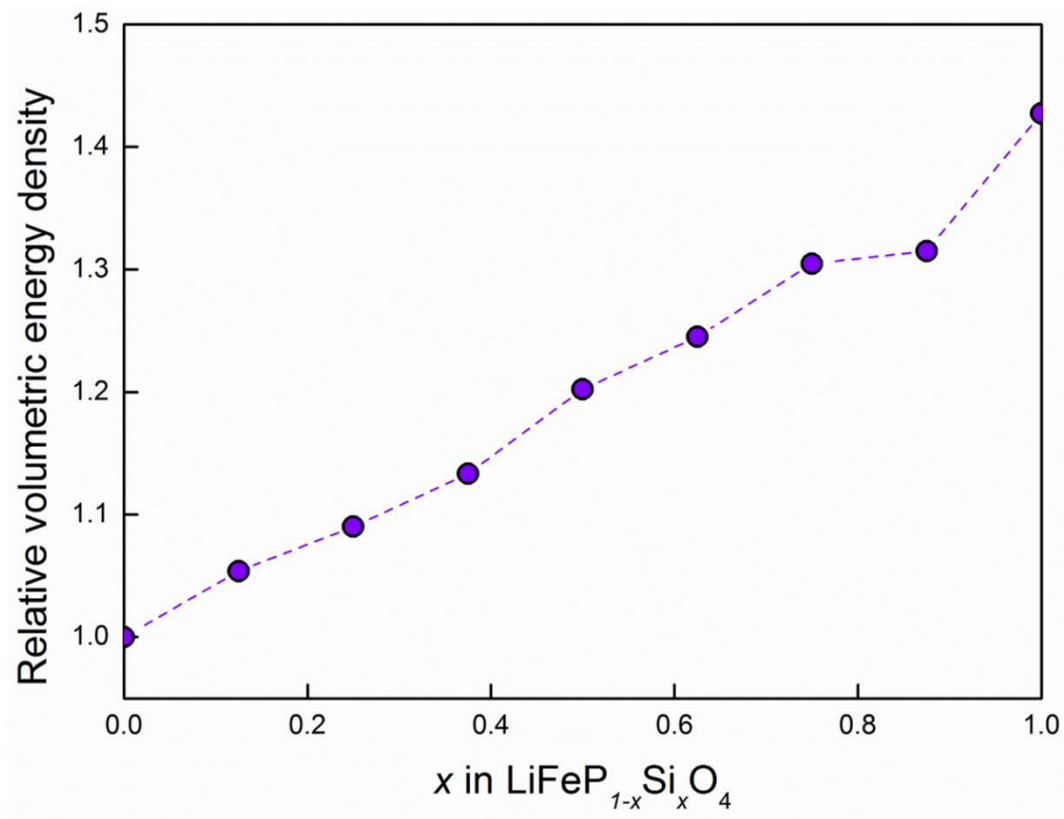
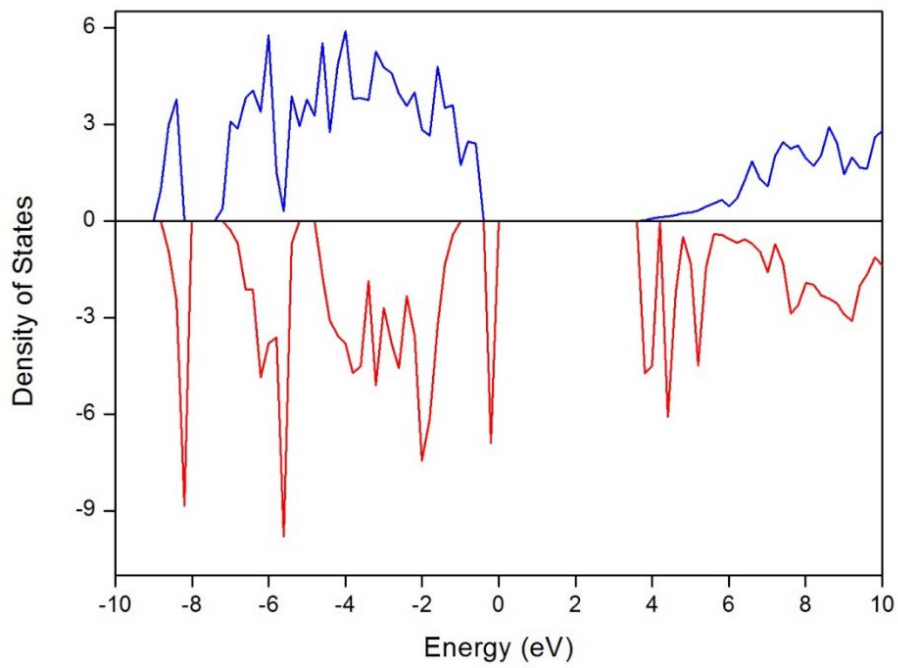


Fig.3.8. (a) Voltage of iron phosphor-silicate for olivine structure  $\text{LiFeP}_{1-x}\text{Si}_x\text{O}_4$  according to Si ratio ( $x=0\sim 1$ ) (b) Voltage profiles of olivine structure  $\text{LiFePO}_4$ ,  $\text{LiFeP}_{0.5}\text{Si}_{0.5}\text{O}_4$  and  $\text{LiFeSiO}_4$  as Li concentration.

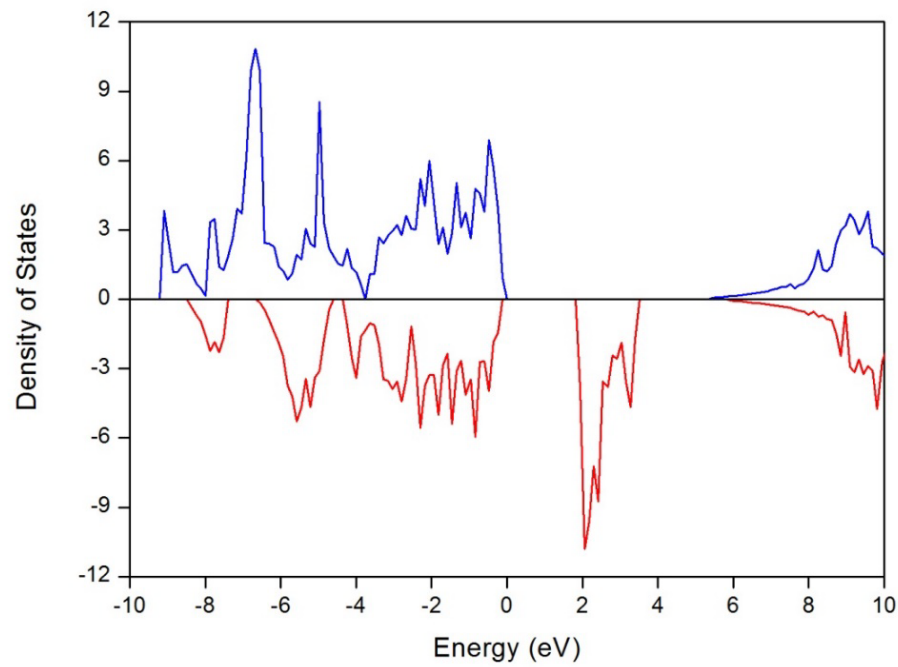


**Fig.3.9. Relative volumetric energy densities of iron phosphor-silicate for olivine structure  $\text{LiFeP}_{1-x}\text{Si}_x\text{O}_4$  compared with pristine iron phosphate  $\text{LiFePO}_4$ .**

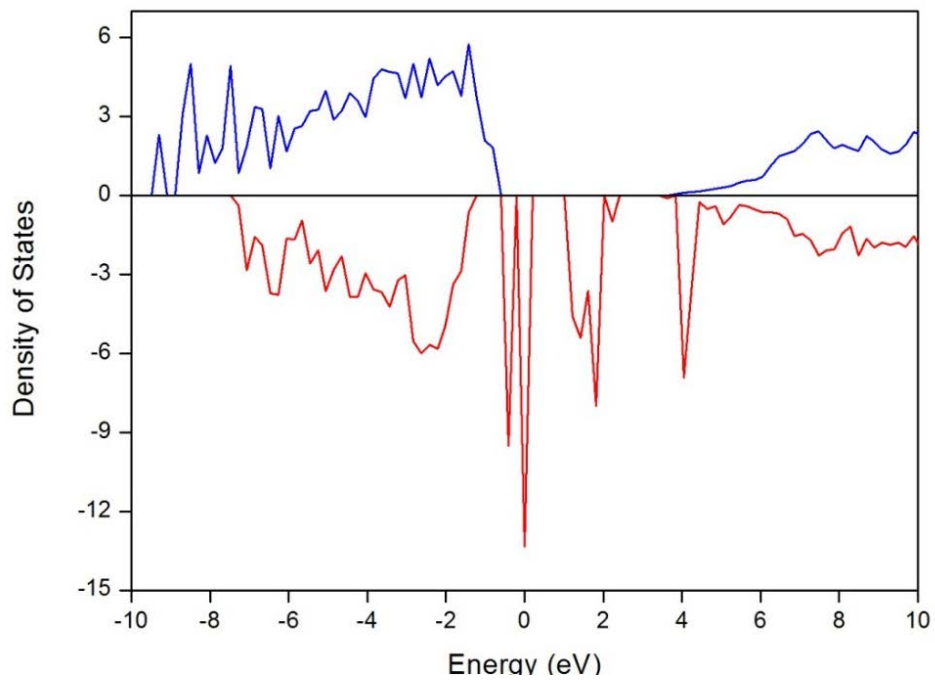
**(a)**



**(b)**



(c)



**(d)**

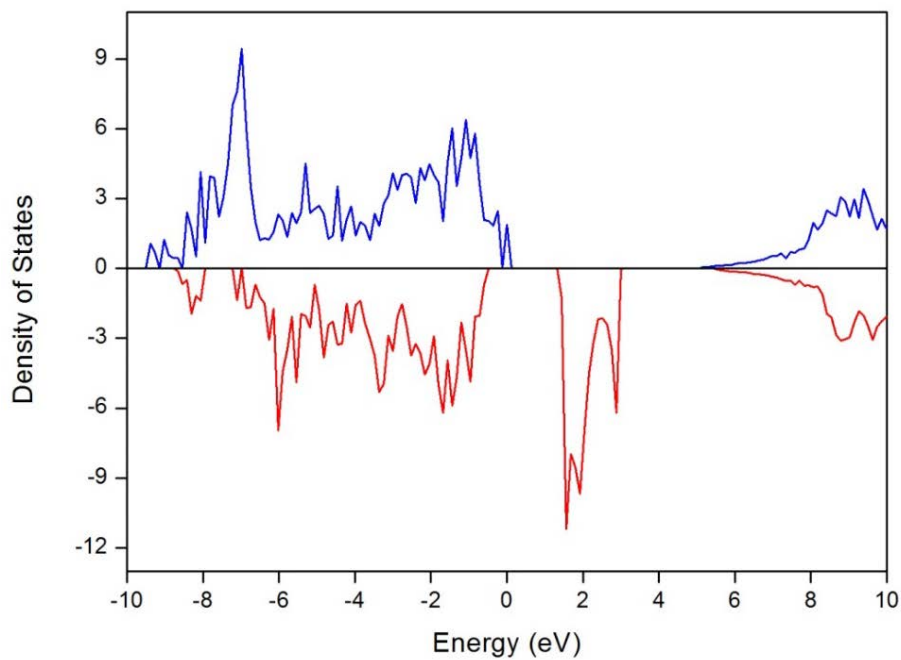


**Fig.3.10. Total density of states (TDOS) of iron phosphate and iron phosphor-silicate for olivine structure  $\text{LiFeP}_{1-x}\text{Si}_x\text{O}_4$  ( $x= 0$  and  $0.5$ ) (a)  $\text{LiFePO}_4$  (b)  $\text{FePO}_4$  (c)  $\text{LiFeP}_{0.5}\text{Si}_{0.5}\text{O}_4$  and (d)  $\text{FeP}_{0.5}\text{Si}_{0.5}\text{O}_4$ .**

## 4. Several anion doped at olivine $\text{LiFePO}_4$ material

### 4.1. Introduction of phosphate and anion type

In the previous study, we mentioned about poly-oxyanion cathode materials, and recent works have been studied phosphate and silicate that divided largely.<sup>63</sup> And the two type poly-oxyanion compounds have various transition metals, like Fe, Mn, Ni and Co. Also, a novel designed phosphate when substituted from phosphorus to silicate is show the higher voltage, higher electronic conductivity, and preventing anti-site defect. Moreover, if control the silicon proportion, the materials can control the voltage, so used several electronic devices. Furthermore, based on the research results, we motivated the design for other anion substitution for iron phosphate cathode material. Through the periodic table, there are determined five candidates, arsenic (As), antimony (Sb), germanium (Ge), tin (Sn) and selenium (Se), and the candidate elements are shown in Fig.4.1. For determined candidates, the most important factor is charge contents, at first, arsenic and antimony belong to same table with phosphorus. Next, germanium and tin belong to same table with silicon. Finally, selenium belongs to a different table with phosphorus or silicon, however, the element has the many charge contents compared with phosphorus and silicon, it is predicted the element has advantages for charge distribution for used cathode materials of Li-ion batteries.

Before the designed the new cathode materials, total energy and atomic radius are

investigated used first principles study to confirm the suitable elements for the insertion of phosphate materials. If the properties significant different from the original properties of phosphorus, the results mean that the elements not suitable for substituted to phosphate crystal structure. So the calculated total energy and atomic radius of phosphorus and candidate elements are shown in Fig.4.2. At first, thermodynamic total energy of candidate elements is very similar with the energy of phosphorus and the blue bars show these results. Hence, substitution from phosphorus to the candidate elements at phosphates crystal structure is suitable thermodynamically. Secondly, the atomic radius of phosphorus and candidate elements are shown in red bars of Fig.4.2. Atomic radius of Se smaller than P, and the radius of Ge and As bigger than the P. but the difference is a little. Hence, if substituted from P to Se, Ge and As for phosphates crystal structure, structural distortion is small kinetically. The atomic radius of Sn and Sb is bigger than the radius of P. On the contrary to previous results, structural distortion is bigger for used substituted elements, Sn and Sb.

## **4.2. Theoretical design of $\text{LiFeP}_{1-x}\text{V}_x\text{O}_4$ ( $\text{V} = \text{As, Ge and so on}$ )**

At first, computational methods are next that the ab initio calculations were based on the DFT method as implemented in the VASP code. A generalized gradient approximation (GGA) was used with the Perdew-Burke-Ernzerhof (PBE) functional of the exchange and correlation energy. For calculation, a projector augmented wave (PAW) method was selected to describe the interactions between the ion core and valence electrons.<sup>48</sup> For accurate interactions inside the d-orbitals of the transition metal, we used

GGA+U scheme. Within GGA+U scheme, effective Hubbard U  $U_{\text{eff}} = U - J$ , was used for Fe (4.3 eV) in the overall calculation. There was a difference of only a few milli-electron volts by using the GGA+U method. We used an energy cutoff for the plane wave basis set was 600 eV and the k-point mesh in the Monkhorst pack scheme was set to 4x4x4. For this research, various atom elements used for calculation, but used U and J values are same with all structures. J value is always used for same value, unity, and U value is only related to atom elements that have d orbitals at charge state. In this section, only transition metal iron has d orbital at the charge state among calculated all structures. Therefore, when used GGA+U method, we considered only transition metal iron, so U value is the same value 5.3 eV for entire structures. The atomic coordinates and cell parameters were fully relaxed to optimize the crystal structures. For the find the optimized structure, at first it is optimized iron phosphate crystal structure thermodynamically, using the ab-initio study. Next, substituted from V to P for optimized iron phosphates structure (V = As, Sb, Ge, Sn and Se) each candidate elements, next find the optimized substituted crystal thermodynamically. For find the optimized structures, we calculated formation energy, and the equation is shown in 4.2.1. And the equation is same with the previous section to find the optimized structures of  $\text{LiFeP}_{1-x}\text{Si}_x\text{O}_4$  ( $x = 0 \sim 1$ ), and the optimized structures are shown in Fig.4.3.

$$\text{Formation energy}_{\text{LiFeSi}_{1-x}\text{P}_x\text{O}_4} = E_{\text{LiFeSi}_{1-x}\text{P}_x\text{O}_4} - [(1-x)E_{\text{LiFeSiO}_4} + xE_{\text{LiFePO}_4}] \quad (4.2.1)$$

where E is the total energy of the material sub-text and x is the number of silicon atoms that have been added per formula unit. At first, substituted position of inserted anion elements is same. Fig.4.3a is shown  $\text{LiFeP}_{0.875}\text{V}_{0.125}\text{O}_4$  (V = As, Sb, Ge, Sn and Se) crystal

structure. Moreover, Fig.4.3b is shown  $\text{LiFeP}_{0.75}\text{V}_{0.25}\text{O}_4$  crystal structure, Fig.4.3c is shown  $\text{LiFeP}_{0.625}\text{V}_{0.375}\text{O}_4$  crystal structure, Fig.4.3d is shown  $\text{LiFeP}_{0.5}\text{V}_{0.5}\text{O}_4$  crystal structure, Fig.4.3e is shown  $\text{LiFeP}_{0.375}\text{V}_{0.625}\text{O}_4$  crystal structure, Fig.4.3f is shown  $\text{LiFeP}_{0.75}\text{V}_{0.75}\text{O}_4$  crystal structure, Fig.4.3g is shown  $\text{LiFeP}_{0.125}\text{V}_{0.875}\text{O}_4$  crystal structure and Fig.4.3h is shown  $\text{LiFeVO}_4$  crystal structure ( $\text{V} = \text{As}, \text{Sb}, \text{Ge}, \text{Sn}$  and  $\text{Se}$ ). In these schematics, all polyhedral shapes are maintained original shapes not distorted. Next, the crystal structures are a little distorted even though substituted from phosphorus to other anions. Lattice parameters and volume will be discussed in next chapter in detail.

### **4.3. Improved performance of $\text{LiFeP}_{1-x}\text{V}_x\text{O}_4$ ( $\text{V} = \text{As}, \text{Ge}$ and so on)**

After finding the most optimized structures for each anion V proportion ( $\text{V} = \text{As}, \text{Sb}, \text{Ge}, \text{Sn}$  and  $\text{Se}$ ), we confirmed the lattice parameters and volume of the newly designed crystal structures. At first, lattice parameters and volume of  $\text{LiFeP}_{1-x}\text{As}_x\text{O}_4$  ( $x = 0 \sim 1$ ) are shown in Fig4.4. All lattice parameters and volume are increased according to the arsenic proportion. Atomic radius of arsenic is bigger than the radius of phosphorus, so the structure is expanded. But the expansion is 10% although all anions are substituted from phosphorus to arsenic. And the crystal structure maintains orthorhombic structure at the same space group, so the distortion of the structure is a little. Consequently, the  $\text{LiFeP}_{1-x}\text{As}_x\text{O}_4$  ( $x = 0 \sim 1$ ) structure can be used for cathode material of Li-ion batteries kinetically. Next is lattice parameters and volume of  $\text{LiFeP}_{1-x}\text{Sb}_x\text{O}_4$  ( $x = 0 \sim 1$ ), and the tendency is

shown in Fig.4.5. In these structures, the tendency is the same with  $\text{LiFeP}_{1-x}\text{As}_x\text{O}_4$  ( $x = 0 \sim 1$ ) because arsenic and antimony are the same groups for periodic table, but the expansion ratio is bigger. The reason is that the atomic number of antimony is 51 and the number of arsenic is 33, so antimony has a bigger atomic orbital compared with the orbital of arsenic, therefore has a bigger atomic radius. Because of the effect, the crystal structures substituted to antimony are more expanded than the structures substituted to arsenic, structural distortion is more occurred. Thus, if other properties are similar, arsenic substituted iron phosphate olivine structure is will be preferred for used cathode materials.

Thirdly, the crystal structures  $\text{LiFeP}_{1-x}\text{Ge}_x\text{O}_4$  ( $x = 0 \sim 1$ ) lattice parameters and volume are shown in Fig.4.6. As substituted from phosphorus to germanium, lattice parameters and volume are increased, the tendency is the same with previous studies, but the increased ratio is smaller than other previous structures. The results mean that germanium substituted iron phosphate olivine structures are most suitable for cathode materials of Li-ion batteries.

Fourth, lattice parameters and volume of  $\text{LiFeP}_{1-x}\text{Sn}_x\text{O}_4$  ( $x = 0 \sim 1$ ) are shown in Fig.4.7, and the tendency is similar to arsenic and antimony group compared with germanium and tin because the element belong to Ge with the same group of periodic table. So increased ratio higher than the crystal structures substituted to tin than to germanium. But the increased ration of the crystal structures substituted to tin is very similar to the crystal structures substituted to arsenic. Finally, lattice parameters and volume of  $\text{LiFeP}_{1-x}\text{Se}_x\text{O}_4$  ( $x = 0 \sim 1$ ) are shown in Fig.4.8. In common with previous studies, the lattice parameters and volume are increased and the tendency is similar to the crystal structures substituted to

antimony in the face of a smaller atomic ratio. The reason is the charge distribution the selenium and antimony belong to another period of periodic table.<sup>67</sup>

Next, we calculated voltage for most important factors for used cathode materials of Li-ion batteries. And equation for calculated theoretical intercalation voltage is given below.

$$V_{LiFeP_{1-x}V_xO_4} = \frac{G_{Li_2FeP_{1-x}V_xO_4} - G_{Li_1FeP_{1-x}V_xO_4} + (y_2 - y_1)G_{Li}}{y_2 - y_1} \quad (4.3.1)$$

At first, intercalation voltages of  $LiFeP_{1-x}As_xO_4$  ( $x = 0 \sim 1$ ) according to arsenic proportion are shown in Fig4.9, and the voltages of  $LiFeP_{1-x}Sb_xO_4$  ( $x = 0 \sim 1$ ) according to antimony proportion are shown in Fig.4.10. At first, voltage plateau shows the very stable line, therefore the materials reacted based on a two-phase reaction, and the inclination is same with original iron phosphate cathode material. Next, voltage is shown following the arsenic and antimony ratio, and the voltage values of arsenic substituted structures have almost same values of 3.47V except for  $LiFeSbO_4$ . The material has only a 3.0V voltage. And the values are the same or low with original iron phosphate's voltage. Therefore, the crystal structures  $LiFeP_{1-x}As_xO_4$  ( $x = 0 \sim 1$ ) and  $LiFeP_{1-x}Sb_xO_4$  ( $x = 0 \sim 1$ ) cannot show the advantages for electrochemical properties, and the reason is that arsenic is affiliated with phosphorus, so entire crystal structures substituted from phosphorus to arsenic have same charge distribution because the arsenic has same charge state. In previous study, the newly designed structures are expanded according to arsenic and antimony ratio, thus not suitable for cathode materials compared with original iron phosphates because they have not advantaged. Next, the intercalation voltages of  $LiFeP_{1-x}Ge_xO_4$  ( $x = 0 \sim 1$ ) according to

germanium proportion are shown in Fig.4.11. The intercalation voltage increased up to 4.78V according to the germanium proportion. Besides, the structures are very stable because the degree of increase is linear. The strong inductive effect between germanium and oxygen is occurred the intercalation voltage rising. Consequently, the crystal structures  $\text{LiFeP}_{1-x}\text{Ge}_x\text{O}_4$  ( $x = 0 \sim 1$ ) are most appropriate for used cathode materials. Next, the intercalation voltages of  $\text{LiFeP}_{1-x}\text{Sn}_x\text{O}_4$  ( $x = 0 \sim 1$ ) according to tin proportion are shown in Fig.4.12. Like germanium substituted iron phosphate structures, the intercalation voltage is increased according to the tin ratio for a strong inductive effect between tin and oxygen, but the structures are unstable for the bigger atomic radius of tin, hence the degree of increased is non-linear. At first, when substituted 0.125 mol tin, the voltage increased to 3.8V. But until substituted until 0.5 mol tin, intercalation voltage is maintained same value. Substituted tin over the 0.5 mol, voltage increased up to 4.3V. The intercalation voltage is reasonable, but structures are unstable, the increased voltage is not linear. Finally, the intercalation voltages of  $\text{LiFeP}_{1-x}\text{Se}_x\text{O}_4$  ( $x = 0 \sim 1$ ) according to selenium proportion are shown in Fig.4.13. The intercalation voltages show inconsistent performance according to selenium value, hence substituted selenium of iron phosphate structures are very unstable compared with the substituted other anions iron phosphate structures. Selenium and oxygen bonding has  $(\text{SeO}_4)^{2-}$ , so inductive effect becomes weak, moreover, iron redox process is  $\text{Fe}^{1+}/\text{Fe}^{2+}$  for the charging/discharging process, the charge state  $\text{Fe}^{1+}$  is very unstable, so the structure distortion is very huge electrochemically. Therefore, the substituted selenium of iron phosphate structures are most unsuitable for used cathode material of Li-ion batteries.

## 4.4. Summary

In this study, we designed the new poly-oxyanion structures based on anion exchange. Through the lowest formation energy, most optimized structures are found thermodynamically. At first, total five candidate anions are selected for periodic table, similar charge state. As and Sb are selected for same group with P, and Ge and Sn are selected for same group with Si. Se is near group with P and Si. Next step is that insert the candidate anions to phosphorus position for iron phosphate structure  $\text{LiFePO}_4$  step by step. So most optimized structures are selected for each substituted anions ratio. Using the calculated lattice parameters and volume, we selected most favorable anion that substitute for iron phosphate structure for used cathode material kinetically. As a calculate result, Ge is most favorable anion, next is As and Sn, and last is Sb and Se. Calculate voltage profile show that voltage can control according to anion type and ratio. When used the As and Sb, voltage profile consistent although change the anion ratio. Next when used the Ge and Sn, voltage profile is increased according to substituted the anion ratio. When substituted Se anion, the voltage is almost randomly, so structures are very unstable because of iron charge state. Consequently, Ge is most favorable anion for substitution of iron phosphate olivine structure because structures are very stable Ge inserted various ratio, and voltage is increased up to 4.87V linearly. The theoretical studies show the significant insight for design new cathode materials and  $\text{LiFeP}_{1-x}\text{Ge}_x\text{O}_4$  ( $x = 0 \sim 1$ ) are promising cathode

materials of Li-ion batteries.

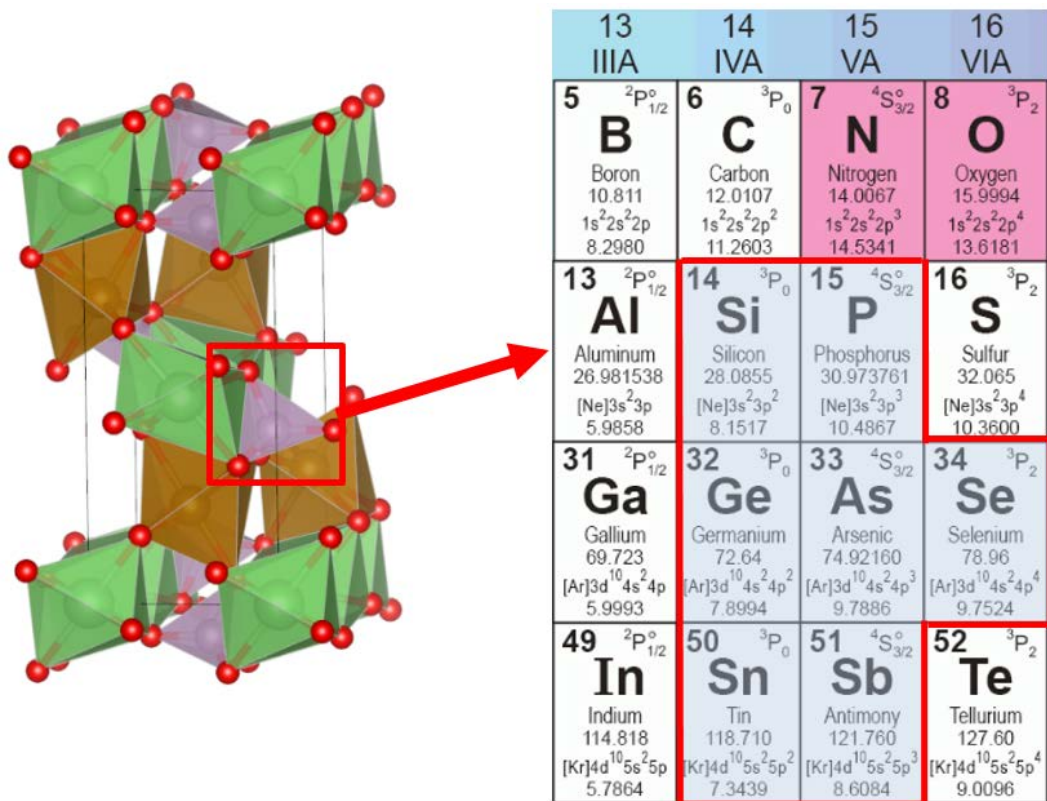


**Fig.4.1. Olivine structure  $Pnma$  space group and periodic table for show original anion elements Si, P and the anion candidates substituted for original anion position As, Sb, Ge, Sn and Se.**

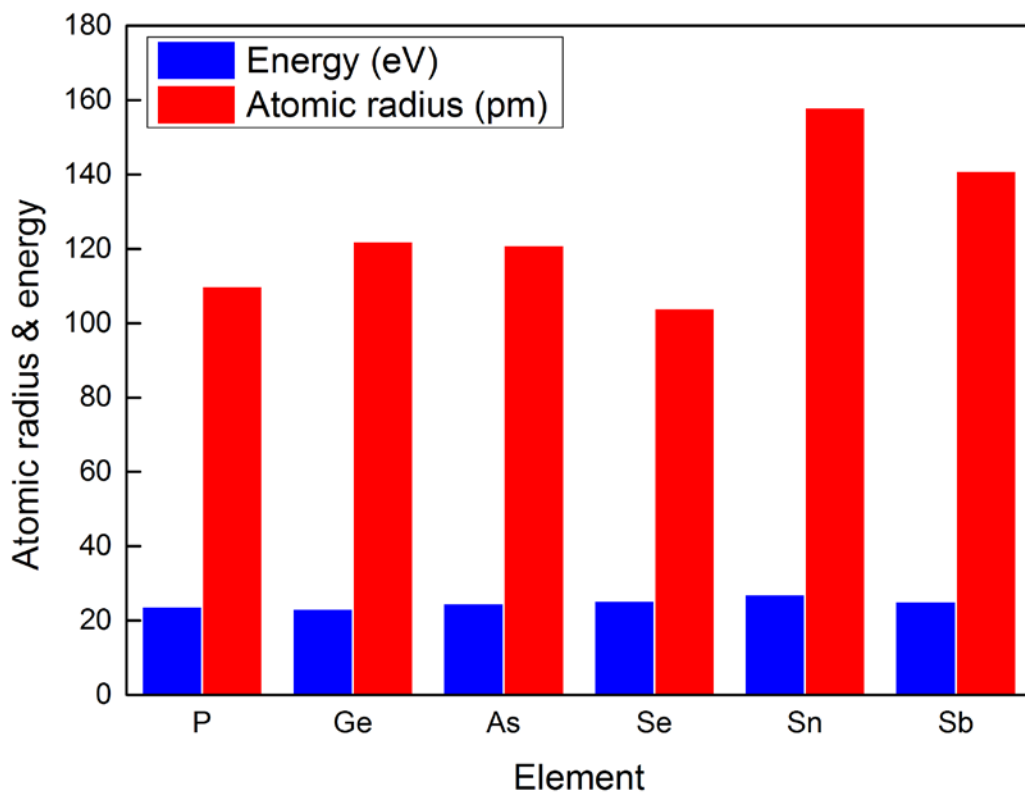
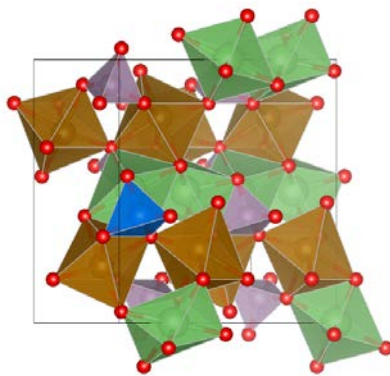
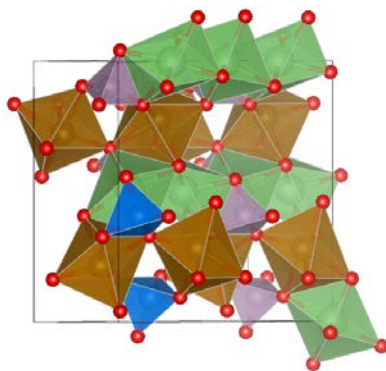


**Fig.4.2.** Thermodynamic total energy and atomic radius the anion candidates substituted for original anion position As, Sb, Ge, Sn and Se. Blue bars mean that total energy of ground state of the candidate anions and red bars are mean that atomic radius of the candidate anions.

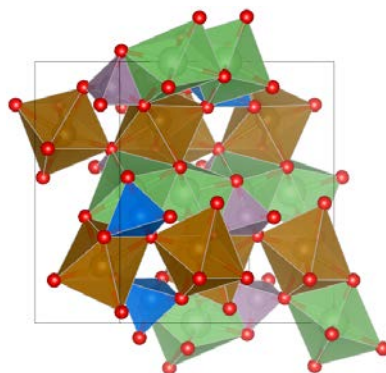
**(a)**



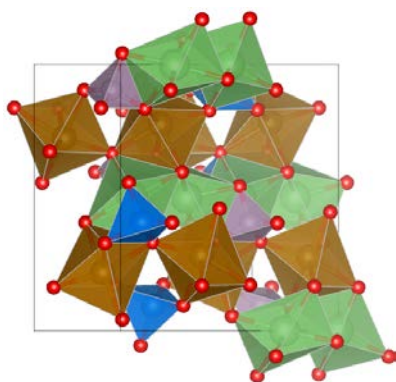
**(b)**



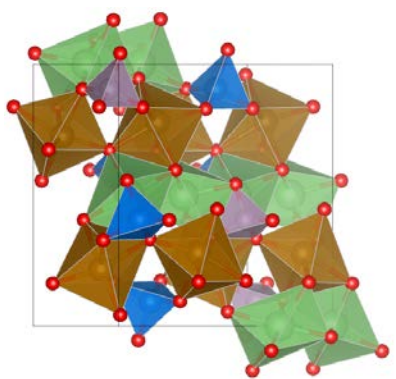
**(c)**



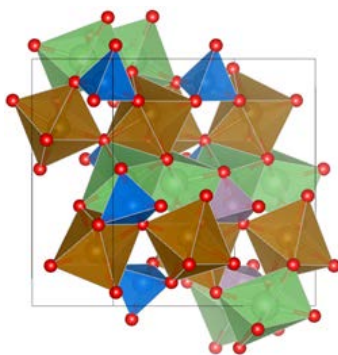
**(d)**



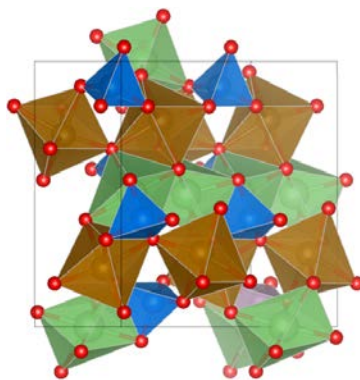
**(e)**



**(f)**



**(g)**



**(h)**

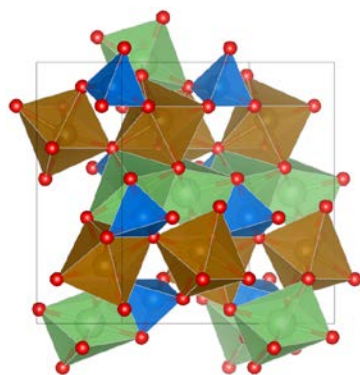
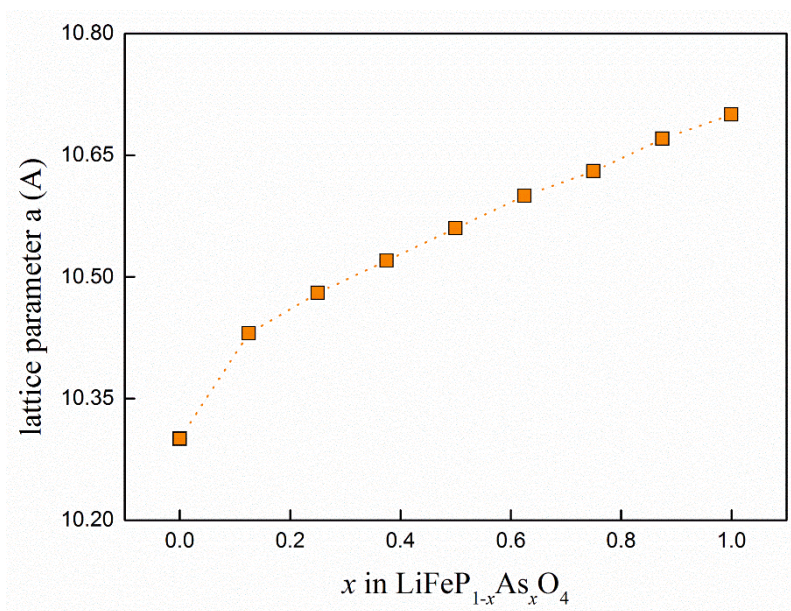
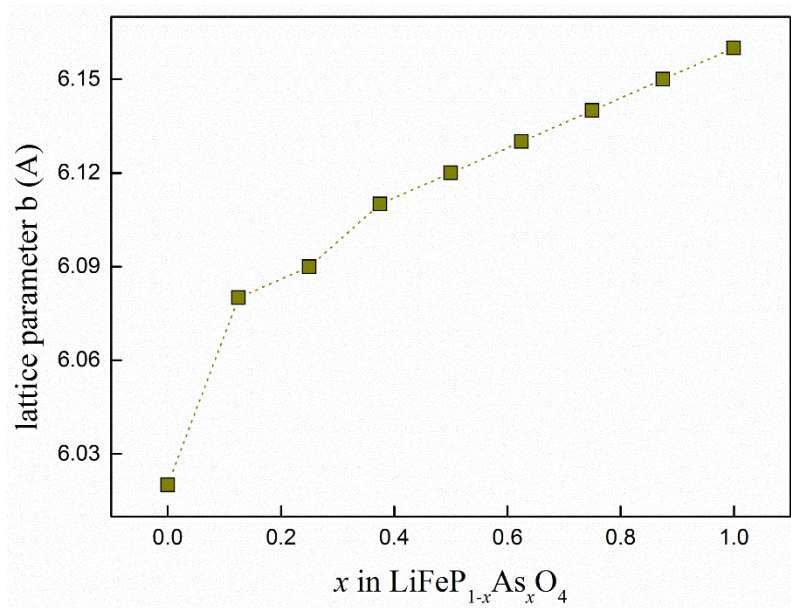


**Fig.4.3. Entire schematics of  $\text{LiFeP}_{1-x}\text{V}_x\text{O}_4$  (a)  $x = 0.125$ , (b)  $x = 0.25$ , (c)  $x = 0.375$ , (d)  $x = 0.5$ , (e)  $x = 0.625$ , (f)  $x = 0.75$ , (g)  $x = 0.875$  and (h)  $x = 1$**

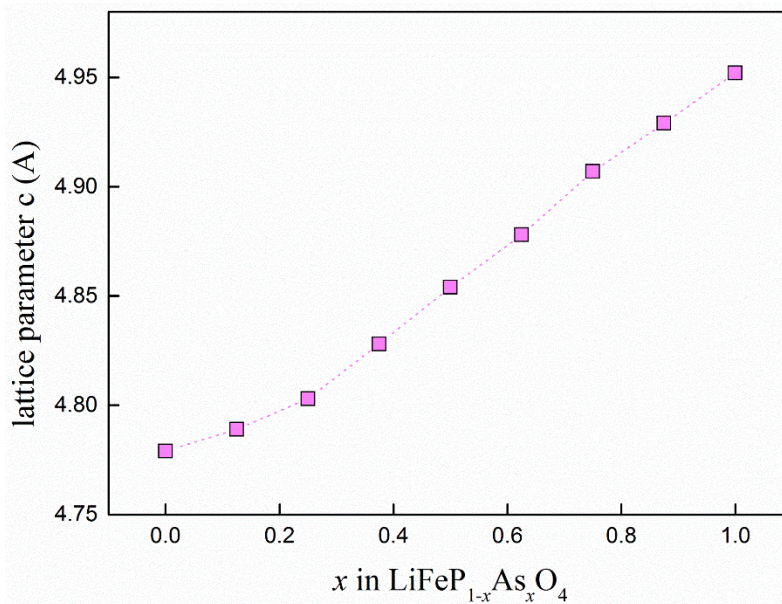
**(a)**



**(b)**



(c)



(d)

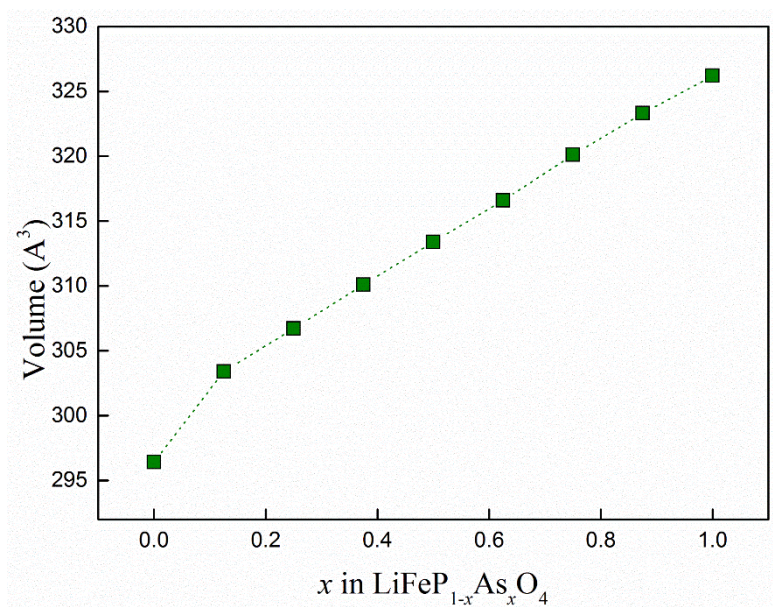
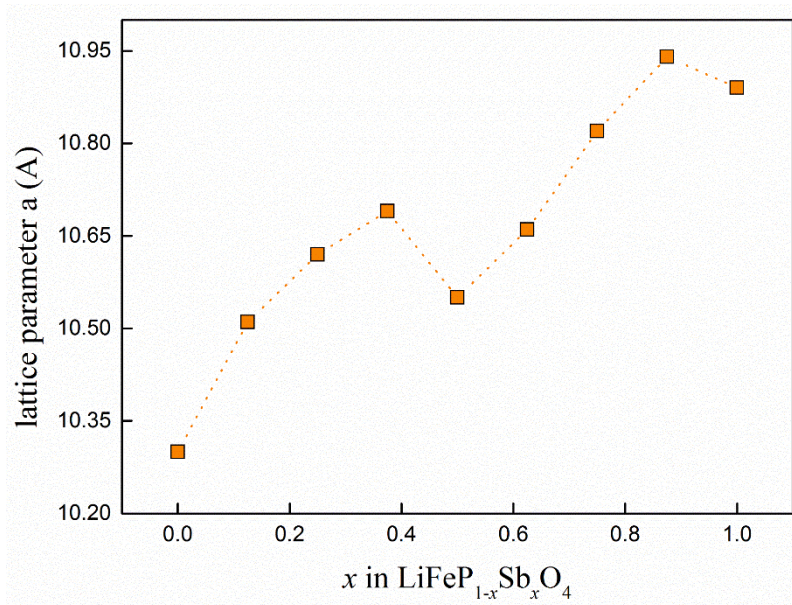
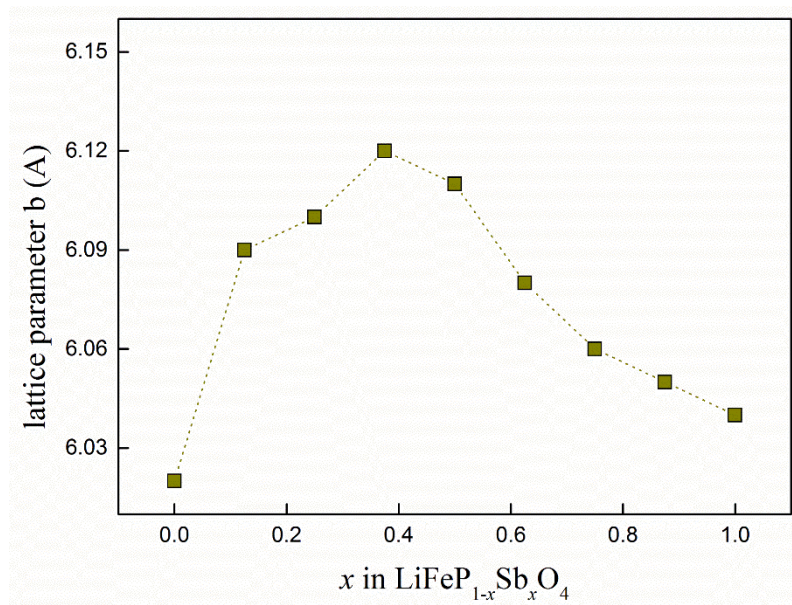


**Fig.4.4.** Lattice parameters (a)  $a$ , (b)  $b$ , and (c)  $c$  (Å) and (d) volume (Å<sup>3</sup>) per formula unit (f.u.) for olivine structures  $\text{LiFeP}_{1-x}\text{As}_x\text{O}_4$  that was the most optimized structure thermodynamically.

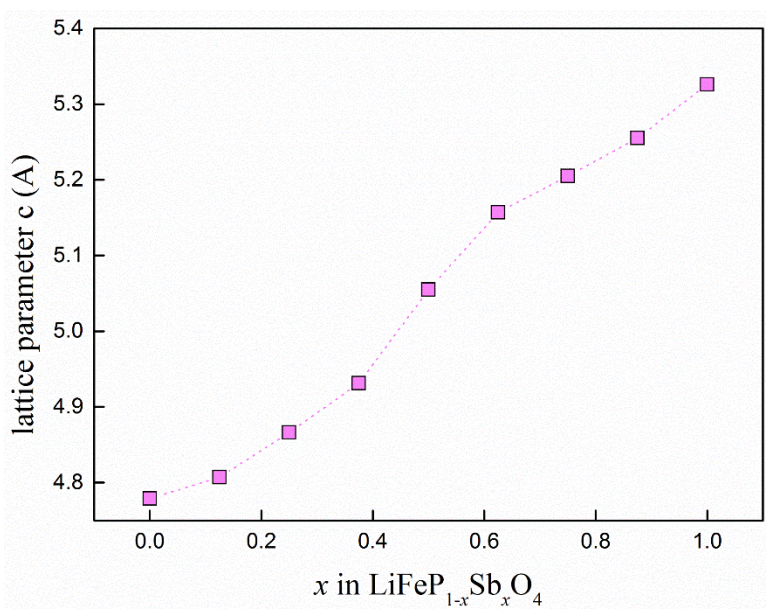
**(a)**



**(b)**



(c)



(d)

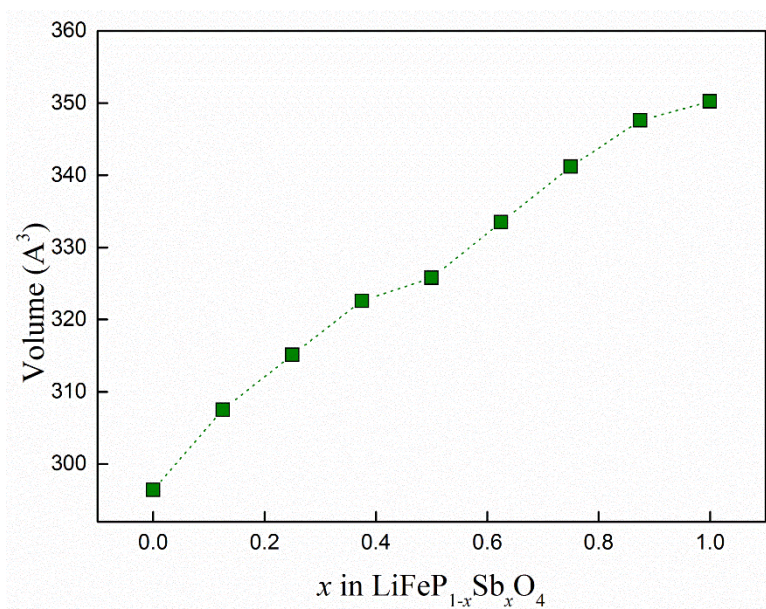
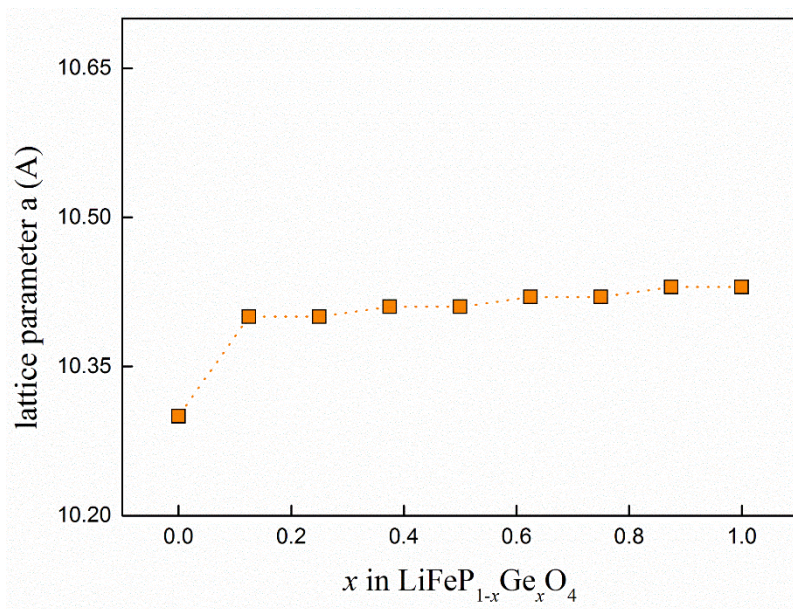
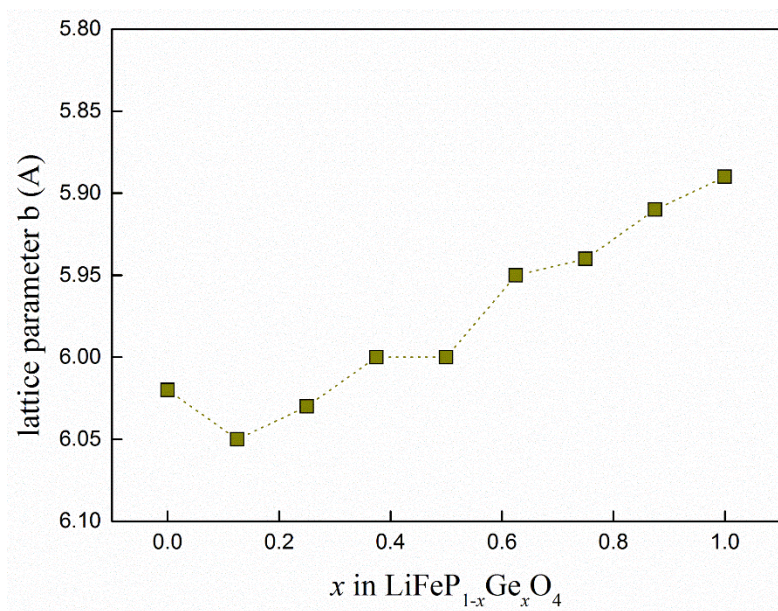


**Fig.4.5.** Lattice parameters (a) a, (b) b, and (c) c (Å) and (d) volume (Å<sup>3</sup>) per formula unit (f.u.) for olivine structures  $\text{LiFeP}_{1-x}\text{Sb}_x\text{O}_4$  that was the most optimized structure thermodynamically.

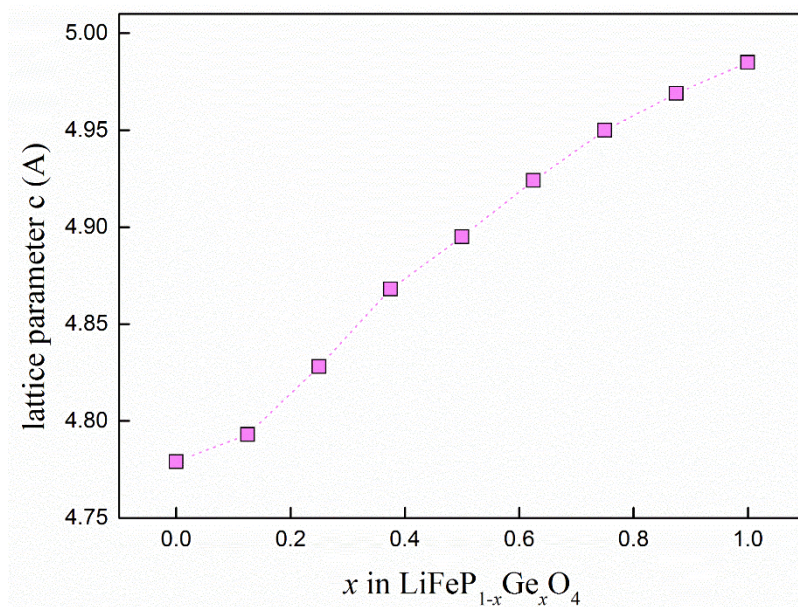
**(a)**



**(b)**



(c)



(d)

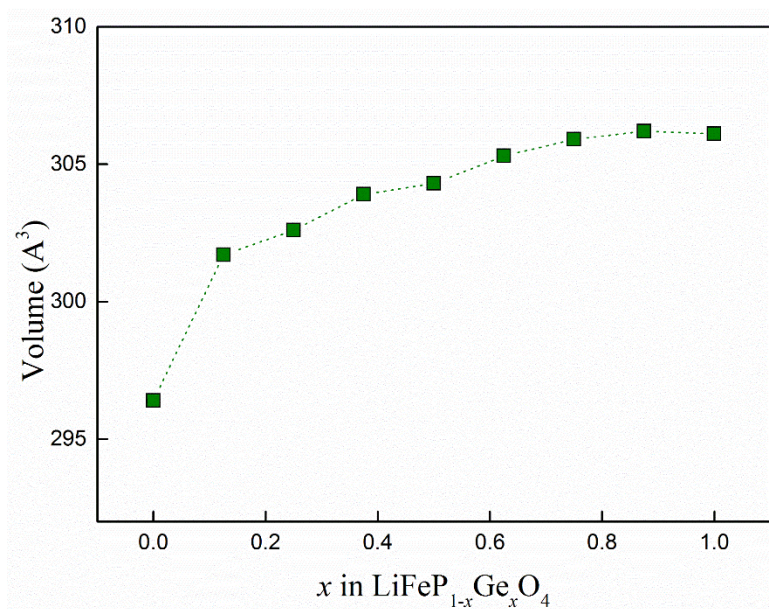
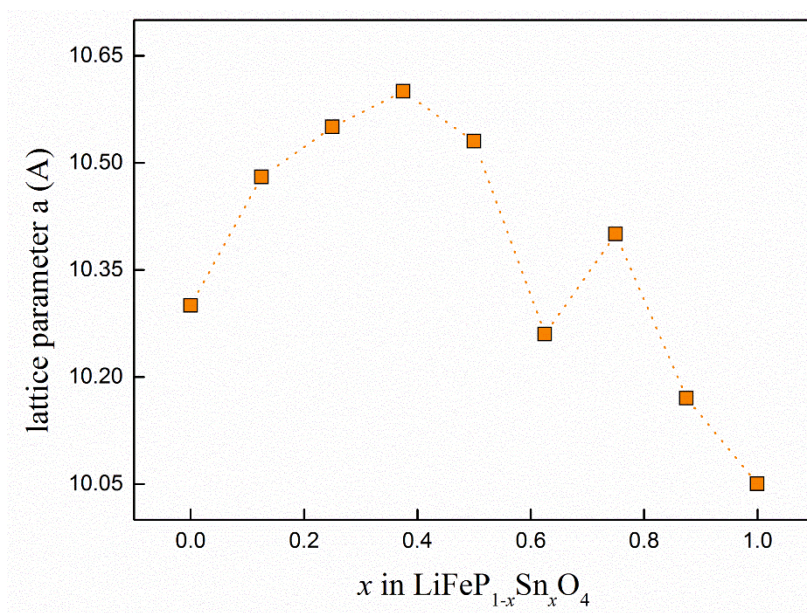
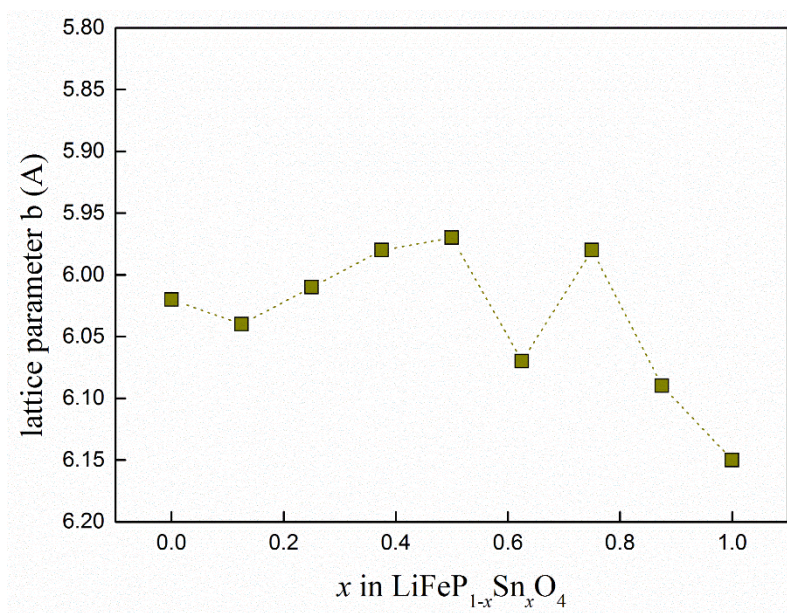


**Fig.4.6.** Lattice parameters (a) a, (b) b, and (c) c (Å) and (d) volume (Å<sup>3</sup>) per formula unit (f.u.) for olivine structures  $\text{LiFeP}_{1-x}\text{Ge}_x\text{O}_4$  that was the most optimized structure thermodynamically.

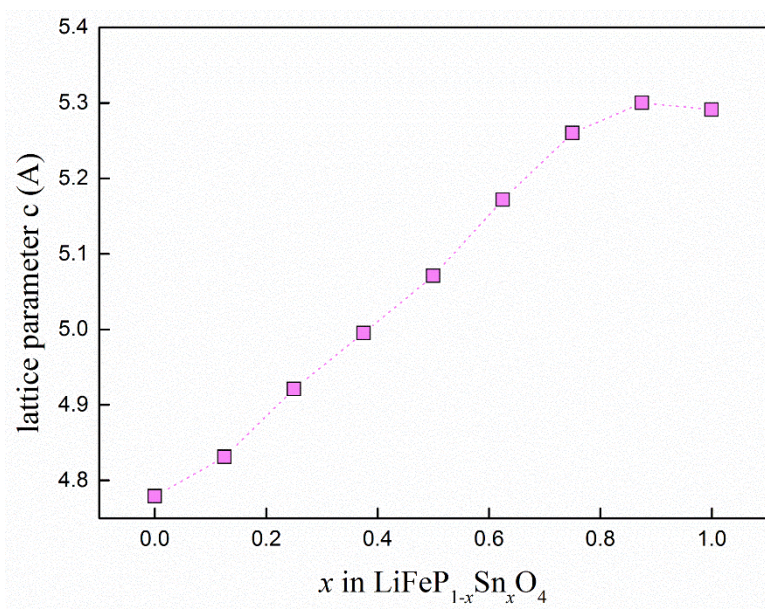
**(a)**



**(b)**



(c)



(d)

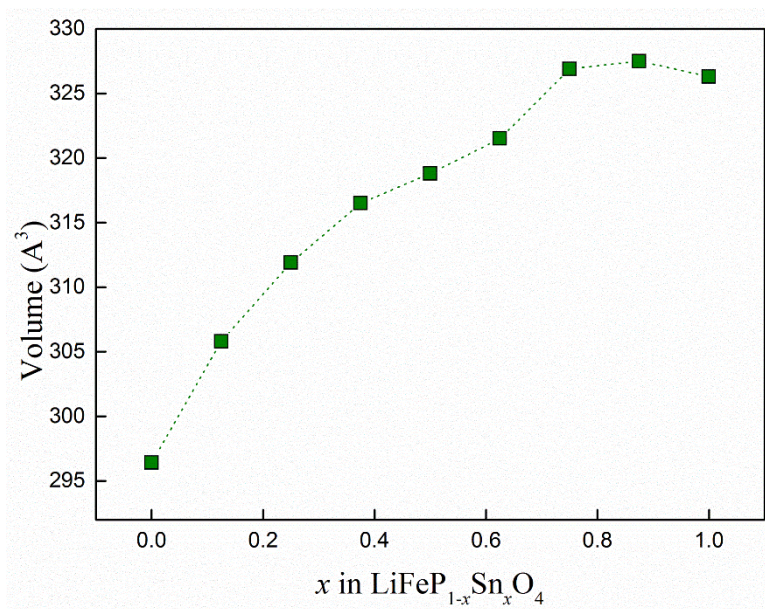
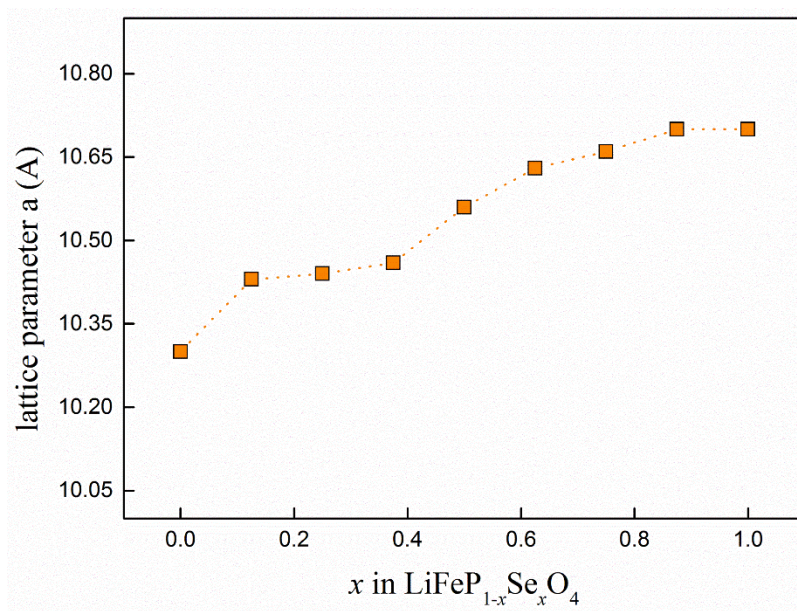
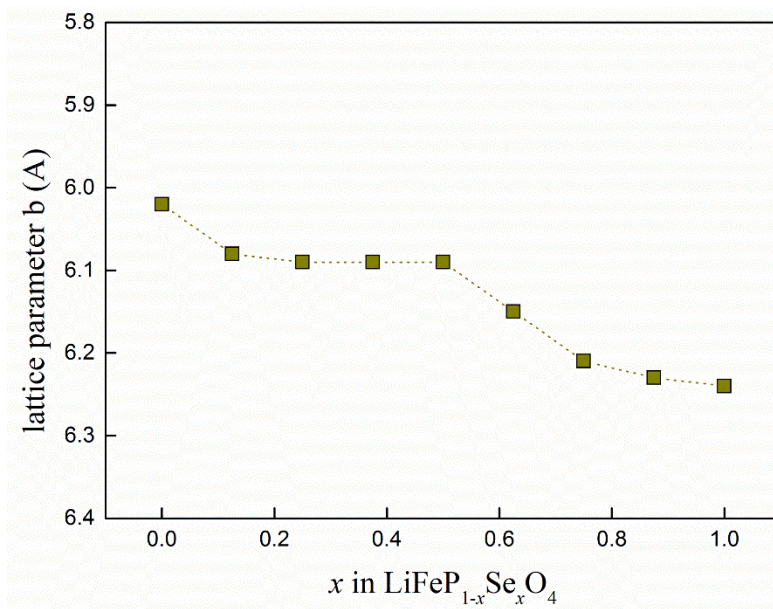


**Fig.4.7.** Lattice parameters (a) a, (b) b, and (c) c (Å) and (d) volume (Å<sup>3</sup>) per formula unit (f.u.) for olivine structures  $\text{LiFeP}_{1-x}\text{Sn}_x\text{O}_4$  that was the most optimized structure thermodynamically.

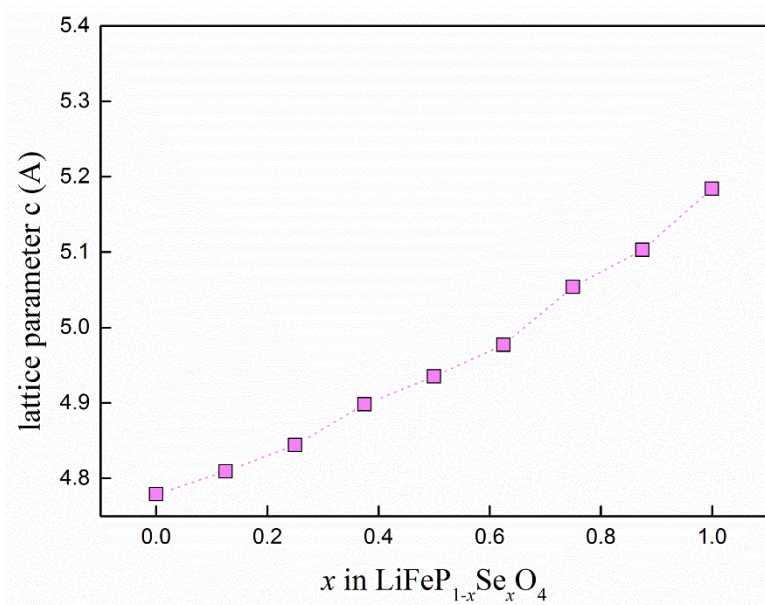
**(a)**



**(b)**



(c)



(d)

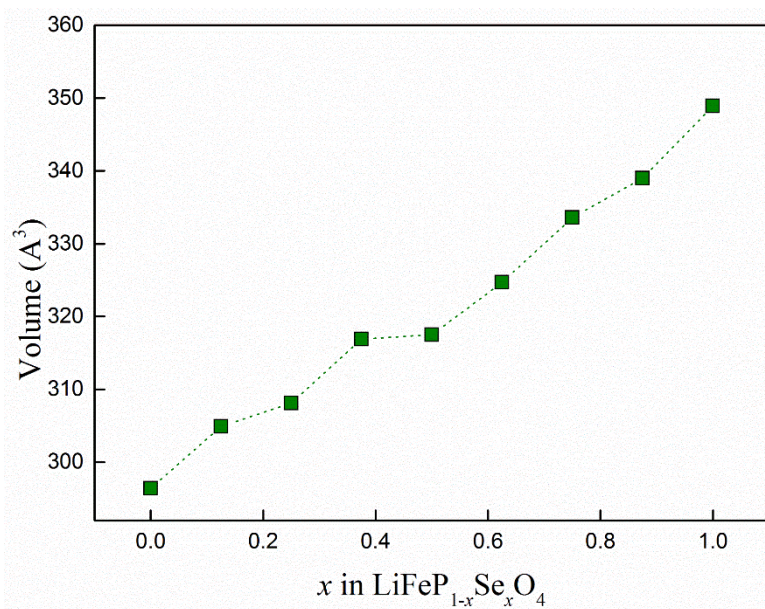


**Fig.4.8.** Lattice parameters (a) a, (b) b, and (c) c (Å) and (d) volume (Å<sup>3</sup>) per formula unit (f.u.) for olivine structures  $\text{LiFeP}_{1-x}\text{Se}_x\text{O}_4$  that was the most optimized structure thermodynamically.

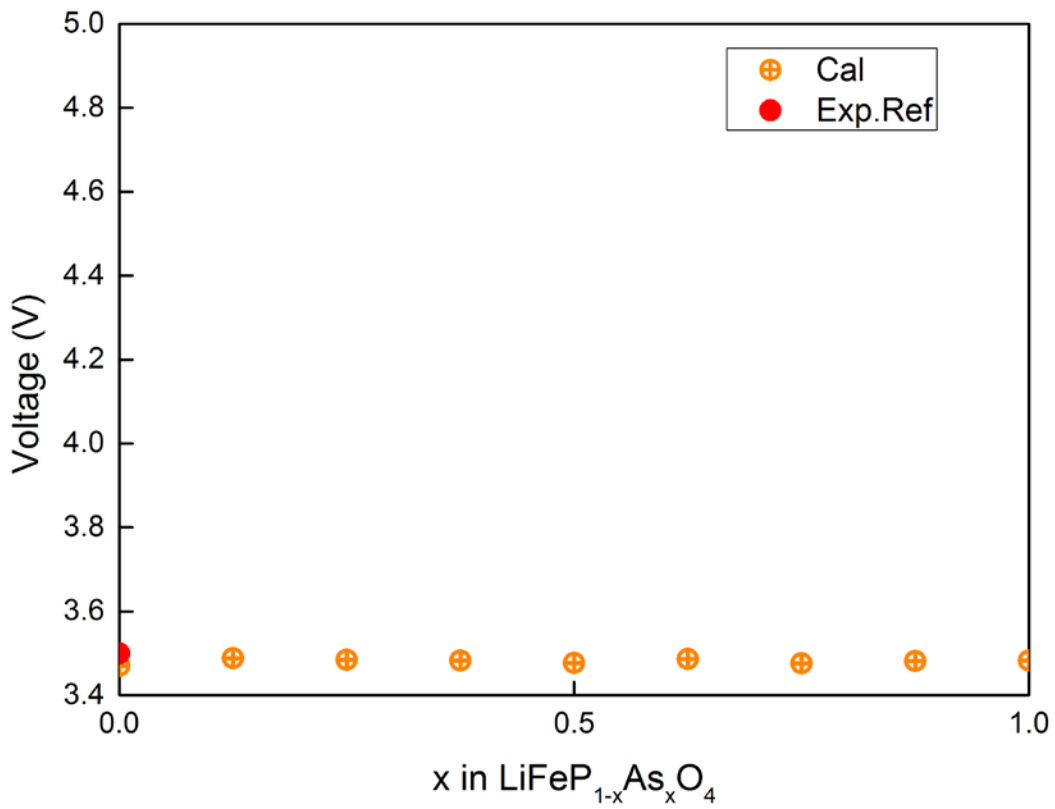


**Fig.4.9. Voltage profiles of olivine structures  $\text{LiFeP}_{1-x}\text{As}_x\text{O}_4$  according to substituted anions proportion ( $x = 0 \sim 1$ ).**

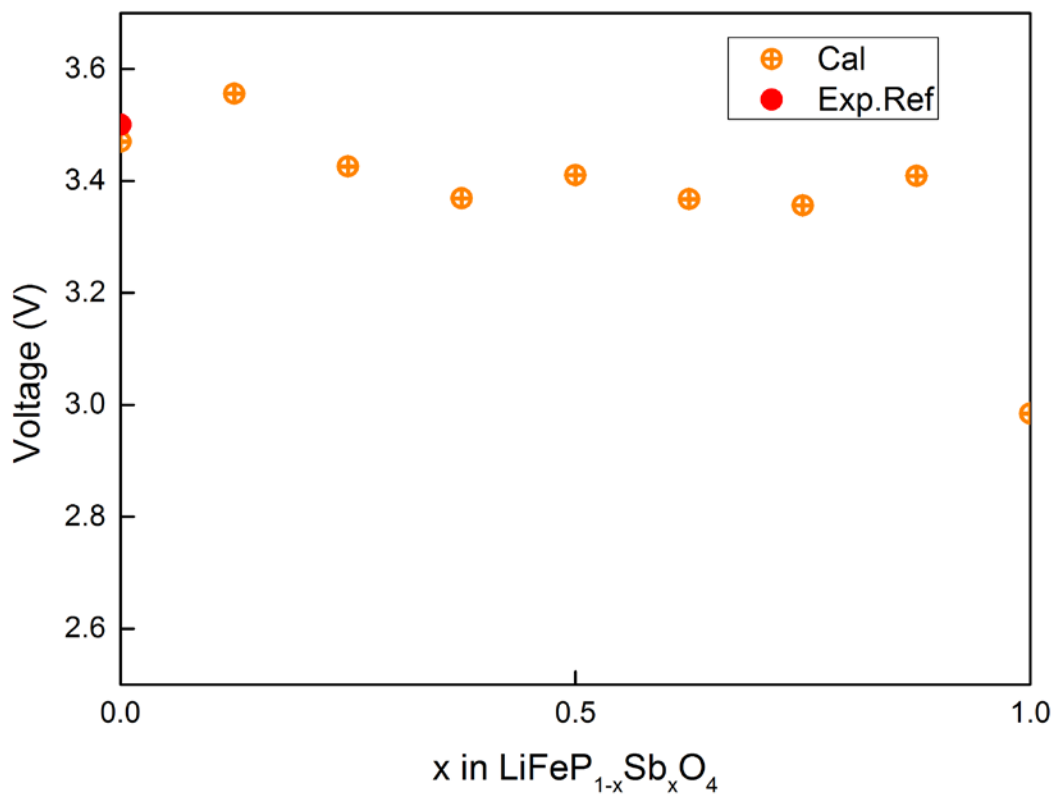


**Fig.4.10.** Voltage profiles of olivine structures  $\text{LiFeP}_{1-x}\text{Sb}_x\text{O}_4$  according to substituted anions proportion ( $x = 0 \sim 1$ ).

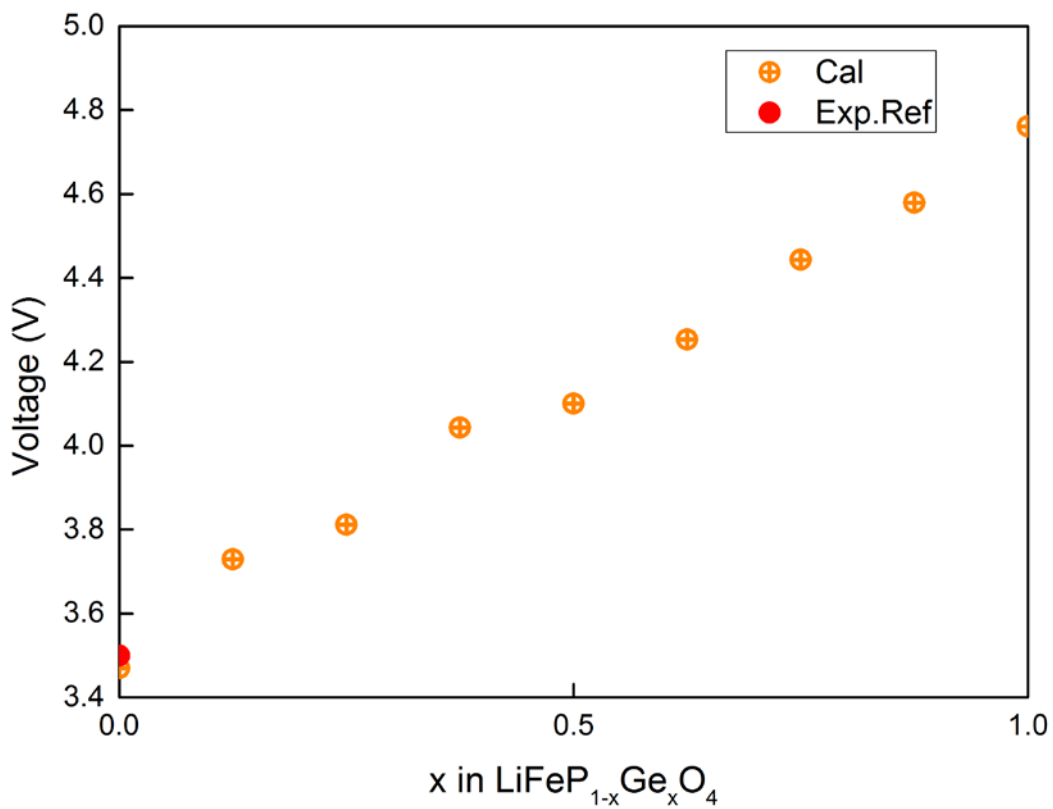


**Fig.4.11. Voltage profiles of olivine structures  $\text{LiFeP}_{1-x}\text{Ge}_x\text{O}_4$  according to substituted anions proportion ( $x = 0 \sim 1$ ).**

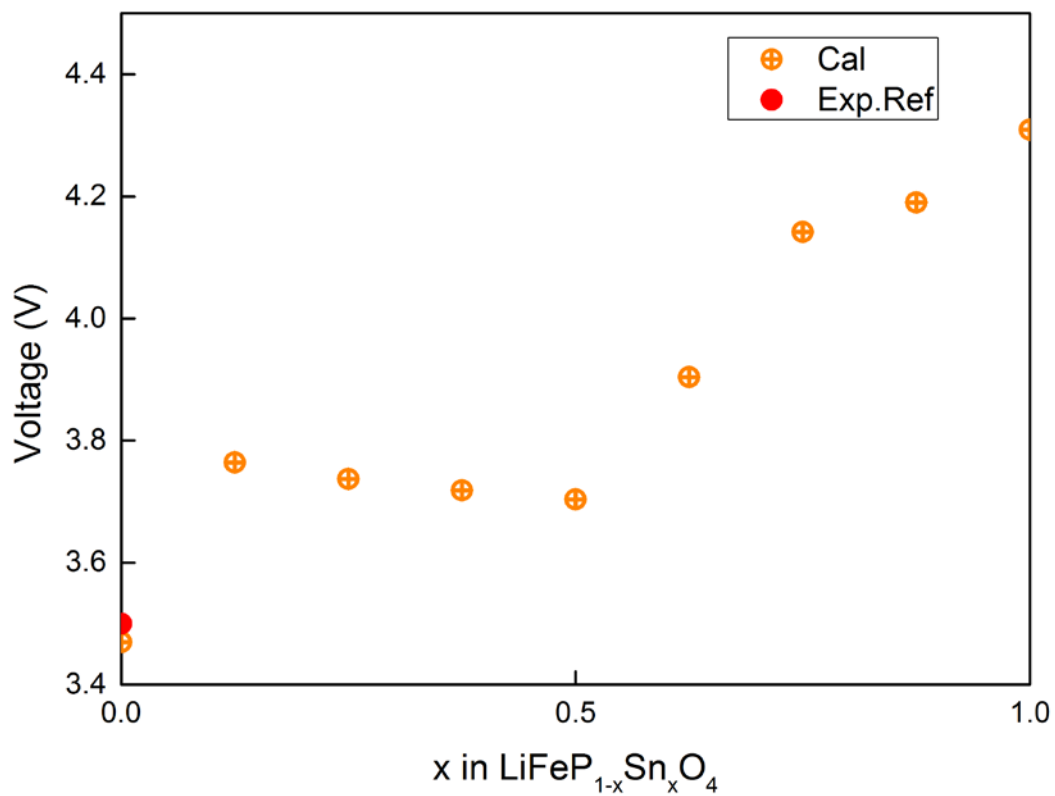


**Fig.4.12.** Voltage profiles of olivine structures  $\text{LiFeP}_{1-x}\text{Sn}_x\text{O}_4$  according to substituted anions proportion ( $x = 0 \sim 1$ ).

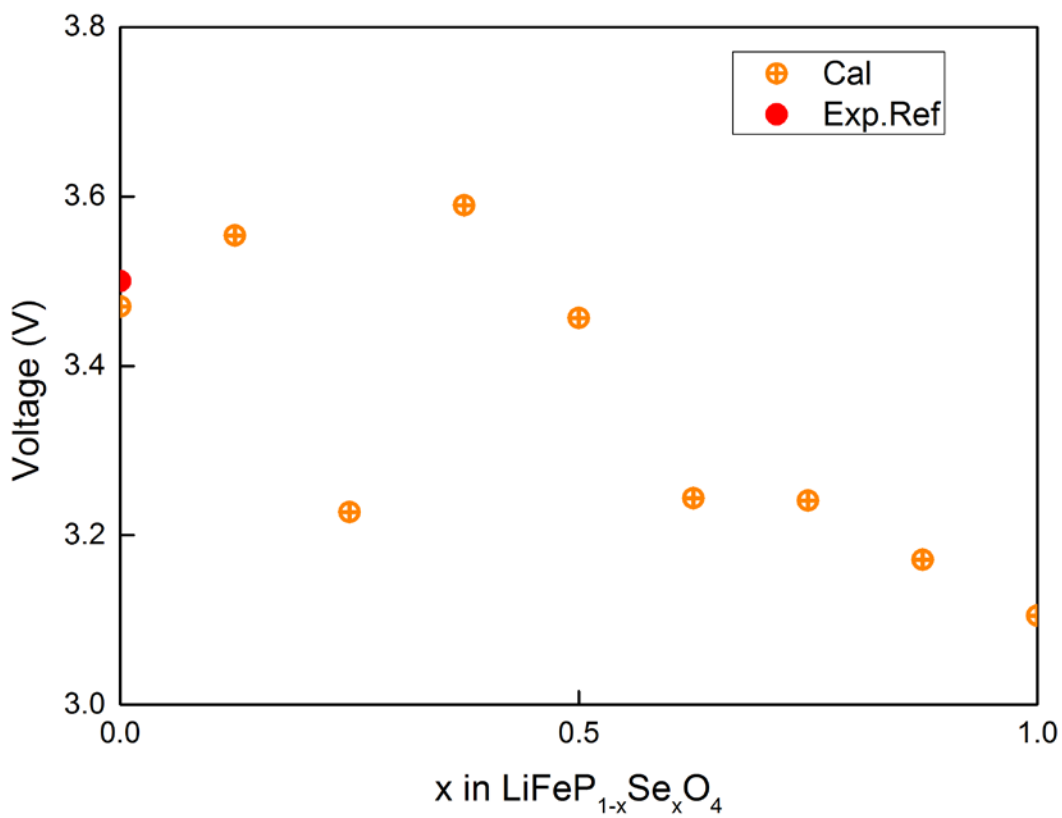


**Fig.4.13.** Voltage profiles of olivine structures  $\text{LiFeP}_{1-x}\text{Se}_x\text{O}_4$  according to substituted anions proportion ( $x = 0 \sim 1$ ).

## 5. Multiscale analysis for existing and new designed polyoxyanion cathode materials

### 5.1. Phase field model bridging the atomic- and macro- scale

At first, first-principles calculations required basic information (e.g., the number of electrons, pristine crystal structure, and so on) from empirical calculations using fitting parameters for the atomistic study. Based on solving the time independent Schrodinger equation with exchange-correlation potential  $V$ , the entire information of the given system is calculated in the form of wave function  $\Psi$  using density functional theory (DFT) as follows:

$$H\Psi = T + V + U + V\Psi = E\Psi \quad (5.1)$$

where H means the Hamiltonian operator, T is the kinetic energy operator, V is the potential energy operator from the outer field, U is the electron-electron internal energy operator, and E indicates total energy.

As the previous study, the DFT method for implemented in the Vienna ab initio simulation package based on the plane-wave set with pseudopotentials of the projector augmented wave (PAW) was used for atomistic investigation. For the exchange correlation functional according to Perdew-Wang, the generalized gradient approximation (GGA) was used for calculation. For the transition metal including d-orbital, GGA+U method also used, a Hubbard type U correction into GGA to revise the precise value.<sup>74</sup> To

sample the k-point in the reciprocal space, the Monkhorst-Pack method was used and cut-off energy set for the appropriate calculation. The calculations based on DFT method is only can be calculated the materials for the atomic scale, however, the real battery is operated complicatedly and show the various electrical, chemical, and mechanical behaviors at the wide range time and size scales. Therefore, multiscale analysis that means simulation with scale bridging from small scale to larger scale is required to show the complex systems of battery because the existing single scale analysis is impossible to calculate the systems.

Therefore, there are used ab-initio calculation and phase field method for bridging from atomic scale to macroscale that connected with crystal structure and particle of the electrode cell in this study. Through the multiscale analysis, we can show the several macroscale behaviors of  $\text{Li}_{1-x}\text{FePO}_4$  (LFP) and  $\text{Li}_{1-x}\text{FeP}_{0.5}\text{Si}_{0.5}\text{O}_4$  (LFPS), and compared the performance for using electrode of lithium ion battery with dimensionless time flow ( $x = 0 \sim 1$ ).

Furthermore, based on the Butler-Volmer equation, current density can be calculated, and chemical potential is calculated based on Nernst equations.<sup>75-76</sup> Next, using the internal energy of the materials, the mixing enthalpy was described for the phase difference, and the equation as follows:

$$H_{mix,atom} = E_{Li,FeVO_4}^{atom} - (xE_{LiFeVO_4}^{atom} + (1-x)E_{FeVO_4}^{atom}) \quad (5.2)$$

In the equation,  $x$  is the contents of lithium,  $V$  is the type of anions. Next, based on the results, mixing enthalpy is recalculated for divides regions through the phase, and the

equation is next:

$$H_{mix,atom}^{i,f} = E_{Li_xFeVO_4}^{atom} - \left( \frac{x-x_i}{x_f-x_i} E_{Li_fFeVO_4}^{atom} + \frac{x_f-x}{x_f-x_i} E_{Li_iFeVO_4}^{atom} \right) \quad (5.3)$$

Furthermore, the mixing enthalpy equation is can be changed at the discretization phase, and the equation is next:

$$H_{mix,CP} = \sum \mathcal{E}_i^f (x-x_i)^2 (x_f-x)^2, x_i \leq x \leq x_f \quad (5.4)$$

In this equation,  $\mathcal{E}_i^f$  means enthalpy coefficient. Based on convex hull analysis, the value is obtained by mixing enthalpy, we can be predicted phase separation like one-phase reaction and two-phase reaction. Moreover modified combined enthalpy was calculated for the ground state energy and convex hull. Finally, multiscale based free energy  $f_{CP}$  is can be calculated for the next equation that used mixing enthalpy:

$$f_{CP} = H_{CP} + k_B T \{x \ln x + (1-x) \ln(1-x)\} \quad (5.5)$$

In the equation,  $k_B$  is Boltzmann constant and T is absolute temperature. For show the electrochemical phase transformation model with various phase model, Cahn-Hilliard energy function is selected based on the combined phase free energy model.<sup>77</sup> Based on the function, elastic strain field can be calculated based on the lattice misfit, and stress field can be calculated for Cahn-Hilliard equation equilibrium.<sup>31, 33, 78</sup>

And the basic Cahn-Hilliard equation is well defined as follows:

$$\frac{\partial c_i}{\partial t} = \nabla M_{ij} \nabla \frac{\delta F}{\delta c_j(r,t)} \quad (5.6)$$

Also, total free energy equation is well defined as follows:

$$F(f, c, \eta) = \int_V \left[ f(c, \eta) + \frac{\kappa_c}{2} (\nabla c)^2 + \frac{\kappa_\eta}{2} (\nabla \eta)^2 \right] dv \quad (5.7)$$

In this electrode system of Li-ion batteries, the phase is divided Li ion concentration, hence equation is changed because of  $c$  equal  $x$ . At first, Cahn-Hilliard equation is next:

$$\frac{\partial c_i}{\partial t} = \nabla(Mc\nabla\mu) \quad (5.8)$$

$M$  is mobility and  $\mu$  is chemical potential, and the free energy equation is next:

$$F(f, c) = \int_V \rho_n \left[ f(c) + \frac{\kappa_i^f}{2} + |\nabla c|^2 \right] + f_{el} dV, \kappa_i^f = \frac{n_d}{3} \lambda^2 \varepsilon_i^f \quad (5.9)$$

$\rho_n$  is the number of sites per volume  $V$ .

Finally, the entire numerical algorithm is well shown in the Fig.5.1.

## 5.2. Phase separation of existing and new-designed poly-oxyanion materials

In previous studies, phase separation of pristine iron phosphate is well established.<sup>79-80</sup> And the pristine iron phosphate show the strong phase separation because the material react perfectly two-phase reaction for charging/discharging process.<sup>81-82</sup> Therefore, LiFePO<sub>4</sub>/FePO<sub>4</sub> two phases are shown in reference.<sup>59</sup> For the precise comparison, we recalculated phase separation kinetics of LFP. Next, the phase separation of the newly designed LiFeP<sub>0.5</sub>Si<sub>0.5</sub>O<sub>4</sub>/FeP<sub>0.5</sub>Si<sub>0.5</sub>O<sub>4</sub> is calculated for used multiscale analysis. For this analysis, we calculated the mixing enthalpy of optimized LFP crystal structures following inverse Li contents, and the figure is shown in Fig.5.2. Next, mixing enthalpy of optimized

LFPs crystal structures following inverse Li contents, and the figure is shown in Fig.5.3. Moreover, free energy plots of LFP and LFPS are shown in Fig.5.4. Finally, phase separation plots following dimensionless time  $t$  are shown in Fig.5.5. In this figure, there is less occurred phase separation for the difference of Li ion concentration, charging/discharging process of Li-ion batteries. Therefore, stress according to phase separation is less applied for the electrode, and show the better rate capability and cyclic performance.<sup>83</sup> In these result, silicon ratio of pristine iron phosphate is can be controlled phase separation for better performance used for cathode materials of Li-ion batteries.

### **5.3. Strain field of existing and new-designed poly-oxyanion materials**

In previous research results, newly designed  $\text{LiFeP}_{1-x}\text{Si}_x\text{O}_4$  ( $x = 0 \sim 1$ ) cathode materials are showed superior performance compared with existing cathode material LFP like the voltage, electronic conductivity and so on. And we show the phase separation behaviors of LFP and LFPS for used multiscale analysis at the previous study. Moreover, we calculated strain field of the phase for precise analysis using lattice misfit. At first, the schematics of strain field  $\varepsilon_{xx}$  of LFP and LFPS are shown in Fig.5.6. Next the schematics of strain field  $\varepsilon_{yy}$  of LFP and LFPS are shown in Fig.5.7 and last the schematics of strain field  $\varepsilon_{xy}$  of LFP and LFPS are shown in Fig.5.8. In these figures, strain is strongly occurred at LFP particle compared with LFPS particle between different phases

independent of direction. These results mean that larger strain energy generated at LFP than LFPS during the charge/discharge process. Hence, LFPS has higher structural stability compare with LFP, so it has higher cyclability for the used electrode of lithium ion batteries. For detail analysis, we calculated stress field, and the research results are discussed at the next chapter.

#### **5.4. Stress field of existing and new-designed poly-oxyanion materials**

For the particle scale at electrode, we show the phase separation and strain field of the particle phase using multiscale analysis. Furthermore, we calculated stress field of LFP and LFPS electrode system for the used elastic constant of DFT simulation. And the stress is more generated for LFP system compared with LFPS system. In other words, when insertion/extraction lithium ions at these systems, LFPS is less generated stress than LFP, so show the more stable tendency and distortion and crack of particle is less occurred. And the stress is more generated for x direction at LFP system and less generated for y direction and shear direction. On the other hand, LFPS system is more generated for y direction compared with x and shear direction. Hence, LFP system is influenced by phase separation compared with lithium diffusion direction, however LFPS system is less influenced by phase separation compared with lithium diffusion. Finally, LFP system gives the stress for x direction and LFPS system is give the stress for y direction.

## 5.5. Summary

Through the DFT simulation and phase field method that is the multiscale analysis connected with atomic and particle scale of electrode in lithium ion batteries, it has been shown that phase separation, strain field and stress field of existing and newly designed poly-oxyanion cathode materials LFP and LFPS. Phase separation of LFP is stronger than the separation of LFPS during insertion and extraction of lithium ion, hence when used the lithium ion battery for these cathode materials, phase of LFPS is more stable than the phase of LFP. In other words, cyclability is better when used LFPS to cathode material than when used LFP to cathode material. Next, strain and stress field with the lithium ion concentration dependency for used LFP and LFPS to cathode material of lithium ion battery. A strain is more occurred at LFP cathode system than cathode system of LFPS material. Similarly, stress is more generated for the phase of LFP material than LFPS material. Moreover, when used LFPS material to cathode in lithium ion battery, reduce the tensile and compress stresses for any direction during the charging/discharging process. And the strain and stress are more generated for x direction for LFP, and less generated for y direction and shear direction. On the other hand, the LFPS electrode system is more generated for y direction compared with x and shear direction. The results mean that phase separation is more affected on the strain and stress than lithium diffusion direction for the LFP system, however, the LFPS system is a little occurred phase separation, so lithium

diffusion direction is more affected on the strain and stress generation. Consequently, the LFP system show the higher strain and stress generation for x direction and LFPS system show the higher strain and stress generation for y direction.

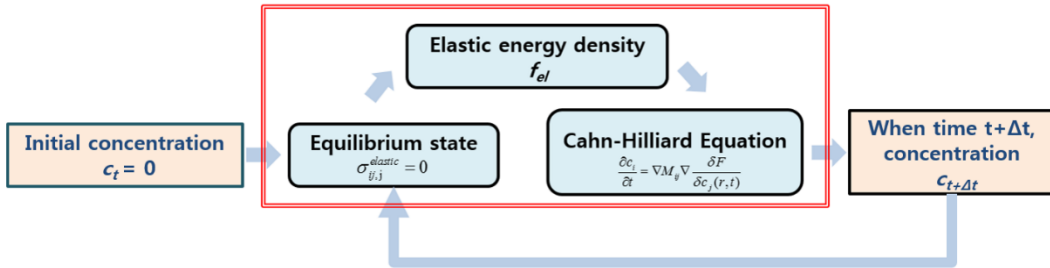


**Fig.5.1. Entire numerical algorithm of multiscale analysis, DFT simulation and PFM method**

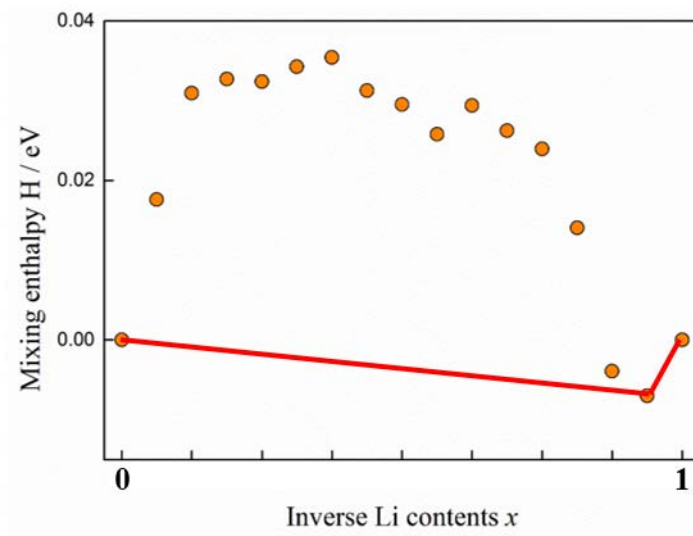


**Fig.5.2. Mixing enthalpy at optimized  $\text{LiFePO}_4$  (LFP) structures as a function of the inverse Li contents  $x$  ( $x = 0 \sim 1$ )**

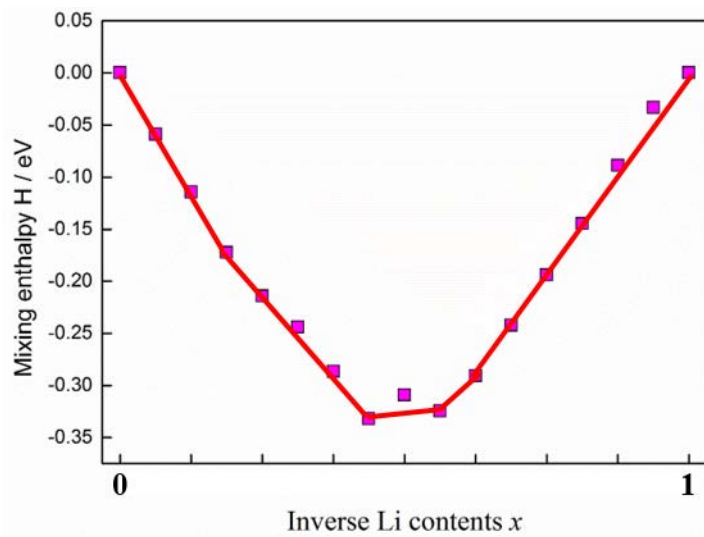


**Fig.5.3. Mixing enthalpy at optimized  $\text{LiFeP}_{0.5}\text{Si}_{0.5}\text{O}_4$  (LFPS) structures as a function of the inverse Li contents  $x$  ( $x = 0 \sim 1$ )**

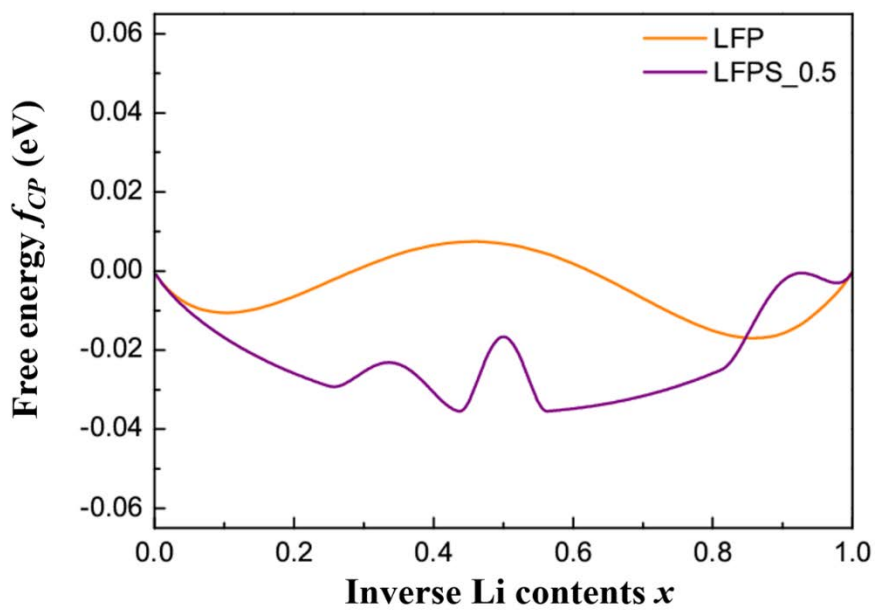


**Fig.5.4. Homogeneous free energies  $f_{CP}$  of LFP and LFPS structures as a function of the inverse Li contents  $x$  ( $x = 0 \sim 1$ )**

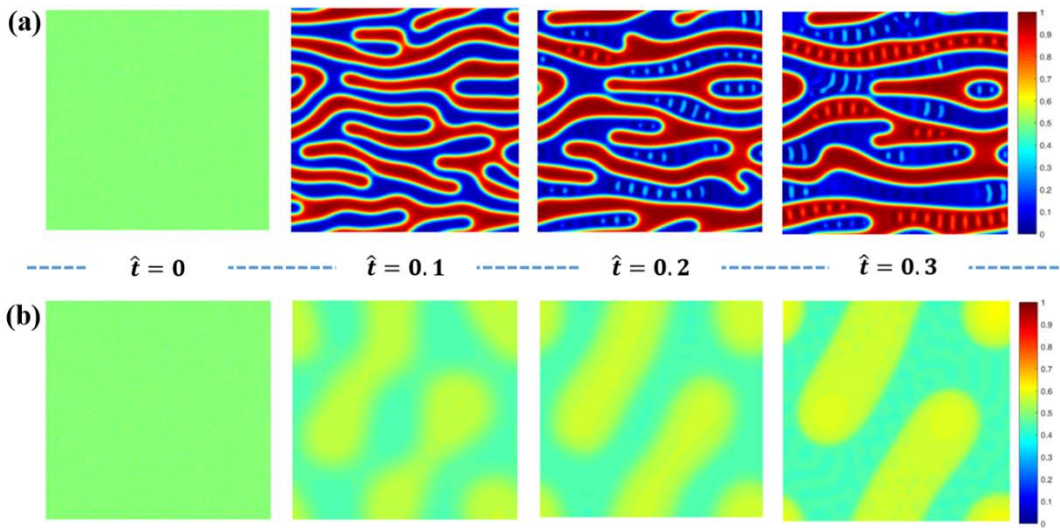


**Fig.5.5.** Entire schematics of phase separation of (a) LFP and (b) LFPS structures at various dimensionless time  $t$

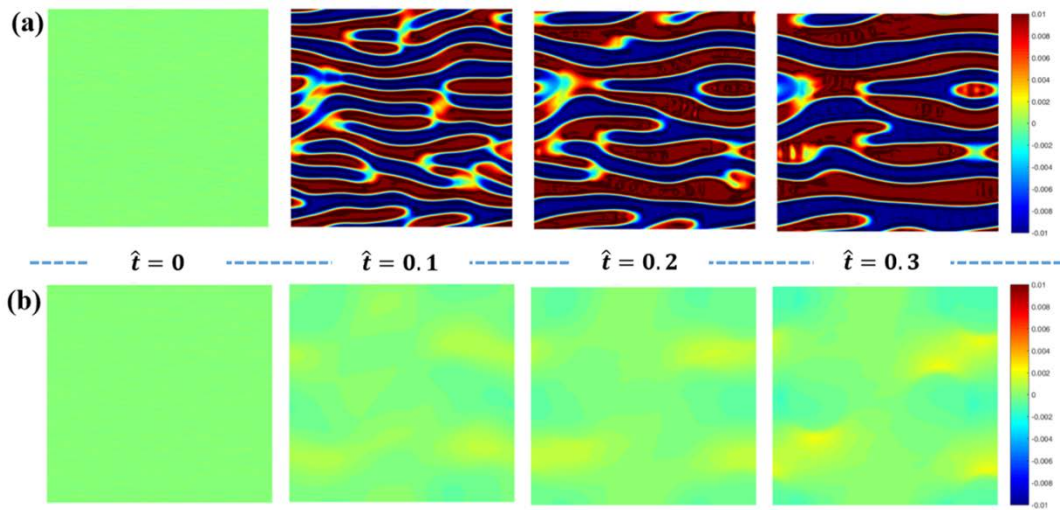


**Fig.5.6.** Entire schematics of strain field  $\epsilon_{xx}$  of (a) LFP and (b) LFPS structures at various dimensionless time  $t$

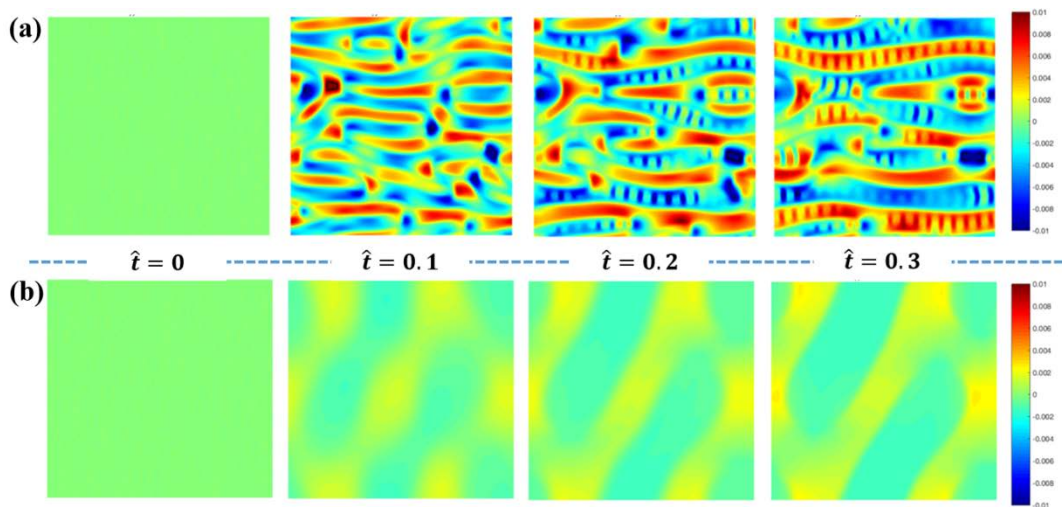


**Fig.5.7.** Entire schematics of strain field  $\varepsilon_{yy}$  of (a) LFP and (b) LFPS structures at various dimensionless time  $t$

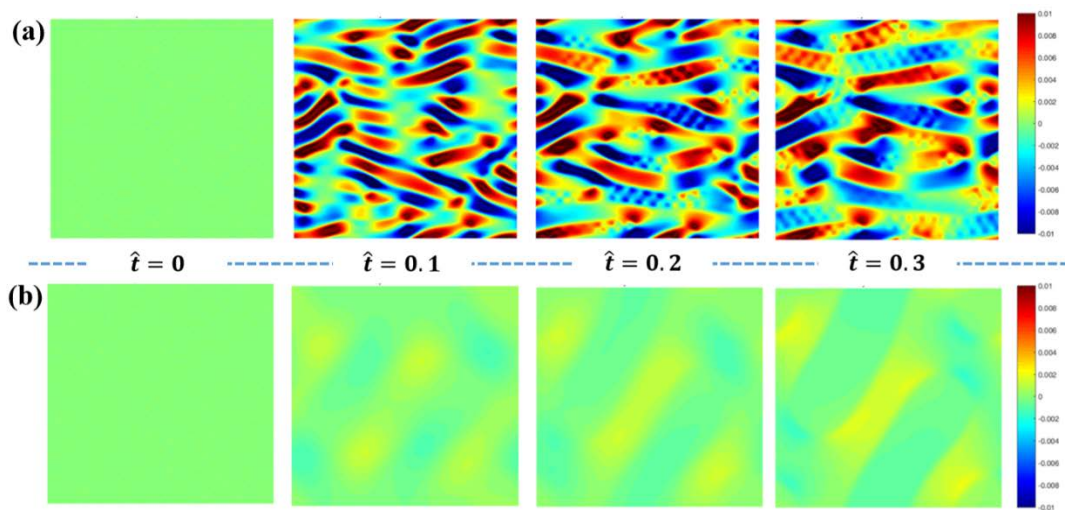


**Fig.5.8.** Entire schematics of strain field  $\varepsilon_{xy}$  of (a) LFP and (b) LFPS structures at various dimensionless time  $t$

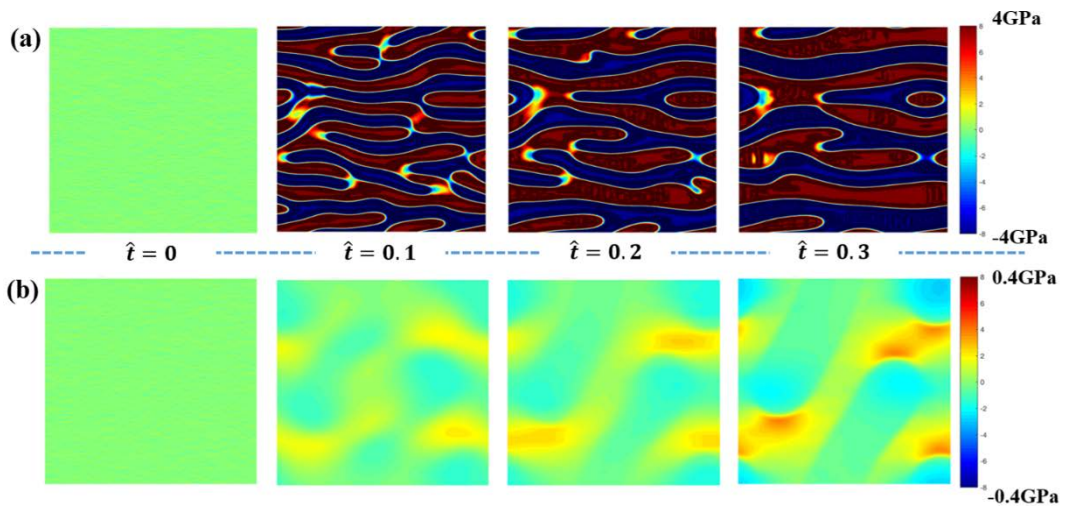


**Fig.5.9.** Entire schematics of stress field  $\sigma_{xx}$  of (a) LFP and (b) LFPS structures at various dimensionless time  $t$

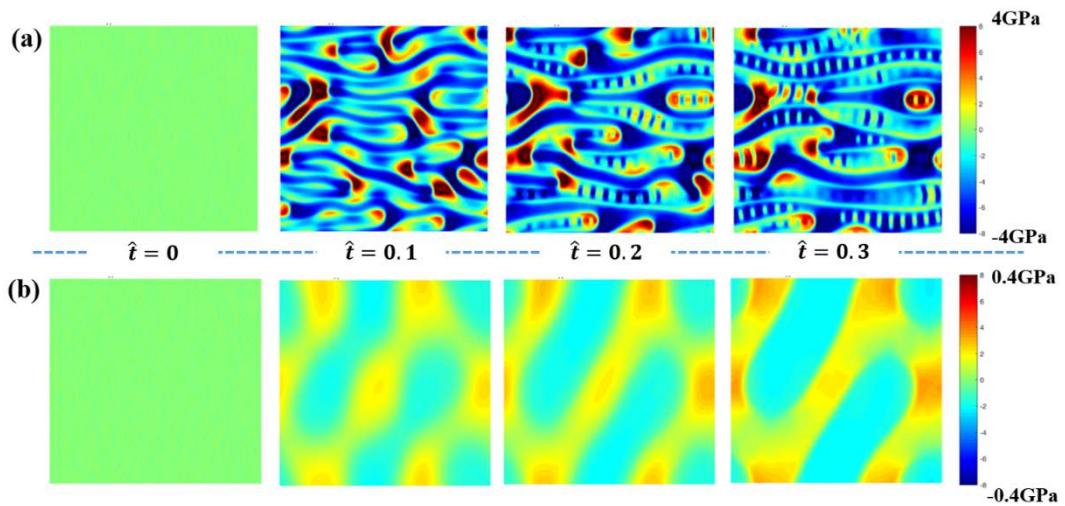


**Fig.5.9.** Entire schematics of stress field  $\sigma_{yy}$  of (a) LFP and (b) LFPS structures at various dimensionless time  $t$

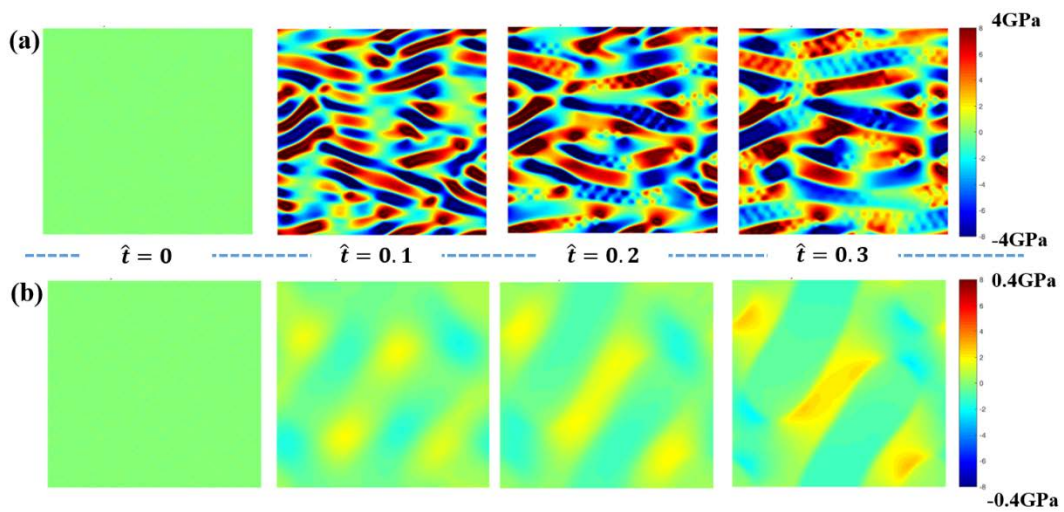


**Fig.5.11. Entire schematics of stress field  $\sigma_{xy}$  of (a) LFP and (b) LFPS structures at various dimensionless time  $t$**

## 6. Conclusion and Recommendations

In the present dissertation, a systematic multiscale analysis based on mechanics is performed from atomic scale using first-principles calculation to macro scale using phase field method at positive electrodes of Li-ion battery. Poly-oxyanion cathode materials received much attention for their higher capacity, higher energy density and better cyclability caused by the stable material structure. The poly-oxyanion materials is composed of lithium, several types of transition metal, oxygen and anions (i.e.  $\text{LiFePO}_4$  and  $\text{Li}_2\text{FeSiO}_4$ ). Lithium orthosilicate  $\text{Li}_2\text{TMSiO}_4$  (TM = Fe, Mn, Ni and Co) are nowadays have attracted considerable attention for their higher theoretical capacity because of two Li ions insertion/extraction and stability for strong Si-O bonding force. However, the orthosilicates suffer from their capacity fading because of phase transformation, worse cyclic performance and low electronic conductivity, so many studies are performed to overcome the disadvantages. However, almost approach is related to electrochemical or electronic point of view not mechanical aspect. Mechanical behaviors of electrode materials is associated with rate capability, and dislocation and cracking micro particle cause of cyclic degradation. To explore the physical mechanism of orthosilicates, mechanical properties are investigated using first-principles study. At first, elastic constants, several moduli and Poisson ratio of pristine orthosilicates are calculated and discuss the values related to elastic softness and rate capability that have different types of transition metal. Furthermore, anisotropic factors which are new measurement are calculated to show

the probability of dislocation and cracking. Also, fundamental understanding is discussed these mechanical values. Mechanical properties of binary multicomponent silicates  $\text{Li}_2\text{Fe}_{0.5}\text{TM}_{0.5}\text{SiO}_4$  (TM = Mn, Ni and Co) are also investigated and compared with pristine silicates, and the multicomponent silicate means that substituted from original transition metals to other transition metals. Hence, manganese silicate has better elastic softness but the material has worse moduli and anisotropic factors, and the results well correspond with experiment results like higher capacity and lower cyclability. Moreover at the multicomponent silicate system, compensate the mechanical properties of original silicate, especially manganese silicate.

Next study is performed the novel design of iron phosphor-silicate  $\text{LiFeP}_{1-x}\text{Si}_x\text{O}_4$  (LFPS,  $x = 0 \sim 1$ ) step by step to overcome the weakness of pristine iron phosphate like low voltage, anti-site defect phenomena, and electronic conductivity, and find the optimized LFPS structure thermodynamically and the LFPS show that prevents the anti-site defect, increases electronic conductivity and voltage, besides the structures are can be control the voltage according to silicon proportion. Furthermore, we design the cathode materials substituted from several anions to phosphorus position at iron phosphate. At first, search for the anion candidates like Ge, As, Se, Sn and Sb including a same or closed group with Si and P, and find the thermodynamically favorable position for optimized structure based on ab-initio study. Finally, optimization structures are calculated the kinetical, electrochemical and electronic properties, and compared with pristine phosphate structure. For this research, Ge substitution structure  $\text{LiFeP}_{1-x}\text{Ge}_x\text{O}_4$  ( $x = 0 \sim 1$ ) most suitable material

for used cathode part of Li-ion batteries than other anion substitution structure materials because the structures have higher and linear voltage value, and a little distortion compared with other structures.

Not only atomic scale but also macro scale analysis of novel designed cathode materials as mentioned before, phase field model is applied for the material's structure  $\text{LiFePO}_4$ ,  $\text{LiFeP}_{1-x}\text{Si}_x\text{O}_4$  ( $x = 0 \sim 1$ ). The mixing enthalpy about lithium ion concentration is calculated using the ab-initio study and is consists of a governing equation connected to physics and chemistry. Through the multiphysics system that used bridging the scale, Phase separation, strain field, and stress field of cathode materials for macro scale. So, phase separation is more decreased at the newly designed  $\text{LiFeP}_{1-x}\text{Si}_x\text{O}_4$  ( $x = 0 \sim 1$ ) than pristine phosphate. And the results mean newly designed poly-oxyanion materials have better rate capability and cyclic performance.

Consequently, for the present multiscale analysis, the electrode mechanism of poly-oxyanion materials is studied for electrochemical and mechanical aspect. Additionally, newly designed the novel poly-oxyanion materials are researched from atomic scale to macro scale, so the materials have improved the performance of poly-oxyanion materials for used cathode materials, and this approach will be the excellent solution for overcoming the cathode materials, furthermore Li ion battery.

## References

1. Tarascon, J.-M.; Armand, M., Issues and challenges facing rechargeable lithium batteries. In *Materials for Sustainable Energy: A Collection of Peer-Reviewed Research and Review Articles from Nature Publishing Group*, World Scientific: 2011; pp 171-179.
2. Suo, L.; Hu, Y.-S.; Li, H.; Armand, M.; Chen, L., A new class of solvent-in-salt electrolyte for high-energy rechargeable metallic lithium batteries. *Nature communications* **2013**, *4*, 1481.
3. Goodenough, J. B.; Kim, Y., Challenges for rechargeable Li batteries. *Chemistry of materials* **2009**, *22* (3), 587-603.
4. Kang, K.; Meng, Y. S.; Bréger, J.; Grey, C. P.; Ceder, G., Electrodes with high power and high capacity for rechargeable lithium batteries. *Science* **2006**, *311* (5763), 977-980.
5. Cubuk, E. D.; Wang, W. L.; Zhao, K.; Vlassak, J. J.; Suo, Z.; Kaxiras, E., Morphological evolution of Si nanowires upon lithiation: A first-principles multiscale model. *Nano Lett.* **2013**, *13* (5), 2011-2015.
6. Tasaki, K., Solvent decompositions and physical properties of decomposition compounds in Li-ion battery electrolytes studied by DFT

calculations and molecular dynamics simulations. *The Journal of Physical Chemistry B* **2005**, *109* (7), 2920–2933.

7. Leung, K.; Budzien, J. L., Ab initio molecular dynamics simulations of the initial stages of solid–electrolyte interphase formation on lithium ion battery graphitic anodes. *PCCP* **2010**, *12* (25), 6583–6586.

8. Xu, B.; Qian, D.; Wang, Z.; Meng, Y. S., Recent progress in cathode materials research for advanced lithium ion batteries. *Materials Science and Engineering: R: Reports* **2012**, *73* (5–6), 51–65.

9. Bai, P.; Bazant, M. Z., Charge transfer kinetics at the solid–solid interface in porous electrodes. *Nature communications* **2014**, *5*, 3585.

10. Dunn, B.; Kamath, H.; Tarascon, J.–M., Electrical energy storage for the grid: a battery of choices. *Science* **2011**, *334* (6058), 928–935.

11. Padhi, A. K.; Nanjundaswamy, K. S.; Goodenough, J. B., Phospho-olivines as positive-electrode materials for rechargeable lithium batteries. *Journal of the electrochemical society* **1997**, *144* (4), 1188–1194.

12. Padhi, A.; Nanjundaswamy, K.; Masquelier, C.; Okada, S.; Goodenough, J., Effect of structure on the Fe<sup>3+</sup>/Fe<sup>2+</sup> redox couple in iron phosphates. *Journal of the Electrochemical Society* **1997**, *144* (5), 1609–1613.

13. Huang, Q.; Li, H.; Grätzel, M.; Wang, Q., Reversible chemical delithiation/lithiation of LiFePO<sub>4</sub>: towards a redox flow lithium–ion battery.

*PCCP* **2013**, *15* (6), 1793–1797.

14. Li, G.; Azuma, H.; Tohda, M., LiMnPO<sub>4</sub> as the cathode for lithium batteries. *Electrochem. Solid-State Lett.* **2002**, *5* (6), A135–A137.

15. Kornev, I.; Bichurin, M.; Rivera, J.-P.; Gentil, S.; Schmid, H.; Jansen, A.; Wyder, P., Magnetolectric properties of LiCoPO<sub>4</sub> and LiNiPO<sub>4</sub>. *Physical Review B* **2000**, *62* (18), 12247.

16. Wolfenstine, J.; Allen, J., LiNiPO<sub>4</sub>–LiCoPO<sub>4</sub> solid solutions as cathodes. *Journal of Power Sources* **2004**, *136* (1), 150–153.

17. Nyten, A.; Abouimrane, A.; Armand, M.; Gustafsson, T.; Thomas, J. O., Electrochemical performance of Li<sub>2</sub>FeSiO<sub>4</sub> as a new Li–battery cathode material. *Electrochemistry communications* **2005**, *7* (2), 156–160.

18. Larsson, P.; Ahuja, R.; Nyten, A.; Thomas, J. O., An ab initio study of the Li–ion battery cathode material Li<sub>2</sub>FeSiO<sub>4</sub>. *Electrochemistry Communications* **2006**, *8* (5), 797–800.

19. Dominko, R.; Conte, D.; Hanzel, D.; Gaberscek, M.; Jamnik, J., Impact of synthesis conditions on the structure and performance of Li<sub>2</sub>FeSiO<sub>4</sub>. *Journal of Power Sources* **2008**, *178* (2), 842–847.

20. Yi, L.; Wang, X.; Wang, G.; Bai, Y.; Liu, M.; Wang, X.; Yu, R., Improved electrochemical performance of spherical Li<sub>2</sub>FeSiO<sub>4</sub>/C cathode materials via Mn doping for lithium–ion batteries. *Electrochimica Acta* **2016**, *222*, 1354–1364.

21. Islam, M. S.; Dominko, R.; Masquelier, C.; Sirisopanaporn, C.; Armstrong, A. R.; Bruce, P. G., Silicate cathodes for lithium batteries: alternatives to phosphates? *Journal of Materials Chemistry* **2011**, *21* (27), 9811–9818.
22. Vajeeston, P.; Bianchini, F.; Fjellvåg, H., First-Principles Study of the Structural Stability and Dynamic Properties of Li<sub>2</sub>MSiO<sub>4</sub> (M= Mn, Co, Ni) Polymorphs. *Energies* **2019**, *12* (2), 224.
23. Zhang, P.; Hu, C.; Wu, S.; Zhu, Z.; Yang, Y., Structural properties and energetics of Li<sub>2</sub>FeSiO<sub>4</sub> polymorphs and their delithiated products from first-principles. *PCCP* **2012**, *14* (20), 7346–7351.
24. Sirisopanaporn, C.; Masquelier, C.; Bruce, P. G.; Armstrong, A. R.; Dominko, R., Dependence of Li<sub>2</sub>FeSiO<sub>4</sub> electrochemistry on structure. *J. Am. Chem. Soc.* **2010**, *133* (5), 1263–1265.
25. Wu, S.; Zhu, Z.; Yang, Y.; Hou, Z., Structural stabilities, electronic structures and lithium deintercalation in Li<sub>x</sub>MSiO<sub>4</sub> (M= Mn, Fe, Co, Ni): A GGA and GGA+ U study. *Computational materials science* **2009**, *44* (4), 1243–1251.
26. Dominko, R.; Bele, M.; Kokalj, A.; Gaberscek, M.; Jamnik, J., Li<sub>2</sub>MnSiO<sub>4</sub> as a potential Li-battery cathode material. *Journal of Power Sources* **2007**, *174* (2), 457–461.
27. Arroyo-de Dompablo, M.; Armand, M.; Tarascon, J.; Amador, U.,

On-demand design of polyoxianionic cathode materials based on electronegativity correlations: An exploration of the  $\text{Li}_2\text{MSiO}_4$  system (M= Fe, Mn, Co, Ni). *Electrochemistry Communications* **2006**, *8* (8), 1292–1298.

28. Lu, X.; Chiu, H.-C.; Bevan, K. H.; Jiang, D.-T.; Zaghbi, K.; Demopoulos, G. P., Density functional theory insights into the structural stability and Li diffusion properties of monoclinic and orthorhombic  $\text{Li}_2\text{FeSiO}_4$  cathodes. *Journal of Power Sources* **2016**, *318*, 136–145.

29. Kashkooli, A. G.; Farhad, S.; Lee, D. U.; Feng, K.; Litster, S.; Babu, S. K.; Zhu, L.; Chen, Z., Multiscale modeling of lithium-ion battery electrodes based on nano-scale X-ray computed tomography. *Journal of Power Sources* **2016**, *307*, 496–509.

30. Shin, H.; Baek, K.; Han, J.-G.; Cho, M., Homogenization analysis of polymeric nanocomposites containing nanoparticulate clusters. *Compos. Sci. Technol.* **2017**, *138*, 217–224.

31. Ngandjong, A. C.; Rucci, A.; Maiza, M.; Shukla, G.; Vazquez-Arenas, J.; Franco, A. A., Multiscale Simulation Platform Linking Lithium Ion Battery Electrode Fabrication Process with Performance at the Cell Level. *The journal of physical chemistry letters* **2017**, *8* (23), 5966–5972.

32. Pharr, M.; Suo, Z.; Vlassak, J. J., Measurements of the fracture energy of lithiated silicon electrodes of Li-ion batteries. *Nano Lett.* **2013**, *13* (11), 5570–5577.

33. Mori, T.; Tanaka, K., Average stress in matrix and average elastic energy of materials with misfitting inclusions. *Acta Metall.* **1973**, *21* (5), 571-574.
34. Li, L.; Han, E.; Dou, L.; Zhu, L.; Mi, C.; Li, M.; Niu, J., Enhanced Electrochemical performance of Li<sub>2</sub>FeSiO<sub>4</sub>/C as cathode for lithium-ion batteries via metal doping at Fe-site. *Solid State Ionics* **2018**, *325*, 30-42.
35. Longo, R.; Xiong, K.; Wang, W.; Cho, K., Influence of the exchange-correlation potential on the electrochemical properties of multicomponent silicate cathode materials. *Electrochimica Acta* **2012**, *80*, 84-89.
36. Longo, R.; Xiong, K.; Santosh, K.; Cho, K., Crystal structure and multicomponent effects in Tetrahedral Silicate Cathode Materials for Rechargeable Li-ion Batteries. *Electrochimica Acta* **2014**, *121*, 434-442.
37. Hao, H.; Wang, J.; Liu, J.; Huang, T.; Yu, A., Synthesis, characterization and electrochemical performance of Li<sub>2</sub>FeSiO<sub>4</sub>/C cathode materials doped by vanadium at Fe/Si sites for lithium ion batteries. *Journal of Power Sources* **2012**, *210*, 397-401.
38. Zhang, L.-L.; Duan, S.; Yang, X.-L.; Liang, G.; Huang, Y.-H.; Cao, X.-Z.; Yang, J.; Li, M.; Croft, M. C.; Lewis, C., Insight into cobalt-doping in Li<sub>2</sub>FeSiO<sub>4</sub> cathode material for lithium-ion battery. *Journal of Power Sources* **2015**, *274*, 194-202.
39. Li, L.; Han, E.; Qiao, S.; Liu, H.; Shi, Y.; Yuan, W., Synthesis

characterization and improved electrochemical performance of  $\text{Li}_2\text{FeSiO}_4/\text{C}$  as cathode for lithium-ion battery by metal doping. *Progress in Natural Science: Materials International* **2019**.

40. Wang, Y. X.; Geng, H. Y.; Wu, Q.; Chen, X. R.; Sun, Y., First-principles investigation of elastic anomalies in niobium at high pressure and temperature. *Journal of Applied Physics* **2017**, *122* (23), 235903.

41. Eames, C.; Armstrong, A.; Bruce, P.; Islam, M., Insights into changes in voltage and structure of  $\text{Li}_2\text{FeSiO}_4$  polymorphs for lithium-ion batteries. *Chemistry of Materials* **2012**, *24* (11), 2155–2161.

42. Chang, S.; Moon, J.; Cho, M., Stress-diffusion coupled multiscale analysis of Si anode for Li-ion battery. *Journal of Mechanical Science and Technology* **2015**, *29* (11), 4807–4816.

43. Maxisch, T.; Ceder, G., Elastic properties of olivine  $\text{Li}_x\text{FePO}_4$  from first principles. *Physical Review B* **2006**, *73* (17), 174112.

44. Söderlind, P.; Klepeis, J. E., First-principles elastic properties of  $\alpha\text{-Pu}$ . *Physical Review B* **2009**, *79* (10), 104110.

45. Wang, D.; Wu, X.; Wang, Z.; Chen, L., Cracking causing cyclic instability of  $\text{LiFePO}_4$  cathode material. *Journal of Power Sources* **2005**, *140* (1), 125–128.

46. Singh, G.; Bazant, M.; Ceder, G., Anisotropic surface reaction limited phase transformation dynamics in  $\text{LiFePO}_4$ . *arXiv preprint arXiv:0707.1858*

2007.

47. Wolverton, C.; Zunger, A., First-principles prediction of vacancy order-disorder and intercalation battery voltages in  $\text{Li}_x\text{CoO}_2$ . *Phys. Rev. Lett.* **1998**, *81* (3), 606.

48. Kresse, G.; Furthmüller, J., Efficient iterative schemes for ab initio total-energy calculations using a plane-wave basis set. *Physical review B* **1996**, *54* (16), 11169.

49. Tani, J.-i.; Takahashi, M.; Kido, H., First-principles calculations of the structural and elastic properties of  $\beta\text{-FeSi}_2$  at high-pressure. *Intermetallics* **2010**, *18* (6), 1222-1227.

50. Ravindran, P.; Fast, L.; Korzhavyi, P. A.; Johansson, B.; Wills, J.; Eriksson, O., Density functional theory for calculation of elastic properties of orthorhombic crystals: Application to  $\text{TiSi}_2$ . *Journal of Applied Physics* **1998**, *84* (9), 4891-4904.

51. Voigt, W., Lehrbuch der Kristallphysik (Teubner, Leipzig, 1928).  
*There is no corresponding record for this reference* **1908**.

52. Reuss, A., Calculation of the flow limits of mixed crystals on the basis of the plasticity of monocrystals. *Z. Angew. Math. Mech* **1929**, *9*, 49-58.

53. Hill, R., The elastic behaviour of a crystalline aggregate. *Proceedings of the Physical Society. Section A* **1952**, *65* (5), 349.

54. Hill, R., Elastic properties of reinforced solids: some theoretical principles. *J. Mech. Phys. Solids* **1963**, *11* (5), 357–372.
55. Zeng, Y.; Chiu, H.-C.; Rasool, M.; Brodusch, N.; Gauvin, R.; Jiang, D.-T.; Ryan, D. H.; Zaghbi, K.; Demopoulos, G. P., Hydrothermal crystallization of Pmn21 Li<sub>2</sub>FeSiO<sub>4</sub> hollow mesocrystals for Li-ion cathode application. *Chem. Eng. J.* **2019**, *359*, 1592–1602.
56. Saracibar, A.; Van der Ven, A.; Arroyo-de Dompablo, M., Crystal structure, energetics, and electrochemistry of Li<sub>2</sub>FeSiO<sub>4</sub> polymorphs from first principles calculations. *Chemistry of Materials* **2012**, *24* (3), 495–503.
57. Girish, H.-N.; Shao, G.-Q., Advances in high-capacity Li<sub>2</sub>MSiO<sub>4</sub> (M= Mn, Fe, Co, Ni,…) cathode materials for lithium-ion batteries. *RSC Advances* **2015**, *5* (119), 98666–98686.
58. Aghabozorg, H.; Palenik, G. J.; Stouffer, R. C.; Summers, J., Dynamic Jahn-Teller effect in a manganese (III) complex. Synthesis and structure of hexakis (urea) manganese (III) perchlorate. *Inorg. Chem.* **1982**, *21* (11), 3903–3907.
59. Huang, H.; Yin, S.-C.; Nazar, L. s., Approaching theoretical capacity of LiFePO<sub>4</sub> at room temperature at high rates. *Electrochem. Solid-State Lett.* **2001**, *4* (10), A170–A172.
60. Nishijima, M.; Ootani, T.; Kamimura, Y.; Sueki, T.; Esaki, S.; Murai, S.; Fujita, K.; Tanaka, K.; Ohira, K.; Koyama, Y., Accelerated discovery of

cathode materials with prolonged cycle life for lithium-ion battery. *Nature communications* **2014**, *5*, 4553.

61. Islam, M. S.; Driscoll, D. J.; Fisher, C. A.; Slater, P. R., Atomic-scale investigation of defects, dopants, and lithium transport in the LiFePO<sub>4</sub> olivine-type battery material. *Chemistry of Materials* **2005**, *17* (20), 5085–5092.

62. Nishimura, S.-i.; Kobayashi, G.; Ohoyama, K.; Kanno, R.; Yashima, M.; Yamada, A., Experimental visualization of lithium diffusion in Li<sub>x</sub>FePO<sub>4</sub>. *Nature materials* **2008**, *7* (9), 707.

63. Recham, N.; Casas-Cabanas, M.; Cabana, J.; Grey, C.; Jumas, J.-C.; Dupont, L.; Armand, M.; Tarascon, J.-M., Formation of a complete solid solution between the triphylite and fayalite olivine structures. *Chemistry of Materials* **2008**, *20* (21), 6798–6809.

64. Zhai, P.-Y.; Zhao, S.-X.; Cheng, H.-M.; Zhao, J.-W.; Nan, C.-W., Synthesis and structural stability of Li<sub>2</sub>.<sub>1</sub>Mn<sub>0.9</sub> [PO<sub>4</sub>]<sub>0.1</sub> [SiO<sub>4</sub>]<sub>0.9</sub>/C mixed polyanion cathode material for Li-ion battery. *Electrochimica Acta* **2015**, *153*, 217–224.

65. Henkelman, G.; Jónsson, H., Improved tangent estimate in the nudged elastic band method for finding minimum energy paths and saddle points. *The Journal of chemical physics* **2000**, *113* (22), 9978–9985.

66. Aydinol, M.; Kohan, A.; Ceder, G.; Cho, K.; Joannopoulos, J., Ab initio

study of lithium intercalation in metal oxides and metal dichalcogenides.

*Physical Review B* **1997**, *56* (3), 1354.

67. Hu, S.; Li, Y.; Rosso, K. M.; Sushko, M. L., Mesoscale phase-field modeling of charge transport in nanocomposite electrodes for lithium-ion batteries. *The Journal of Physical Chemistry C* **2012**, *117* (1), 28–40.

68. Moon, J.; Lee, B.; Cho, M.; Cho, K., Ab initio and kinetic Monte Carlo study of lithium diffusion in LiSi, Li<sub>12</sub>Si<sub>7</sub>, Li<sub>13</sub>Si<sub>5</sub> and Li<sub>15</sub>Si<sub>4</sub>. *Journal of Power Sources* **2016**, *328*, 558–566.

69. Henkelman, G.; Uberuaga, B. P.; Jónsson, H., A climbing image nudged elastic band method for finding saddle points and minimum energy paths. *The Journal of chemical physics* **2000**, *113* (22), 9901–9904.

70. Maxisch, T.; Zhou, F.; Ceder, G., Ab initio study of the migration of small polarons in olivine Li<sub>x</sub>FePO<sub>4</sub> and their association with lithium ions and vacancies. *Physical review B* **2006**, *73* (10), 104301.

71. Shi, J.; Wang, Z.; Fu, Y. Q., Density functional theory study of lithium diffusion at the interface between olivine-type LiFePO<sub>4</sub> and LiMnPO<sub>4</sub>. *Journal of Physics D: Applied Physics* **2016**, *49* (50), 505601.

72. Johannes, M.; Hoang, K.; Allen, J.; Gaskell, K., Hole polaron formation and migration in olivine phosphate materials. *Physical Review B* **2012**, *85* (11), 115106.

73. Laffont, L.; Delacourt, C.; Gibot, P.; Wu, M. Y.; Kooyman, P.;

Masquelier, C.; Tarascon, J. M., Study of the LiFePO<sub>4</sub>/FePO<sub>4</sub> two-phase system by high-resolution electron energy loss spectroscopy. *Chemistry of Materials* **2006**, *18* (23), 5520–5529.

74. Yang, J.; Zheng, J.; Kang, X.; Teng, G.; Hu, L.; Tan, R.; Wang, K.; Song, X.; Xu, M.; Mu, S., Tuning structural stability and lithium-storage properties by d-orbital hybridization substitution in full tetrahedron Li<sub>2</sub>FeSiO<sub>4</sub> nanocrystal. *Nano Energy* **2016**, *20*, 117–125.

75. Latz, A.; Zausch, J., Thermodynamic derivation of a Butler–Volmer model for intercalation in Li-ion batteries. *Electrochimica Acta* **2013**, *110*, 358–362.

76. Cahn, J. W.; Hilliard, J. E., Free energy of a nonuniform system. I. Interfacial free energy. *The Journal of chemical physics* **1958**, *28* (2), 258–267.

77. Chung, K. Y.; Yoon, W.-S.; Kim, K.-B.; Yang, X.-Q.; Oh, S. M., Suppression of structural fatigue by doping in spinel electrode probed by in situ bending beam method. *Journal of The Electrochemical Society* **2004**, *151* (3), A484–A492.

78. Birch, F., Finite elastic strain of cubic crystals. *Phys. Rev.* **1947**, *71* (11), 809.

79. Meethong, N.; Huang, H. Y.; Speakman, S. A.; Carter, W. C.; Chiang, Y. M., Strain accommodation during phase transformations in olivine-based

cathodes as a materials selection criterion for high-power rechargeable batteries. *Advanced Functional Materials* **2007**, *17*(7), 1115–1123.

80. Lim, J.-M.; Cho, K.; Cho, M., Phase transformations with stress generations in electrochemical reactions of electrodes: Mechanics-based multiscale model for combined-phase reactions. *Extreme Mechanics Letters* **2017**, *11*, 89–95.

81. Bai, P.; Cogswell, D. A.; Bazant, M. Z., Suppression of phase separation in LiFePO<sub>4</sub> nanoparticles during battery discharge. *Nano Lett.* **2011**, *11*(11), 4890–4896.

82. Li, Y.; El Gabaly, F.; Ferguson, T. R.; Smith, R. B.; Bartelt, N. C.; Sugar, J. D.; Fenton, K. R.; Cogswell, D. A.; Kilcoyne, A. D.; Tyliszczak, T., Current-induced transition from particle-by-particle to concurrent intercalation in phase-separating battery electrodes. *Nature materials* **2014**, *13*(12), 1149.

83. Heo, T. W.; Tang, M.; Chen, L. Q.; Wood, B. C., Defects, entropy, and the stabilization of alternative phase boundary orientations in battery electrode particles. *Advanced Energy Materials* **2016**, *6*(6), 1501759.

## 국문 요약

리튬 이온 전지는 이차 전지 중 하나로 기존 전지와는 다르게 반복해서 사용할 수 있는 전지 중 하나로써, 크게 양극, 음극 그리고 전해질로 구분할 수 있다. 양극 재료는 방전 시 리튬을 저장하고, 충전 시 리튬을 다시 음극에 보내주는 역할을 하는데 이 때, 다양한 단위에서 복잡한 반응들이 발생한다. 본 논문에서는 양극 재료 중 하나인 다중 산소 음이온 포함 물질에 대해 원자 단위부터 마크로 단위까지 이르는 멀티스케일 해석을 수행하였다. 우선 원자 단위에서 대부분의 양극 연구는 전기화학적 및 전기적 성능의 해석 및 발전에 치중하여 연구가 진행되어왔다. 그러나 구조의 어긋남 및 전극의 균열에 의한 재현성의 저하나, 용량의 감소 등 역시 리튬 이온 전지의 성능을 위한 중요한 요소이며 이에 대한 해석을 위해 기계적인 물성 해석은 필수적이다. 따라서 다양한 전이 금속이나 두 개 이상의 전이금속을 가진 규산염에 대해 탄성 상수, 여러 탄성률 및 포아송 비를 계산하여 기계적인 측면에 대해 해석을 수행하였다. 나아가 이러한 규산염들에 대해 비등방성 해석을 수행하여 기계적인 물성 해석을 통해 양극 재료의 새로운 설계 방향을 제시하였다.

뿐만 아니라 기존의 철 인산염의 한계를 극복하기 위해, 새로운 다중 산소 음이온 포함 양극 물질의 설계를 수행하였다. 음이온의 치환을 통해 새로운 철 규산-인산염을 설계하고 실리콘의 비율에 따라 물성이 어떻게 변하는지 확인하였다. 본 소제는 기존 철 인산염의 낮은 전압을 극복하고, 실리콘의 비율

에 따라 전압을 조절할 수 있음을 확인하였다. 뿐만 아니라 인산염의 단점 중 하나인 안티 사이트 결합 현상을 억제하고 기존의 전자 전도성보다 높은 전자 전도성을 가질 수 있음을 확인하였다. 이는 그 전 연구에서 낮은 전자 전도성을 극복하기 위한 탄소 코팅과 조합되어 더욱 높은 전자 전도성을 가지는 양극 물질을 설계할 수 있음을 의미한다.

뿐만 아니라 기존의 인산염에서 As, Sb, Ge, Sn 그리고 Se와 같은 다양한 음이온 치환을 통해 새로운 양극 물질을 설계하여 그 성능 해석을 수행하였다. 그 결과 음이온과 산소 결합에서 전자 분포 해석을 수행하여 같은 족에 있는 경우 비슷한 전압을 가짐을 확인하였다. 뿐만 아니라 Ge의 치환을 통해 보다 안정적인 구조를 가지면서 전압을 상승시키고, Ge의 비율에 따라 전압을 조절할 수 있는 새로운 다중 산소 음이온 포함 양극 물질을 설계하였다.

뿐만 아니라 기존의 철 인산염 및 새롭게 설계된 다중 산소 음이온 물질 철 규산-인산염에서의 멀티스케일 해석을 동시에 수행 및 비교하여, 메조 스케일에서 상 분리를 확인하여 충/방전 과정 시 새롭게 설계된 철 규산-인산염에서 보다 안정적인 상을 가짐을 확인하였다. 나아가 변형 및 피로 멀티스케일 해석을 수행하여 철 규산-인산염에서 보다 안정적인 구조를 유지할 수 있고, 따라서 충/방전 시 더 좋은 재현성 및 성능 유지가 가능함을 확인하였다.

본 연구는 역학적 멀티스케일 해석을 통해 기존 다중 산소 음이온 양극 물질의 새로운 물성 해석을 수행하고, 보다 높은 성능을 가지면서 기존의 단점을 극복한 새로운 양극 물질 설계를 제안하였다. 나아가 기존의 한계를 극

복하는 새로운 양극 물질로 인해 보다 개선된 리튬 이온 전지의 설계 및 나아갈 방향성을 제시할 수 있을 것으로 기대된다.

**주요어:** 리튬 이온 전지, 다중 산소 음이온 포함 양극 물질, 밀도 이론 함수, 제일 원리 계산, 상장 역학 모델, 멀티스케일 해석

**학번:** 2012-22562